

**Protein Detection using Semiconducting Single-Walled Carbon Nanotube-Based Field-
Effect Transistors**

by

Wenting Shao

B.S. in Chemistry, Nanjing University, 2014

Submitted to the Graduate Faculty of the
Dietrich School of Arts and Sciences in partial fulfillment
of the requirements for the degree of
Doctor of Philosophy

University of Pittsburgh

2021

UNIVERSITY OF PITTSBURGH

DIETRICH SCHOOL OF ARTS AND SCIENCES

This dissertation was presented

by

Wenting Shao

It was defended on

April 6, 2021

and approved by

Dr. Haitao Liu, Professor, Department of Chemistry

Dr. Stephen G. Weber, Professor, Department of Chemistry

Dr. Michael R. Shurin, Professor, Department of Pathology

Thesis Advisor/Dissertation Director: Dr. Alexander Star, Professor, Department of Chemistry

Copyright © by Wenting Shao

2021

Protein Detection using Semiconducting Single-Walled Carbon Nanotube-Based Field-Effect Transistors

Wenting Shao, PhD

University of Pittsburgh, 2021

Proteins are large biomolecules that play many critical roles in living organisms, and some proteins, the presence or level of which can be directly correlated with disease status, are extremely important for disease diagnosis and monitoring. Therefore, recent years have seen a rapid expansion of the field of disease relevant protein detection as it is key to the development of rapid diagnostics tools and healthcare monitoring devices. Common techniques for protein detection include immunoassays, mass spectrometry, and biosensors. Immunoassay-based techniques have shown advantages such as low cost and easy mass-production but suffer from low sensitivity. Mass spectrometry, although having high speed and sensitivity, necessitates large and expensive instruments therefore is not easily accessible. Biosensors have attracted much attention in the field of protein detection owing to the high sensitivity, rapid responsiveness, versatility, and miniaturability biosensors provide. In particular, field-effect transistor (FET)-based biosensing devices have demonstrated great potential for the application of point-of-care diagnostics as they offer an excellent platform for rapid, label-free and real-time detection of proteins.

Carbon nanotubes are an ideal sensing material for electrochemical biosensors, with their nanoscale dimensions enabling the sensitive probing of biomolecular interactions. Recently, high-purity semiconducting (sc-) single-walled carbon nanotubes (SWCNTs) have emerged as a promising material for high-performance biosensing devices. At the same time, the successful

functionalization of sc-SWCNTs with the specific biorecognition element, together with a complete characterization of the sc-SWCNT FET device are crucial for achieving high specificity toward the target analyte.

In this dissertation, high-purity semiconducting SWCNTs, with different chemical functionalization, have been utilized to develop FET-based biosensors for protein detection. Sc-SWCNTs were first decorated with gold nanoparticles and employed in investigating the Ca^{2+} -induced conformational change of calmodulin – a vital process in calcium signal transduction in the human body. The sc-SWCNT FET devices were then incorporated in a three-step strategy to develop a sensing platform for the detection of β 2-transferrin in body fluids as a potential diagnostic tool for cerebrospinal fluid leak. Finally, sc-SWCNT-based FET biosensors were functionalized with severe acute respiratory syndrome coronavirus 2 (SARS-CoV-2) antibodies to detect SARS-CoV-2 antigens in nasopharyngeal swab samples.

Table of Contents

Preface.....	xii
1.0 Introduction.....	1
1.1 Protein Detection	1
1.1.1 Significance	1
1.1.2 Common Methods for Protein Detection	3
1.1.3 Challenges	6
1.2 Single-Walled Carbon Nanotubes and their Applications in Protein Detection	7
1.2.1 Sorting of Single-Walled Carbon Nanotubes	8
1.2.2 Functionalization of Single-Walled Carbon Nanotubes	10
1.2.3 Characterization Methods of Single-Walled Carbon Nanotubes	13
1.2.4 Single-Walled Carbon Nanotube-Based Field-Effect Transistors for Protein Detection.....	16
2.0 Probing Ca²⁺-Induced Conformational Change of Calmodulin with Gold Nanoparticle-Decorated Single-Walled Carbon Nanotube-Based Field-Effect Transistors	19
2.1 Chapter Preface	19
2.2 Introduction	19
2.3 Experimental Section	22
2.4 Results and Discussion	26
2.5 Conclusions	39
2.6 Acknowledgement.....	40

3.0 Cerebrospinal Fluid Leak Detection with a Carbon Nanotube-Based Field-Effect	
Transistor Biosensing Platform	41
3.1 Chapter Preface	41
3.2 Introduction	41
3.3 Experimental Section	44
3.4 Results and Discussion	50
3.5 Conclusions	58
3.6 Acknowledgement.....	59
4.0 Rapid Detection of SARS-CoV-2 Antigens using High-Purity Semiconducting	
Single-Walled Carbon Nanotube-Based Field-Effect Transistors.....	60
4.1 Chapter Preface	60
4.2 Introduction	60
4.3 Experimental Section	63
4.4 Results and Discussion	66
4.5 Conclusions	73
4.6 Acknowledgement.....	74
5.0 Future Outlook.....	75
Appendix A Chapter 2 Supporting Information	76
Appendix B Chapter 3 Supporting Information.....	85
Appendix C Chapter 4 Supporting Information	94
Appendix D List of Publications during PhD Study.....	101
Bibliography	102

List of Tables

Appendix Table A-1 Comparison of various methods for Ca²⁺ detection	84
Appendix Table B-1 Transferrin concentration of positive and negative sample after 2 steps of separation determined from the standard curve.	85
Appendix Table B-2 Relative response of each body fluid sample tested with sc-SWCNT FET devices using Tf-ab-SWCNT and Au electrode approach.	93
Appendix Table C-1 Number of devices (n) tested for each clinical sample.	99

List of Figures

Figure 1-1 Schematic illustration of the three main types of ELISA.....	4
Figure 1-2 Schematic diagram of the three fundamental components of a biosensor.	6
Figure 1-3 Classification of SWCNTs by chiral indices.....	8
Figure 1-4 Noncovalent and covalent functionalization of SWCNTs.	12
Figure 1-5 Common techniques for characterization of SWCNTs.....	15
Figure 1-6 Illustration of a SWCNT-based FET device and FET transfer characteristics.	17
Figure 2-1 Binding of CaM on Au-sc-SWCNT and Au-un-SWCNT FET devices.....	27
Figure 2-2 UV-vis-NIR absorption spectroscopy of un-SWCNT and sc-SWCNT during functionalization.....	30
Figure 2-3 Raman spectroscopy of un-SWCNT and sc-SWCNT during functionalization.	31
Figure 2-4 Fluorescence images of EGFP-CaM functionalized Au-SWCNT FET device. ..	33
Figure 2-5 Ca²⁺ sensing with CaM-un-SWCNT and sc-SWCNT FET devices.....	36
Figure 3-1 The 3-step strategy for detection of β2-Tf.....	51
Figure 3-2 Detection of transferrin using bare SWCNT FET devices.....	53
Figure 3-3 Detection of recombinant transferrin using sc-SWCNT FET devices.	54
Figure 3-4 β2-Tf detection in CSF (blue) and serum (grey) using Tf-ab-SWCNT FET devices and Au electrode approach. Results are mean \pm SEM.....	57
Figure 4-1 Detection of SARS-CoV-2 Ag using SWCNT-based FET biosensors.	63
Figure 4-2 Characterizations of SARS-CoV-2 antibody-functionalized SWCNT FET devices.	68
Figure 4-3 Detection of recombinant SARS-CoV-2 antigen proteins.	70

Figure 4-4 Clinical sample tests with a SAb and NAb functionalized FET devices.	73
Appendix Figure A-1 SEM characterization of Au-un-SWCNTs and Au-sc-SWCNTs.	76
Appendix Figure A-2 AFM characterization of Au-unSWCNTs before and after CaM binding.	77
Appendix Figure A-3 Raman spectroscopy characterization of un-SWCNTs and sc-SWCNTs in the RBM region.	78
Appendix Figure A-4 Circular Dichroism solution spectra of calcium-free CaM (apo-CaM) and calcium-bound CaM with different concentrations of CaCl₂.	79
Appendix Figure A-5 Expression of EGFP-CaM in HEK293T cells.	80
Appendix Figure A-6 Device reproducibility of un-SWCNT and sc-SWCNT FET devices.	80
Appendix Figure A-7 Control experiments with un-SWCNT and sc-SWCNT FET devices.	81
Appendix Figure A-8 Comparison of source-drain current (I_d) and gate leakage current (I_g) for sc-SWCNT and un-SWCNT FET devices.	82
Appendix Figure A-9 Comparison of on/ff ratio of un-SWCNT and sc-SWCNT FET devices.	82
Appendix Figure A-10 Comparison of calibration sensitivity of un-SWCNT and sc-SWCNT FET devices.	83
Appendix Figure B-1 Transferrin ELISA standard curve.	85
Appendix Figure B-2 Characterizations of high-purity semiconducting single-walled carbon nanotubes.	86
Appendix Figure B-3 Nonspecific binding of Alexa Fluor 647 conjugated transferrin on bare sc-SWCNTs.	87

Appendix Figure B-4 Fluorescence characterization of Tf-ab functionalized sc-SWCNT FET device.....	88
Appendix Figure B-5 RBM region of Raman spectra of sc-SWCNTs before (black) and after (blue) Tf-ab functionalization.....	89
Appendix Figure B-6 Nyquist plot for EIS measurement of the gold disk surface upon exposing to increasing concentrations of transferrin.	90
Appendix Figure B-7 Relative transconductance change of sc-SWCNT FET devices for transferrin sensing using the Au electrode approach.....	91
Appendix Figure B-8 Western blot of Serum and CSF.....	92
Appendix Figure C-1 UV-vis-NIR spectrum of sc-SWCNT.	94
Appendix Figure C-2 Functionalization of enhanced green fluorescent protein (EGFP) antibody on a SWCNT FET device.	95
Appendix Figure C-3 XPS spectra of sc-SWCNT FET devices.....	96
Appendix Figure C-4 Comparison of source-drain current (I_d) and gate leakage current (I_g) of SAb-SWCNT FET device and NAb-SWCNT FET device.....	96
Appendix Figure C-5 FET characteristic curves and calibration curve of S antigen detection using S antibody functionalized FET devices.....	97
Appendix Figure C-6 FET characteristic curves and calibration-curve of N antigen detection using N antibody functionalized FET devices.	98

Preface

First, I wish to express my sincere gratitude to my research advisor, Dr. Alexander Star, for his help and guidance throughout my PhD study. This dissertation would not have been possible without his valuable advice, continuous support, and encouragement. I would also like to thank all my collaborators and colleagues inside and outside the Star group for their generous help and assistance at every stage of my research. Special thanks to Dr. Michael R. Shurin for his tremendous support and all the insightful comments and suggestions to improve my research. Thanks also to my other committee members, Dr. Haitao Liu and Dr. Stephen G. Weber for their helpful advice and suggestions.

My deepest gratitude also goes to my family, especially my parents and my husband. I would like to thank my parents for their love and support. They are always there for me, to give me comfort and guidance. Finally, to my husband, Shangmou, I will be forever grateful for him always believing in me, giving me strength and courage to pursue my dreams.

1.0 Introduction

1.1 Protein Detection

1.1.1 Significance

Detection of the presence and/or concentration of a certain type of proteins in a specimen is extremely important in biological research and clinical diagnostics. Developing improved methods for protein detection has demonstrated growing significance in life sciences research especially in recent years. In particular, the field of disease relevant protein detection has expanded rapidly as it is key to development of rapid diagnostic tools, providing better healthcare, and alleviating the burden on hospital resources.

One type of disease relevant protein that protein sensing generally focuses on is biomarker. A biomarker is a characteristic that can be objectively measured and often used as an indicator of a disease due to its specificity to the related disease.^{1, 2} The detection and quantification of a biomarker may provide a diagnosis at early stages, assess disease severity, and even evaluate the effectiveness of a treatment.^{3, 4} Moreover, biomarkers are present in body fluids, such as serum and plasma, urine and saliva, hence allow for easy accessible and non-invasive detections.⁵ Biomarker detection is especially vital for the diagnosis and treatment of cancers as it can help early cancer detection, cancer risk identification and monitor the disease progression, regression and recurrence,⁶ which is critical to improving patient survival rates.⁷ Much effort has been made, in the past few decades, to develop powerful, reliable, and cost-effective strategies for detection and monitoring of cancer biomarkers.⁸⁻¹² Meanwhile, substantial progress has also been made in

detection of biomarkers for other diseases, such as Alzheimer's disease¹³, Parkinson's disease¹⁴ and cardiovascular disease¹⁵.

Viral proteins are another type of disease relevant protein that protein sensing focuses on. Emerging and re-emerging infectious diseases have been major threats to global health and biosecurity.¹⁶ Infectious diseases, caused by viruses, such as influenza viruses, human immunodeficiency virus (HIV), severe acute respiratory syndrome coronavirus (SARS-CoV), and the newly emerged coronavirus SARS-CoV-2, are fast-spreading, causing worldwide social and economic disruption. Due to the high transmission rate and/or the absence of vaccine for some infectious diseases, rapid diagnosis and large-scale virus surveillance are crucial to controlling the outbreak. Therefore, rapid diagnostic tools, which offer rapid identification of virus infection and has the potential for low-cost point of care (POC) application, is in great need.

A virus infects human body by entering the host cells, insert its own generic materials in order to replicate itself then leave the host cells and spread inside the body, therefore viral proteins, depending on their type and pathogenesis, can be detected in various body fluids such as intracellular fluid, blood plasma or serum, and cerebrospinal fluid.¹⁷⁻²⁰ Albeit having lower sensitivity than the gold standard nucleic acid amplification tests (NAAT) in general, rapid viral antigen test provides fast detection of viral proteins, are relatively inexpensive, and can be used at the point of care, making it advantageous for screening.²¹ Nowadays, rapid antigen tests have been applied in clinical practices for the diagnoses of Ebola virus²², pandemic (H1N1) 2009^{23, 24} and COVID-19²⁵⁻²⁷.

1.1.2 Common Methods for Protein Detection

Common methods used for detection and quantification of biologically important proteins include immunoassay-based techniques, mass spectrometry, and biosensors.

Immunoassay-based techniques. Immunoassays are bioanalytical methods that utilize the specific interaction between antigen and antibody to detect and quantify target analyte. Immunoassay-based techniques have been widely used in bioanalytical settings such as clinical diagnostics, food testing and pharmaceutical industries.²⁸⁻³⁰ The versatility of immunoassay can be attributed to the high-throughput detection and high specificity toward a wide variety of analytes.

The most commonly used immunoassay is enzyme-linked immunosorbent assay (ELISA), which is routinely used for the detection of various proteins. In an ELISA, a target protein is first immobilized on a solid surface and then complexed to a detection antibody. The signal is produced via direct or secondary tag on the antibody and detected via absorbance.³¹ ELISA can be further classified into three main types: direct ELISA, indirect ELISA, and sandwich ELISA, depending on the different methods used for target protein immobilization and signal generation (**Figure 1-1**). Besides the colorimetric method used for the detection of proteins in immunoassays, fluorescent immunoassay (FIA) and chemiluminescence immunoassay (CLIA), the detection of which is based on fluorescent labeled molecules and light-generating molecules respectively, are usually

used to achieve higher sensitivity when the concentration of the target protein is low in the sample.³²⁻³⁵

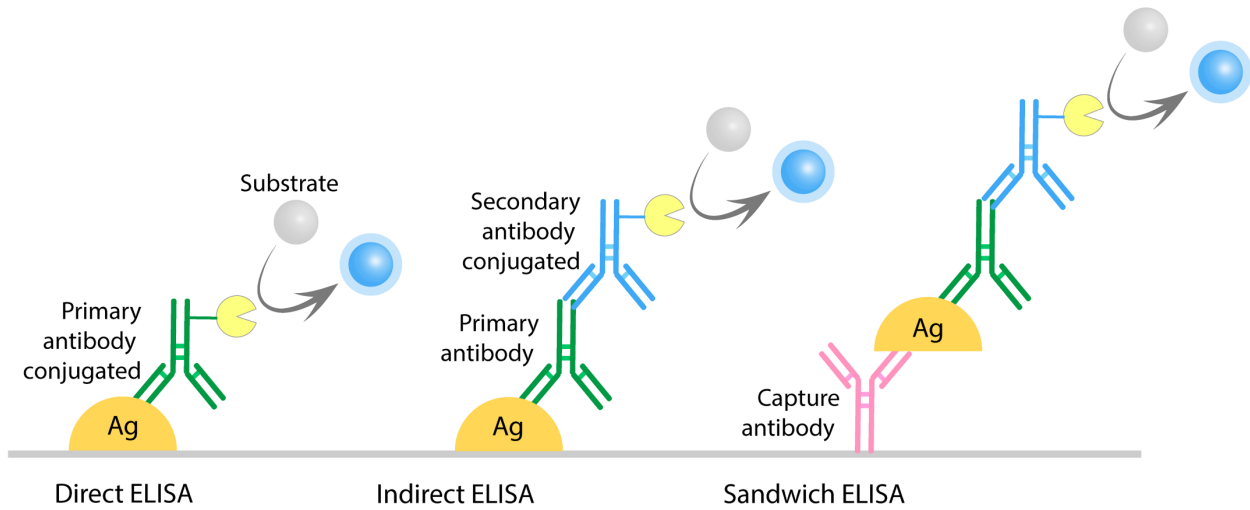


Figure 1-1 Schematic illustration of the three main types of ELISA. Left: Direct ELISA; Middle: Indirect ELISA; Right: Sandwich ELISA.

Unlike the aforementioned lab-based assays, another type of immunoassay that is amenable for POC applications is lateral flow immunoassay (LFA). LFA is simple, cheap, and easily mass-produced, therefore advantageous for rapid in-field protein detection in a low-resource setting.³⁶ Although traditional LFA-based techniques have relatively low sensitivity, with the growing need of rapid viral antigen test devices, extensive research has been done to improve the sensitivity of LFA to meet the high standards of viral disease diagnostics.³⁷⁻⁴⁰

Mass spectrometry. Mass spectrometry (MS) has become a primary method for the identification of proteins from complex mixtures.⁴¹ MS-based protein detection involves 2 steps: (1) proteins are first ionized and analyzed by a mass spectrometer, and (2) proteins are identified via database searching or *de novo* sequencing.⁴²

Fast and robust identification of protein became possible owing to the rapid growth of genomics and bioinformatics. Genomics provides complete genomic sequences, which are critical for identification of proteins by the correlation of mass spectrometric measurements of peptides with sequence database.⁴³ Recent advances in MS instruments also facilitate the increase in the level of automation, allowing the development of proteomic experiments with high-speed and high sensitivity.^{44, 45}

Biosensors. Biosensors are devices that are able to detect biological analytes such as proteins⁴⁶, DNA, antibodies⁴⁷, and even whole cells⁴⁸. The rapid development in the field of biosensors during the past three decades has brought new approaches for diseases diagnoses, drug delivery, health care, and environmental monitoring.⁴⁹ A typical biosensor usually consists of three fundamental components: (1) a biorecognition element to detect biological analytes, (2) a transducer to convert biological process to recordable electronic signal, and (3) a recording device (**Figure 1-2**). Analyte detection is enabled through the specific binding between the analyte and its receptor, creating a signal that can be converted to a measurable one and eventually displayed on a reader device.

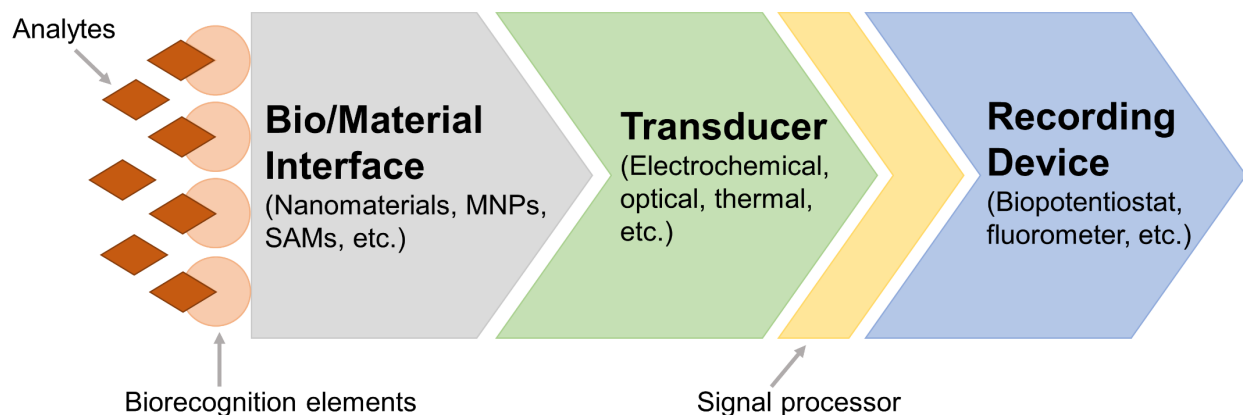


Figure 1-2 Schematic diagram of the three fundamental components of a biosensor. (Abbreviations: MNP: metal nanoparticles; SAM: self-assembled monolayer.)

Biosensors have several advantages for protein detection because of their high sensitivity and specificity, rapid responsiveness, versatility, capability of miniaturization, and potential affordability, showing great potential as diagnostic tools, and healthcare monitoring devices.⁵⁰

Among various types of biosensors, electrochemical biosensors have attracted interests from many researchers. Electrochemical biosensors detect the binding of analyte to the sensory interface through generated perturbation in current or voltage signal, offering an excellent platform for fast and label-free detection of proteins.^{46, 51, 52}

1.1.3 Challenges

Even with the enormous progresses made in the field of protein sensing in recent years, there are still challenges limiting protein sensing techniques for their applications in clinical practices. The first challenge is the low concentration of proteins presents in the specimen. Unlike NAAT, which amplifies the generic material from viruses to meet the requirement for an accurate

reading from the detector, protein detection investigates the presence of a small number of biomarkers or viral antigens that cannot be pre-concentrated without complex sample processing. Therefore, an ultrasensitive detection method is required to produce accurate and reliable results.

Another challenge faced during protein detection in physiological relevant environment is the complexity of the specimen. Body fluid, such as serum and CSF, contains a large number of proteins that can possibly interfere with the detection results or lead to fouling of biosensors. This requires protein detection in complex biological samples to have high specificity to minimize false positive results.

Current development of protein biosensors is mainly focusing on enhancing the sensitivity, selectivity, and stability toward their real-life applications.⁵³ Other challenges include reproducibility, long-term stability, instrument accessibility and affordability should also be concerned for the future development of protein detection.

1.2 Single-Walled Carbon Nanotubes and their Applications in Protein Detection

Carbon nanotubes (CNTs) are seamless cylindrical tubes comprised of graphene sheets. There are many different types of CNTs, varying in lengths, thickness, number of layers. Depending on the number of rolled graphene sheet layers, CNTs are typically classified as single-walled carbon nanotubes (SWCNTs) and multiwalled carbon nanotubes (MWCNTs). Depending on how the graphene sheet has rolled up to form the tube, SWCNTs can be metallic or semiconducting.⁵⁴ In this dissertation, single-walled carbon nanotubes were used as the sensing material for protein detection.

1.2.1 Sorting of Single-Walled Carbon Nanotubes

Single-walled carbon nanotubes have demonstrated remarkable electronic and mechanical properties, making them an ideal material for biosensing and other bioelectronic devices.⁵⁵ The properties of SWCNTs are largely dependent on their structure. One way to classify SWCNTs is based on the diameter and helicity of a SWCNT, which are characterized by a chiral vector L . $L = na + mb \equiv (n, m)$, where a and b are the graphene lattice vector, and m and n are integers. Therefore, the (n, m) indices define the circumference and the chiral angle of the nanotube.⁵⁶ If $n = 0$ or $m = 0$, the nanotubes are called “zigzag”. If $n = m$, the nanotubes are called “armchair”. Other nanotubes, the (n, m) indices of which do not satisfy any of the aforementioned rules, are chiral (Figure 1-3).⁵⁴

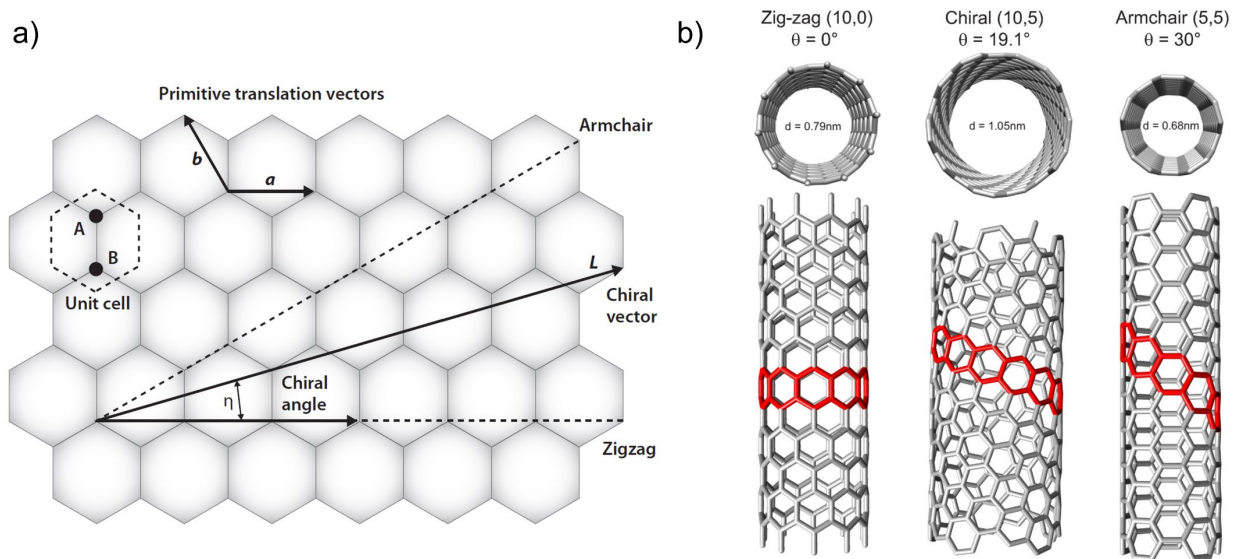


Figure 1-3 Classification of SWCNTs by chiral indices. (a) Schematic of a graphene sheet with chiral vector L , where $L = na + mb \equiv (n, m)$. (n, m) indices determine the semiconducting or metallic property of the CNTs. Adapted from Ref. 54. In the case of $m = n$, the nanotube has armchair structure. In the case of $m =$

0 or $n = 0$, the nanotube has zigzag structure. Otherwise, the nanotube is chiral. (b) Examples of “zigzag” (left), chiral (middle), and “armchair” (right) SWCNT. Adapted from Ref. 57.

The (n, m) indices also determine the semiconducting and metallic property of SWCNTs. When $m - n = 3l$ (where l is an integer), the SWCNTs are predicted to be metallic; Otherwise, they are predicted to be semiconducting.⁵⁸ As a result, the ratio of metallic and semiconducting nanotubes appears to be one to two.

In order to achieve high-performance of biosensing devices, a high purity of semiconducting (sc-) SWCNTs are often required.⁵⁹ High-purity sc-SWCNTs provide high mobilities, high energy-efficiency and high on/off ratios for transistors, making them a promising material for developing a variety of electronic devices, such as field-effect transistors,^{60, 61} electronic skins,⁶² logic circuits,⁶³ and computers.⁶⁴

To date, methods reported for extracting sc-SWCNTs from their metallic counterpart include dielectrophoresis (DEP), chromatography, ultracentrifugation, aqueous two-phase separation (ATP), and conjugated polymer extraction (CPE).⁶⁵

DEP for sorting of SWCNTs is dependent on the different dielectric constant of m-SWCNTs and sc-SWCNTs, resulting in an opposite movement of m-SWCNTs and sc-SWCNTs along the electric field.⁶⁶ Chromatography is a simple, easy, and scalable method for sorting SWCNTs. The separation of m-SWCNTs and sc-SWCNTs is based on the selective adsorption of m-SWCNTs and sc-SWCNTs on the column material.^{67, 68}

Ultracentrifugation sorts SWCNTs according to their sedimentation coefficient, which is determined by multiple parameters, such as length, diameter, and buoyant density. Conventional ultracentrifugation utilizes a constant density medium, showing low separation efficiency due to convolution among multiple parameters.⁶⁹ Density gradient ultracentrifugation (DGU) addresses

this issue by using a gradient medium, and depending on the process conditions, SWCNTs can be resolved by length, diameter, (n, m) structures, and even handedness.^{65, 70}

Sorting SWCNTs via ATP is achieved by mixing polyethylene glycol (PEG) and dextran (DEX), forming two immiscible aqueous phases, and each has a different affinity toward SWCNTs. SWCNTs therefore partition between the PEG-rich phase and DEX-rich phase due to the different partition coefficient, resulted from the different chemical potential of SWCNTs with different (n, m) s.^{71, 72} The partition of SWCNTs can be further controlled by altering surfactants and their concentrations.⁷³ ATP is a promising technique for sorting SWCNTs due to its low equipment requirement and high energy and time efficiency.⁷²

CPE has been demonstrated to be an effective technique to isolate SWCNTs with specific chirality with high selectivity (>99.9%)⁷⁴ and high yield (>10%).⁷⁵ Conjugated polymers, with extensive pi-conjugated structures, interact with SWCNTs through non-covalent $\pi-\pi$ interactions, and can selectively disperse sc-SWCNTs.⁷⁶ The process of CPE includes two steps: (1) Sonicate the mixture of SWCNTs and conjugated polymers to disperse the SWCNTs, and (2) Centrifuge to settle impurities and m-SWCNTs, leaving the sc-SWCNTs in the supernatant for subsequent analysis.⁷⁷ A variety of conjugated polymer has been investigated for sorting of SWCNTs. The selectivity of these polymers is strongly dependent on the diameter and chiral angles of SWCNTs, thus making CPE an effective way to separate SWCNTs with narrow diameter distribution.^{78, 79}

1.2.2 Functionalization of Single-Walled Carbon Nanotubes

The immobilization of the biorecognition element to the sensor surface is a central concern for the development of biosensors. The conformation, stability and activity of the biorecognition

element can dictate the sensing performance of a biosensor.⁸⁰ For SWCNT-based biosensors, the immobilization of the biorecognition element, such as antibody, aptamer, and peptide, enables the biocompatibility, specificity and enhanced sensitivity of the biosensor for protein detection.

Generally, the functionalization of SWCNTs can be classified as non-covalent approaches and covalent approaches (**Figure 1-4**).⁸¹ Non-covalent functionalization of SWCNTs can be achieved through π - π stacking between the aromatic moieties and the π -network in SWCNTs, electrostatic interactions, and hydrophobic interactions.⁸² Aromatic molecules (for example, pyrene) and conjugated polymers⁸³ are usually non-covalently functionalized on SWCNTs through π - π stacking. Moreover, the non-covalent functionalization of an aromatic cross-linker can open opportunities for further functionalization of desired chemistry.⁸⁴ Electrostatic interactions can be observed between charged species and SWCNTs, thus some proteins can be absorbed on SWCNTs non-covalently.⁸⁵ Amphiphilic molecules can be non-covalently functionalized on SWCNTs through hydrophobic interactions. The hydrophobic side of the amphiphile can interact with the SWCNTs, forming micelles in the solution.⁸⁶ Non-covalent approaches for biomolecules to attach to SWCNTs can retain the intrinsic properties of SWCNTs, while remarkably improve the solubility of SWCNTs.⁸⁷

Covalent functionalization of SWCNTs, on the other hand, is more robust and versatile. During covalent functionalization of SWCNTs, chemical bonds form on carbon nanotube sidewalls and at the two ends through chemical reactions. One of the commonly used methods to immobilize antigens and antibodies on SWCNTs is 1-ethyl-3-(3-dimethylaminopropyl)carbodiimide (EDC)/N-hydroxysulfosuccinimide (sulfo-NHS) coupling. This method couples the amine group containing species to the carboxylic acid groups exist on the side walls of SWCNTs. To be specific, EDC first activates the carboxylic acid groups to form an

unstable O-acylisourea intermediate, which can be easily displaced by sulfo-NHS, forming a more stable intermediate, allowing for more efficient conjugation of biomolecules with primary amine groups in physiologically relevant environment.⁸⁸

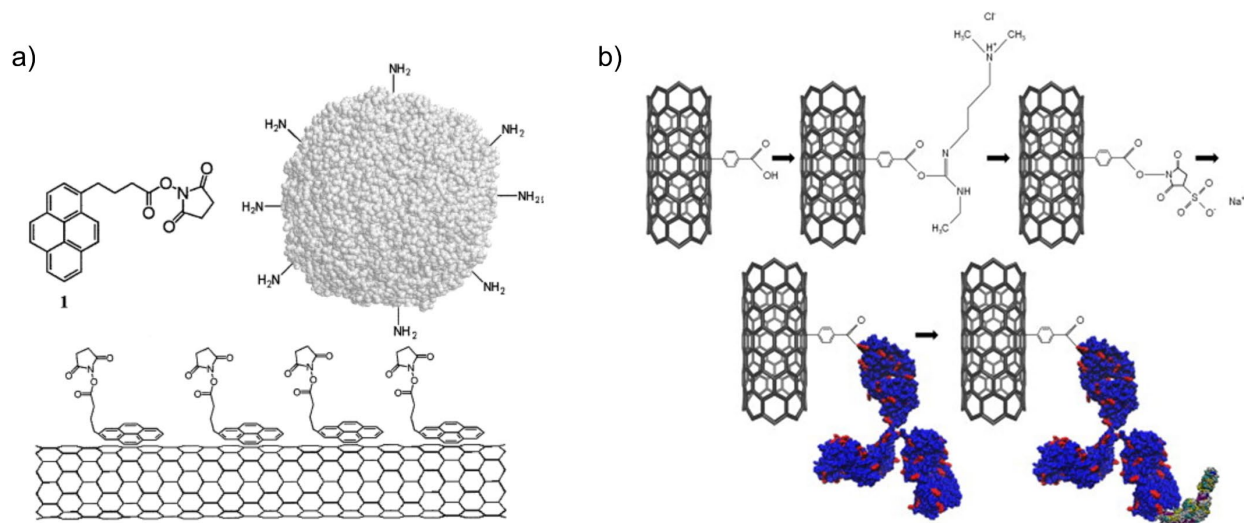


Figure 1-4 Noncovalent and covalent functionalization of SWCNTs. (a) Example of noncovalent functionalization of SWCNTs. 1-pyrenebutanoic acid, succinimidyl ester (1) was anchored on SWCNT surface via pyrene π - π stacking. A protein can then be immobilized on a SWCNT via the reaction between amine groups and the anchored succinimidyl ester to form amide bonds. Adapted with permission from Chen et al., *J. Am. Chem. Soc.* 2001, 123, 3838–3839.⁸⁹ Copyright 2001 American Chemical Society. (b) Example of covalent functionalization of SWCNTs. Lyme antibody was immobilized on a SWCNT via EDC/sulfo-NHS coupling for the detection of Lyme flagellar antigen. Adapted from Ref. 90.

Noble metal nanoparticles (NPs), such as Pt, Au, and Ag, are also widely functionalized on to SWCNTs to synthesize hybrid nanomaterials. Metal NPs provide strong charge scattering sites on SWCNT network, and create interfacial “nano” Schottky barrier on SWCNTs, resulting in highly sensitive functional hybrids for chemical sensing.⁹¹ Metal NPs-decorated SWCNTs have

been applied in gas sensing⁹² and sensor arrays enabling biosensing using machine learning approach.⁹³

SWCNTs/Au NPs composites have also been used as substrates for surface enhanced Raman spectroscopy (SERS).⁹⁴ SWCNTs provide a large and uniform surface area due to their large surface-to-volume ratio, which will result in enrichment of metal nanoparticles and target biomolecules, and therefore enhance the Raman signal.⁹⁴ Therefore, by combining information obtained from Raman spectroscopy and electrical measurements of Au NPs-decorated SWCNT biosensors, one can gain better insight into the chemical and biological interactions on the device surface, which further aid in the design of more sensitive and specific biosensors.⁹⁵

1.2.3 Characterization Methods of Single-Walled Carbon Nanotubes

Characterization methods of SWCNTs are essential as they provide information on electrical and structural characteristics of SWCNTs, and aid in understanding the changes resulted from surface modification of SWCNTs. Analytical techniques that are commonly used to characterize SWCNTs include Raman spectroscopy, ultraviolet-visible-near-infrared (UV-vis-NIR) absorption spectroscopy, and scanning electron microscopy (SEM).

Raman spectroscopy. Raman spectroscopy is one of the most powerful tools to characterize SWCNTs. Both electronic and structural properties of SWCNTs can be revealed by Raman spectra. There are three featured peaks in a typical Raman spectrum of SWCNTs that are useful for characterization of SWCNTs, namely radial breathing mode (RBM), D band, and G band (**Figure 1-5a**). The peak present in the range of 150 cm^{-1} to 300 cm^{-1} is the RBM peak. RBM results from the radial expansion-contraction of carbon atoms. The frequency of RBM peak is dependent on the diameter of the nanotube. D band, usually seen between 1300 cm^{-1} to 1400 cm^{-1}

¹, is related to the defects on the nanotube structure. G band originates from the in-plane stretching mode of C-C bonds and is the most intense peak around 1600 cm⁻¹.⁹⁶ The intensity ratio between D band and G band (I_D/I_G) is often used to evaluate the functionalization degree of SWCNTs.⁹⁷ Moreover, Raman spectroscopy also shows chiral-selectivity with different laser irradiation wavelength, thus enabling discrimination between sc-SWCNTs and m-SWCNTs, and purity assessment of sorted SWCNTs.^{98,99}

UV-vis-NIR absorption spectroscopy. UV-vis-NIR absorption spectroscopy measures the optical absorption of SWCNTs in the UV-vis-NIR region, which originates from inter-band electronic transition from van Hove singularities of the valence band to their corresponding energy level in the conduction band.¹⁰⁰ Therefore, UV-vis-NIR absorption spectroscopy is suitable for probing electronic structure of SWCNTs. SWCNTs give rise to different characteristic peaks in the UV-vis-NIR region depending on their metallicity (**Figure 1-5b**). Sc-SWCNTs exhibits two peaks denoted as S₁₁ and S₂₂, whereas m-SWCNTs have their characteristic peak (M₁₁) around 700 nm.^{101,102}

Scanning electron microscopy (SEM). High resolution SEM is a powerful technique for imaging SWCNTs as it provides three-dimensional morphological information on SWCNT networks with high resolution and high efficiency (**Figure 1-5c**).¹⁰³ SEM utilizes a beam of high-energy electrons to generate signal at the surface of a solid sample, forming an image. To be specific, accelerated electrons are focused into a beam and come into contact with a sample, scanning the sample controlled by scanning coils. Various signals are produced due to electron beam-specimen interactions, among which the secondary electrons (SEs) are collected by the detector, and the intensity of the signal is displayed as brightness on a screen.¹⁰⁴

The visualization of detailed structures under SEM requires optimal conductivity of the sample. Therefore, non-conductive and low-conductive samples can be covered with a conductive coating before imaging. This can be achieved by sputter coating a conductive thin film such as gold/palladium, Pt or Cr.¹⁰⁵

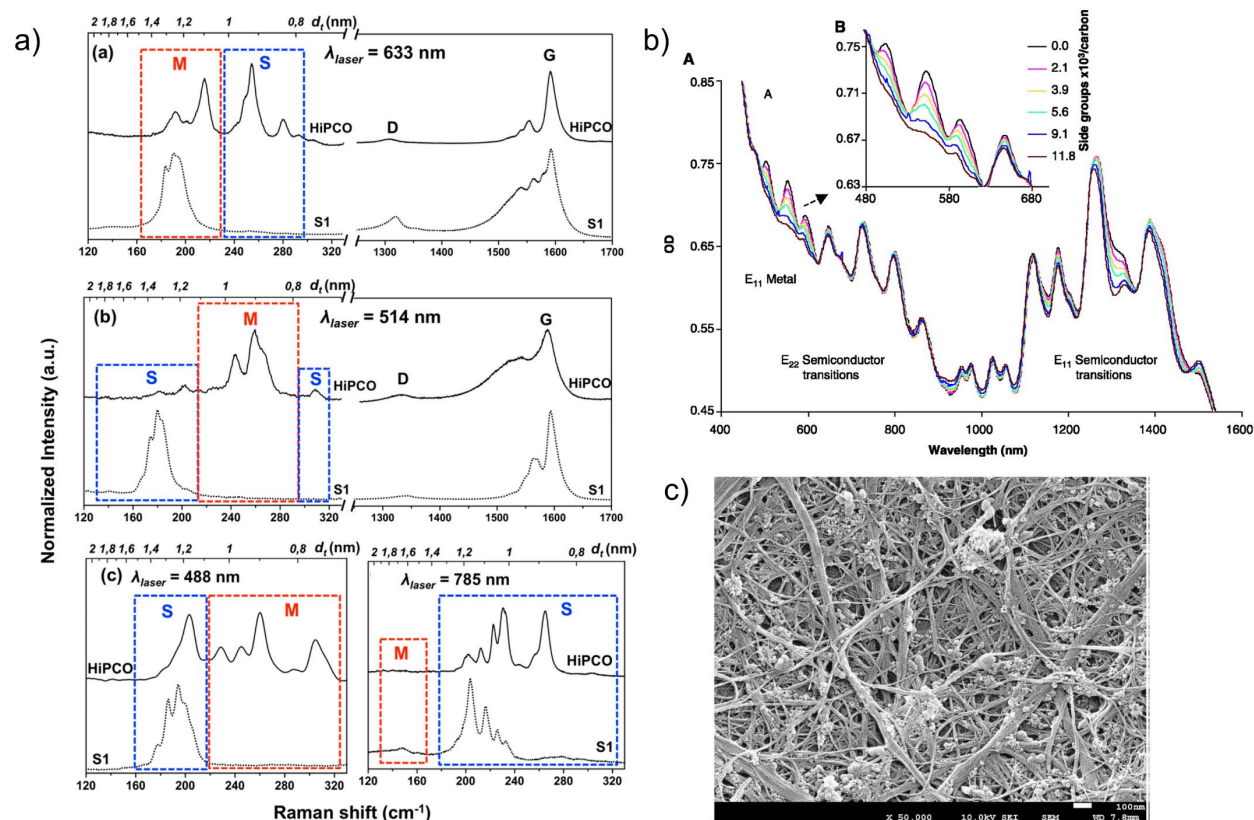


Figure 1-5 Common techniques for characterization of SWCNTs. (a) Raman spectra of two different types (S1 and HiPCO) of SWCNTs under excitation of four different wavelengths. Different types of SWCNTs, depending on their different sc-SWCNTs and m-SWCNTs content, show different RBM peaks correspond to sc-SWCNT and m-SWCNT regions, as well as different shapes of D and G band. Moreover, laser excitation at different wavelength can selectively excite sc-SWCNTs and m-SWCNTs. Adapted from Ref. 99 (<https://pubs.acs.org/doi/10.1021/acs.analchem.7b03712>) with permission from ACS.* (b) UV-vis-NIR spectra

* Further permissions related to this figure should be directed to the ACS.

of sodium dodecyl sulfate-suspended SWCNTs during selective functionalization controlled by differences in the electronic structure of SWCNTs. The gradual decrease of M_{11} peak (inset) suggests a selective functionalization of m-SWCNTs with diazonium salts, while keeping the semiconducting content unaffected. From Strano et al., *Science* 2003, 301, 1519–1522.¹⁰¹ Reprinted with permission from AAAS. (c) SEM images of poly(3,4-ethylenedioxythiophene)-SWCNT films spray-coated on a polyethylene terephthalate substrate.

Adapted from Ref. 103.

Other techniques, such as atomic force microscopy (AFM) and X-ray photoelectron spectroscopy (XPS), are also used to characterize SWCNTs, providing information on morphology and elemental composition of both SWCNTs and biomolecule modified SWCNTs.

1.2.4 Single-Walled Carbon Nanotube-Based Field-Effect Transistors for Protein Detection

Protein detection with field-effect transistors (FET) has been an area of high interest. Owing to the high sensitivity, rapid, label-free, and real-time sensing offered by FET-based biosensors,¹⁰⁶ they have been applied in the detection of a wide variety of disease relevant proteins.¹⁰⁷

A field-effect transistor (FET) device consists of a source (S) electrode and a drain (D) electrode fabricated on a substrate, semiconductor channels that connect S and D, and a control electrode called the gate. In a FET device, electrical current flows from source to drain through the semiconductor channel. A gate voltage is applied to the gate electrode and imposes an electric field into the device, which regulates the charge carrier flow between source and drain. Consequently, the conductivity of the device changes as varying gate voltage (**Figure 1-6a**).

SWCNTs are an ideal sensing material for FET biosensors because of two reasons: (1) They are very sensitive to changes in their environment. (2) The easy and versatile

functionalization of SWCNTs. SWCNT-based FET biosensors are dependent on the interactions of biomolecules with the semiconducting SWCNT channel causing alteration in the dielectric environment, charge carrier density, work function modulation, or charge transfer into the nanotube. At the same time, SWCNT-based FET can be functionalized with custom-designed selective chemistry to preferentially interact with desired biomolecules, demonstrating excellent sensing behavior in complex media, such as human tears and sweat.¹⁰⁸

Rich information regarding the biorecognition process and sensing mechanism can be extracted from the changes in FET transfer characteristics, which is viewed by plotting the source-drain current (I_d) or conductance (G) against the gate voltage (V_g). Several features are selected to accurately describe the changes in FET transfer curves, including (1) relative current/conductance change at certain gate voltage, (2) relative change in transconductance (g_m), and (3) threshold voltage (V_{th}) shift (**Figure 1-6b**).¹⁰⁹

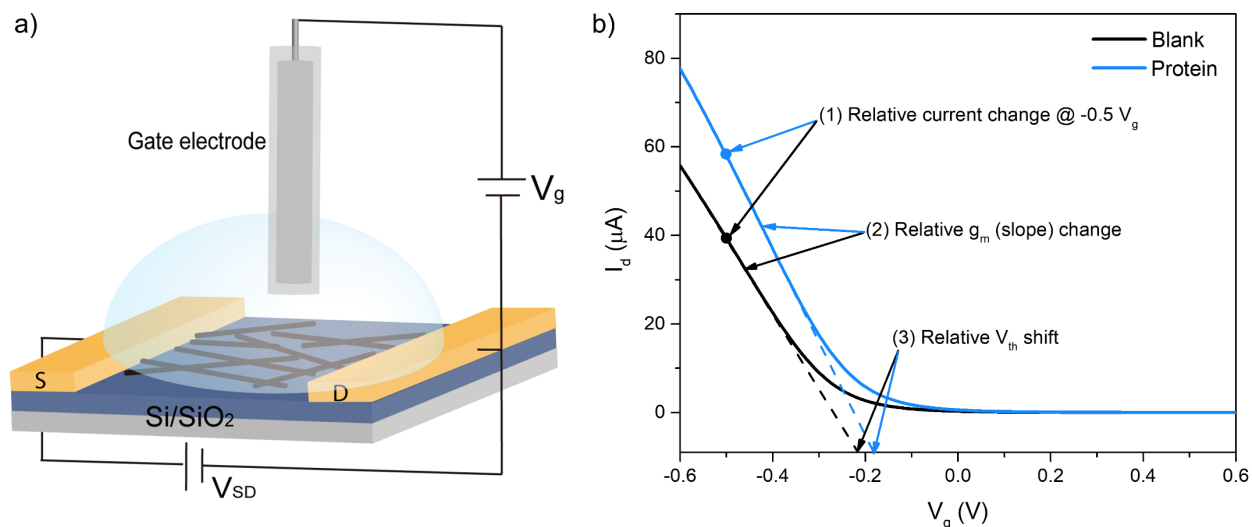


Figure 1-6 Illustration of a SWCNT-based FET device and FET transfer characteristics. (a) Schematic illustration of a SWCNT-based FET device. SWCNTs form a network on a Si/SiO₂ substrate between source and drain gold electrodes. (b) Typical FET transfer curves constructed by plotting source-drain current (I_d)

versus gate voltage (V_g). Three features are selected to study FET characteristics change during biosensing: (1) Relative current change @ $-0.5 V_g$; (2) Relative transconductance (g_m) change, where g_m can be calculated by the slope of the linear range of FET transfer curves; (3) Relative threshold voltage (V_{th}) change.

In this dissertation, high-purity sc-SWCNTs were used to develop FET biosensors for protein detection. In Chapter 2, sc-SWCNTs were decorated with Au NPs to probe the Ca^{2+} -induced conformational change of calmodulin. The sensing performance was also compared with un-SWCNT-based FET device. In Chapter 3, a three-step strategy was developed to detect CSF leak in a short turnaround time. The three-step strategy includes two steps of separation using affinity columns to isolate $\beta 2$ -transferrin from other proteins in a CSF sample, and a third step using sc-SWCNT-based FET biosensors for detection of $\beta 2$ -transferrin. Three different sensing configurations for the sc-SWCNT-based FET biosensor were investigated for obtaining the optimal $\beta 2$ -Tf sensing results. In Chapter 4, sc-SWCNT-based FET biosensors were functionalized with SARS-CoV-2 antibody and applied in rapid detection of SARS-CoV-2 antigens. The results showed that the SARS-CoV-2 antibody functionalized sc-SWCNT FET biosensor has achieved sub-fg/mL detection of SARS-CoV-2 antigens in calibration samples and an 82% accuracy with NAAT positive nasopharyngeal swab samples.

2.0 Probing Ca²⁺-Induced Conformational Change of Calmodulin with Gold Nanoparticle-Decorated Single-Walled Carbon Nanotube-Based Field-Effect Transistors

2.1 Chapter Preface

The aim of this work was to study the sensing performance of gold nanoparticle-decorated high-purity sc-SWCNT-based FET sensing devices by comparing with that of gold nanoparticle-decorated un-SWCNT FET devices for the detection of Ca²⁺-induced conformational change of calmodulin. The material contained in this chapter was published in *Nanoscale* in **2019**. The full citation is listed as Reference 110 in the bibliography section. Reproduced by permission of The Royal Society of Chemistry.

List of Authors: Wenting Shao, Seth C. Burkert, David L. White, Valerie L. Scott, Jianfu Ding, Zhao Li, Jianying Ouyang, François Lapointe, Patrick R. Malenfant, Kabirul Islam and Alexander Star

2.2 Introduction

Single-walled carbon nanotubes (SWCNTs) are considered to be an ideal material for electronic devices, such as field-effect transistors (FETs), due to their outstanding electronic and mechanical properties.¹¹¹⁻¹¹⁷ The properties of SWCNTs are largely dependent on their structure, therefore the control of SWCNT structure, such as diameter and chirality, is crucial for developing high-performance electronic devices.^{59, 117} Unsorted (un-) SWCNTs contain a mixture of metallic

(m-) and semiconducting (sc-) SWCNTs.⁵⁸ However, in order to achieve high-performance FET devices with high carrier mobility and high on/off ratios, a high purity of sc-SWCNTs is often required.^{59, 118} Common methods for separating m-SWCNTs from sc-SWCNTs, include density gradient ultracentrifugation (DGU)¹¹⁹, aqueous two-phase separation (ATP)¹²⁰, and conjugated polymer extraction (CPE)^{121, 122}. Among these methods, a hybrid-CPE protocol has been reported to yield sc-SWCNTs with a purity >99.9%.^{74, 98} Recently, high-purity semiconducting SWCNTs have shown promise for chemical sensing applications, such as highly sensitive gas detection¹²³⁻¹²⁵ and humidity monitoring.¹²⁶ The high sensitivity afforded by sc-SWCNT FETs seen in gas sensing could also be employed in the development of ultrasensitive biosensors, such as aptasensors^{127, 128} and label-free protein sensors.^{129, 130} Here we applied high purity sc-SWCNT based FET devices to the investigation of the Ca²⁺ binding-induced conformational change of calmodulin (CaM).

CaM is a calcium binding messenger protein that modulates calcium transfer in many crucial processes in the human body, and ultimately modulates a variety of cellular processes.^{131, 132} CaM is a ubiquitous, multifunctional protein that regulates over 30 different proteins and enzymes. As a highly conserved protein, CaM consists of only 148 amino acids, has a length of 65 Å, and a diameter of approximately 30 Å.¹³³ The small dimensions make CaM a suitable biological species to study on a carbon nanotube FET device because the conformational change of CaM can be monitored without being adversely affected by ionic screening effects when measured in relatively low ionic strength solutions. One interesting feature of the Ca²⁺-induced conformational change of CaM is that, upon Ca²⁺ binding, CaM changes from a closed to an open form, exposing the solvent accessible hydrophobic surface, which enables the recognition and binding of CaM to its target protein.¹³⁴ Therefore the conformational change of CaM plays a vital

role in calcium signal transduction in the human body. Moreover, understanding of CaM structure could allow for the development of better protein conformational switches with applications in biosensors, diagnostic tools, and therapeutic agents.¹³⁵ Nuclear magnetic resonance (NMR) spectroscopy¹³⁴ and X-ray crystallography¹³⁶ are the primary techniques to study the protein conformational change, but these powerful instrumental methods have a limited miniaturization potential. Other methods such as fluorescence resonance energy transfer (FRET),¹³⁷ DNA nanolevers,¹³⁸ and atomic force microscopy (AFM)¹³⁹ have the advantage of single-molecule detection, however often require complex sample preparation such as protein labeling.

FET devices comprised of individual SWCNTs have already been used for real-time monitoring of biomolecular processes on the surface of SWCNTs, including single-molecule lysozyme dynamics¹⁴⁰ and the conformational dynamics of individual DNA G-quadruplex structures.¹⁴¹ However, these approaches necessitate e-beam lithography and covalent attachment of biomolecules to nanotube sidewalls through patterning or point-defects. Herein, by utilizing networks of sc-SWCNT based FET devices, we detected the calcium ion-dependent conformational change of CaM without further modification of the protein or nanotubes. We measured FET characteristics to investigate steady state changes associated with ion-induced protein conformational changes and to explore the sensing performance and mechanism of sc-SWCNT FETs.

By comparing un-SWCNT and sc-SWCNT based FET devices, we further investigated effects of nanotube structure and functionalization on the biosensing performance. Purified arc-discharge un-SWCNTs have an unmodified graphitic surface but contain a mixture of m-SWCNTs and sc-SWCNTs, whereas semiconductor enriched sc-SWCNTs have a polyfluorene-dodecyl (PFDD) polymer coating due to the sorting process. Additionally, polymer coating in sc-SWCNTs

can affect AuNP deposition and CaM binding in comparison to un-SWCNTs, which in turn can change biosensor performance. In addition to investigating FET transfer characteristics, we used ultraviolet-visible-near infrared (UV-vis-NIR) absorption and Raman spectroscopies to get additional insight into the electronic structure of the nanotube-gold nanoparticle-protein system.

2.3 Experimental Section

Carbon nanotube materials. Commercial unsorted single-walled carbon nanotubes (P2-SWNT, Carbon Solutions Inc.) and semiconducting single-walled carbon nanotubes were prepared according to reference 15 but may also be obtained commercially (IsoSol-S100, Raymor Industries Inc.).

Device fabrication and decoration with gold nanoparticles. Interdigitated gold electrodes (channel length of 10 μm) were patterned on a Si/SiO₂ substrate using photolithography. Un-SWCNT solution was prepared at 0.01 mg/mL in DMF, and sc-SWCNT solution was prepared at 0.05 mg/mL in toluene. SWCNTs were then deposited between gold electrodes via DEP with an ac frequency of 10 MHz for un-SWCNT, and 100 kHz for sc-SWCNT, applied bias voltage of 10 V, and bias duration of 60 s for un-SWCNT and 120 s for sc-SWCNT. Gold nanoparticle decoration on SWCNTs was achieved through bulk electrolysis from a 1 mM AuCl₃ solution in 0.1 M HCl using a 3-electrode system with a Ag/AgCl reference electrode, Pt counter electrode, and SWCNTs acting as the working electrode. A -0.2 V potential was applied for 30 s for formation of AuNPs ranging in diameter from 10 nm to 100 nm.

Calmodulin (CaM) was attached to the AuNPs decorated SWCNTs by a 12-hour incubation with 50 μL of a 500 $\mu\text{g}/\text{mL}$ CaM solution in 1 mM phosphate buffered saline (PBS) on the devices, followed by thorough rinsing with nanopure water.

FET measurements. FET characteristics of both un- and sc-SWCNT FET devices were studied employing liquid-gated FET device configuration. Dulbecco's phosphate buffered saline (DPBS, 0.01X, Lonza) was used as the gating electrolyte. Characteristic FET curves, i.e., source-drain conductance (G) versus gate voltage (V_g), were taken by sweeping the gate voltage from +0.6 to $-0.6 V_g$ versus a Ag/AgCl reference electrode with a fixed source-drain voltage of 50 mV.

To probe the Ca^{2+} -induced conformational change of CaM, a series of CaCl_2 solution was added to the device from the lowest concentration to the highest concentration. The device was first incubated with CaCl_2 solution for 2 min, then rinsed with nanopure water, and measured in 0.01X DPBS as the electrolyte medium with gate voltage sweeping from +0.6 V to -0.6 V.

Control experiments were performed employing the same liquid-gated FET configuration. For all FET measurements, the device was first incubated with the analyte for 2 min, then rinsed with nanopure water, and measured in 0.01X DPBS as the electrolyte medium with gate voltage sweeping from +0.6 V to -0.6 V.

Raman measurements. XplorA Raman-AFM/TERS system was used to record all Raman spectra. Raman spectra were recorded using 638 nm (24 mW) and 785 nm (100 mW) laser excitation operating at 1% power.

UV-vis-NIR absorption spectroscopy. UV-vis-NIR spectra were collected using a Perkin-Elmer Lambda 900 UV-vis-NIR spectrophotometer. Un-SWCNTs were spray casted on a 1" X 1" quartz slide using a commercial air gun (Iwata, Inc), and sc-SWCNTs were drop casted on a 1" X 1" quartz slide. AuNPs were deposited on both types of SWCNTs through bulk

electrolysis from a 1 mM AuCl₃ solution in 0.1 M HCl using a 3-electrode system. Both slides were then incubated with CaM solution (500 µg/mL in 1 mM PBS) to allow CaM binding to the nanomaterial surfaces.

SEM characterization. SEM images were taken on an SEM ZEISS Sigma500 VP with an accelerating voltage of 3 kV. Devices were sputter coated with 8 nm palladium before SEM imaging to limit charging.

AFM. Bruker multimode 8 utilizing a Veeco Nanoscope IIIa controller in tapping mode was used to collect AFM data. AppNano ACST-SS probes having nominal radius of 1-2 nm were operated at a frequency of 160–225 kHz, an amplitude set point of 1.70–1.75 V, and a drive amplitude of 100–300 mV. Images were processed in Gywiddon.

Circular dichroism (CD) measurements. Circular dichroism spectra were recorded on an Olis circular dichroism spectrophotometer. 1.0 mm quartz cuvettes were used for all measurements. 0.1 mg/mL Ca²⁺ free CaM and 0.1 mg/mL CaM solutions containing 10⁻¹⁵ M, 10⁻¹² M, 10⁻⁹ M, 10⁻⁶ M and 10⁻³ M Ca²⁺ were prepared for CD measurements.

Expression of EGFP-CaM. A plasmid for mammalian expression of histidine tagged EGFP-calmodulin (EGFP-CaM) was obtained from Addgene (Plasmid # 47602). Human embryonic kidney 293T (HEK293T) cells were cultured in a T150 Flask (Corning) in Dulbecco's Modified Eagle's Media (DMEM) media supplemented with 10% Fetal Bovine Serum (FBS) at 37°C with 5% CO₂. At 80% cellular confluency, 25 µg of plasmid and 62.5 µg lipofectamine were added to 1.75 mL Optimem media and incubated at room temperature for 5 minutes, separately. Next, the tubes were combined and incubated for 20 minutes. This was added to the cells with fresh DMEM 10% FBS. The cells were grown for an additional 24 hours and collected. Cells were resuspended in 750 µL lysis buffer containing: 50 mM tris pH 8.0, 200 mM NaCl, 10% glycerol,

1 mM phenylmethylsulfonyl fluoride (PMSF), 0.1% triton X, 1x protease inhibitor (Pierce), and small amounts of DNase and lysozyme. Following a 10-minute incubation on ice, the cells were subjected to sonication at 100 mA for five 60 second pulses with a 30 second resting period in between. Samples were then centrifuged at 15,000 rpm for 10 minutes to pellet cell debris. The protein was then purified by HisPur Nickel-NTA resin (ThermoFisher). Ni-NTA resin was prepared by washing 100 μ L of the slurry with 5 column volumes (CV) water followed by 5 CV wash buffer: 50 mM tris pH 8.0, 200 mM NaCl, 10% glycerol, 25 mM imidazole, 1x protease inhibitor, and 1 mM PMSF. The lysate was applied to the resin and gently mixed for 1 hour at 4°C. Next, the beads were washed with 20 CV wash buffer. 600 μ L of elution buffer containing 50 mM tris pH 8.0, 200 mM NaCl, 400 mM Imidazole, 10% glycerol, and 1 mM PMSF was applied to the column in 100 μ L aliquots. All elutions containing protein were combined and concentrated (Sartorius centrifugal concentrator). Protein was quantified via SDS-PAGE with BSA standards (Biorad).

Fluorescence imaging. Fluorescence images were obtained using an Olympus 1X81/1X2-UCB microscope. 20 μ L of 1 μ M EGFP-CaM (containing 0.5mM ethylene glycol-bis(β -aminoethyl ether)-N,N,N',N'-tetraacetic acid, EGTA) was incubated on Au-SWCNT surface at 4°C overnight, and rinsed with nanopure water. Fluorescence images were captured under excitation of 489 nm and 655 nm. 20 μ L of 1 M CaCl₂ was then dropcasted on the device surface to induce the conformational change of EGFP-CaM. After rinsing the surface with nanopure water, fluorescence images were captured under the same excitation wavelengths.

2.4 Results and Discussion

For all studies, carbon nanotubes were deposited using dielectrophoresis (DEP) between interdigitated gold electrodes on Si/SiO₂ wafers. AuNPs were then deposited from a solution of AuCl₃ *via* bulk electrolysis in a three-electrode system, resulting in AuNPs anchoring to the oxygen-containing defect sites on carbon nanotubes.^{95, 109} CaM functionalization of AuNP decorated SWCNTs (Au-SWCNT) was performed by incubating the chip with 500 µg/mL CaM solution for 12 h at room temperature, followed by rinsing with nanopure (18.2 MΩ) water.

Scanning electron microscopy (SEM) was utilized to characterize the difference in surface morphology after CaM functionalization for both types of FET devices (**Figure 2-1**). **Figure 2-1a and b** show the morphology and distribution of AuNPs on un-SWCNT and sc-SWCNT, respectively. For both types of SWCNT, nanotube networks were deposited between fingers of interdigitated gold electrodes. The un-SWCNTs tended to form large bundles and rope-like structures while sc-SWCNTs, due to polymer coating on their surfaces, did not bundle and formed denser and more interconnected networks than un-SWCNTs (**Appendix Figure A-1**). AuNPs anchored on defect sites of both types of SWCNTs, forming larger particles ($d = 126.3 \pm 34.1$ nm, $n = 55$) on un-SWCNTs and smaller particles ($d = 68.4 \pm 20.0$ nm, $n = 106$) on sc-SWCNTs (calculated from SEM images of Au-un-SWCNTs and Au-sc-SWCNTs, including 8nm of palladium coating). A primary difference between AuNP deposition on un-SWCNTs (**Figure 2-1a**) and sc-SWCNTs (**Figure 2-1b**) is the denser AuNP formation in the former case. Higher density AuNP formation is promoted by more available anchoring sites present in the un-SWCNTs resulting in larger quantities of CaM binding to the surface (**Figure 2-1c**), while the polymer coating on sc-SWCNTs may limit the decoration with AuNPs leading to less CaM on the surface (**Figure 2-1d**). Based on the prior work, we estimate a 1:1 weight ratio of wrapping polymer to

SWCNT in thin films, yet excellent thin film transistor performance indicates that tube-tube junctions are not significantly affected by the polymer.¹⁴² This is consistent with fewer binding locations for AuNPs on the polymer wrapped sc-SWCNTs.

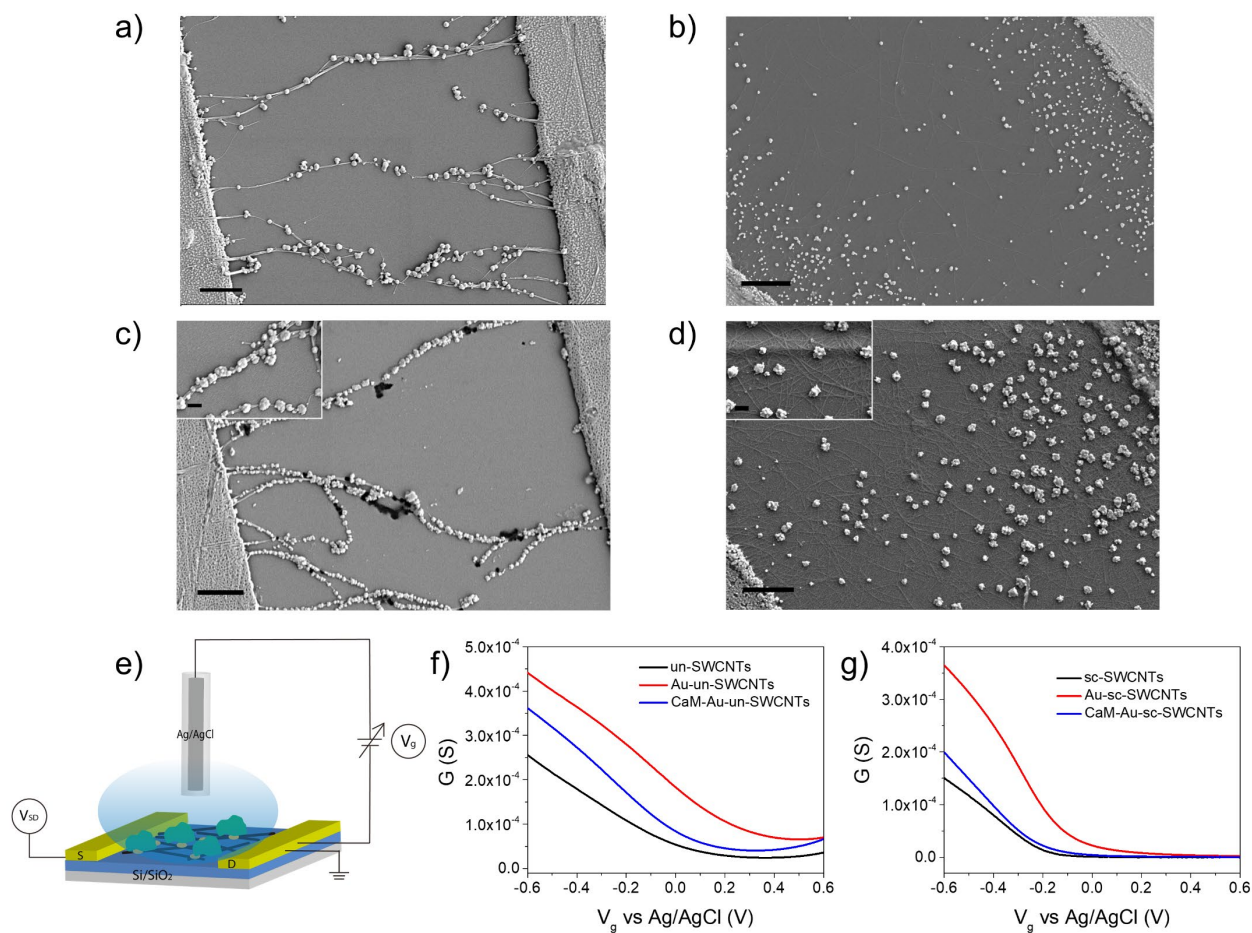


Figure 2-1 Binding of CaM on Au-sc-SWCNT and Au-un-SWCNT FET devices. (a-d) Scanning electron microscopy (SEM) images of AuNPs decorated un-SWCNT FET device (a) before and (c) after CaM binding, and AuNPs decorated sc-SWCNT (b) before and (d) after CaM binding. (Scale bar: 1 μm). Insets in panels c and d: zoom-in view of CaM covering AuNPs. (Scale bar: 200 nm). (e) Schematic illustration of a liquid gated carbon nanotube FET. Interdigitated gold electrodes (yellow blocks) are configured as source (S) and drain (D) whereas gate voltage (V_g) is applied through a Ag/AgCl reference electrode. Source-drain bias (V_{sd}) is 50 mV. (f-g) FET transfer characteristics, i.e., source-drain conductance (G) versus V_g , of (f) bare un-SWCNTs

(black), Au-un-SWCNTs (red), and CaM-Au-un-SWCNTs (blue) and (g) bare sc-SWCNT (black), Au-sc-SWCNT (red), and CaM-Au-sc-SWCNT (blue).

Binding of CaM on AuNPs was confirmed by atomic force microscopy (AFM), which showed height profile change after CaM functionalization (**Appendix Figure A-2**). CaM binds to AuNPs through gold-thiol bonds between its methionine (Met) residues and AuNPs. There are nine Met residues in CaM to facilitate stabilization of the open conformation of CaM after Ca^{2+} binding and provide the target binding surface.¹⁴³ Due to the fact that most of the Met residues located at the hydrophobic target-binding surface, the Ca^{2+} -induced conformational change occurs near the surface of the device, and the change in FET transfer characteristics can be detected within the ionic screening length. A liquid-gated FET device configuration was employed to study the transfer characteristics of both types of SWCNT FET devices (**Figure 2-1e**). All liquid-gated measurements were carried out in 0.01 X DPBS where the Debye screening length is calculated to be 7.53 nm.¹⁴⁴ Figure 1f and 1g show typical transfer characteristics of p-type SWCNT FETs. Conductance of un-SWCNT FET devices in the ON state is consistent with what has been previously reported.^{144, 145} The metallic component of un-SWCNTs contributes to the high conductance of un-SWCNT FET devices. Similar conductance was achieved for sc-SWCNT devices by using a relatively higher concentration of sc-SWCNTs during DEP process, forming dense networks across the channel. For both un-SWCNT and sc-SWCNT FET devices, AuNP decoration resulted in a significant increase in conductance. This observation can be attributed to the charge transfer from SWCNTs to AuNPs, which caused a depletion of electron density of the SWCNTs.¹⁴⁶ After the incubation with the CaM solution, the conductance decreased in the p-type region with more threshold voltage shifting to more negative values due to CaM binding onto the gold nanoparticles.

UV-vis-NIR absorption spectroscopy (**Figure 2-2**) provided complementary characterization of SWCNTs used in this study and revealed effects of functionalization on their electronic structure. UV-vis-NIR absorption spectra showed typical optical characteristics of SWCNTs associated with electronic transitions between van Hove singularities. For un-SWCNTs (**Figure 2-2a**), S_{11} , S_{22} and S_{33} peaks are characteristic of the semiconducting SWCNTs, whereas the metallic portion gives rise to the M_{11} peaks from 600 nm to 800 nm. For sc-SWCNTs (**Figure 2-2b**), the S_{11} , S_{22} and S_{33} peaks are sharper with slight shifts to higher energies, indicating nanotube diameter selection after the extraction with PFDD polymer, whose presence can also be observed as a sharp peak at 392 nm. Additionally, the absence of M_{11} peaks confirms the high-purity semiconducting content in the sc-SWCNTs sample. During the functionalization of SWCNTs, the decrease in the intensity of the S_{11} peak in both nanotube samples after AuNP decoration indicates the occurrence of charge transfer from SWCNTs to AuNPs during this process. However, AuNP-decorated un-SWCNTs (**Figure 2-2a**) showed more prominent absorption at 530 nm, which corresponds to the surface plasmon resonance (SPR) peak of AuNPs. After the incubation with the CaM solution, the increase in S_{11} peak of UV-vis-NIR spectra indicates an electron donation into SWCNTs after CaM binding. The AuNP SPR peak was less prominent in AuNP-decorated sc-SWCNTs (**Figure 2-2b**). This observation is consistent with SEM results that indicate smaller numbers of AuNPs were deposited on PFDD polymer-coated sc-SWCNTs as compared to un-SWCNTs (**Appendix Figure A-1**). The smaller increase of S_{11} peaks after CaM binding is also consistent with smaller portion of AuNP-decorated sc-SWCNT available for CaM binding.

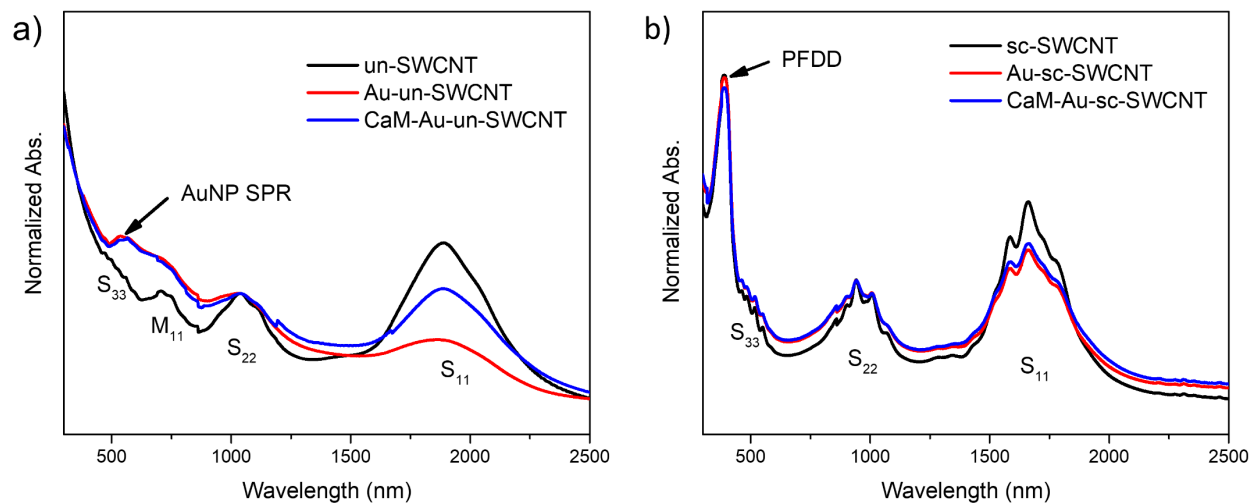


Figure 2-2 UV-vis-NIR absorption spectroscopy of un-SWCNT and sc-SWCNT during functionalization. UV-vis-NIR absorption spectra of (a) bare un-SWCNT (black), AuNPs decorated un-SWCNT (red) and CaM-functionalized Au-un-SWCNT (blue) and (b) bare sc-SWCNT (black), AuNPs decorated sc-SWCNT (red) and CaM-functionalized Au-sc-SWCNT (blue).

Raman spectroscopy provided further evidence for characteristics of un- and sc-SWCNTs and the charge transfer process during functionalization. For all studies, Raman spectra were recorded using a 638 nm laser excitation. As shown in **Figure 2-3**, both Raman spectra show characteristic peaks of SWCNTs, i.e., RBM, D band, G band, and G' band. For un-SWCNTs (**Figure 2-3a**), the G band, ranging from 1400 cm^{-1} to 1700 cm^{-1} , is split into two peaks, G^+ peak and G^- peak, which are centered at 1587 cm^{-1} and 1550 cm^{-1} , respectively. The broad and asymmetric G^- peak shown in Figure 3a has a Breit-Wigner-Fano (BWF) lineshape, which corresponds to the metallic feature of un-SWCNTs.¹⁴⁷ Similar to the Raman spectra of un-SWCNT, in the G band region of sc-SWCNTs from 1500 cm^{-1} to 1650 cm^{-1} , there are two peaks- G^+ peak centered around 1580 cm^{-1} and G^- peak centered around 1554 cm^{-1} (**Figure 2-3b**). However, in contrast to the broad G^- peak of un-SWCNT that has BWF lineshape, the G^- peak of sc-SWCNT is narrower with a Lorentzian lineshape, indicative of semiconducting carbon nanotubes.^{74, 148}

Radial breathing mode (RBM) peaks were characterized using a 785 nm laser excitation. Different RBM peak frequencies of un- and sc-SWCNTs under 785 nm laser excitation also confirms the high purity content of sc-SWCNTs (**Appendix Figure A-3**).

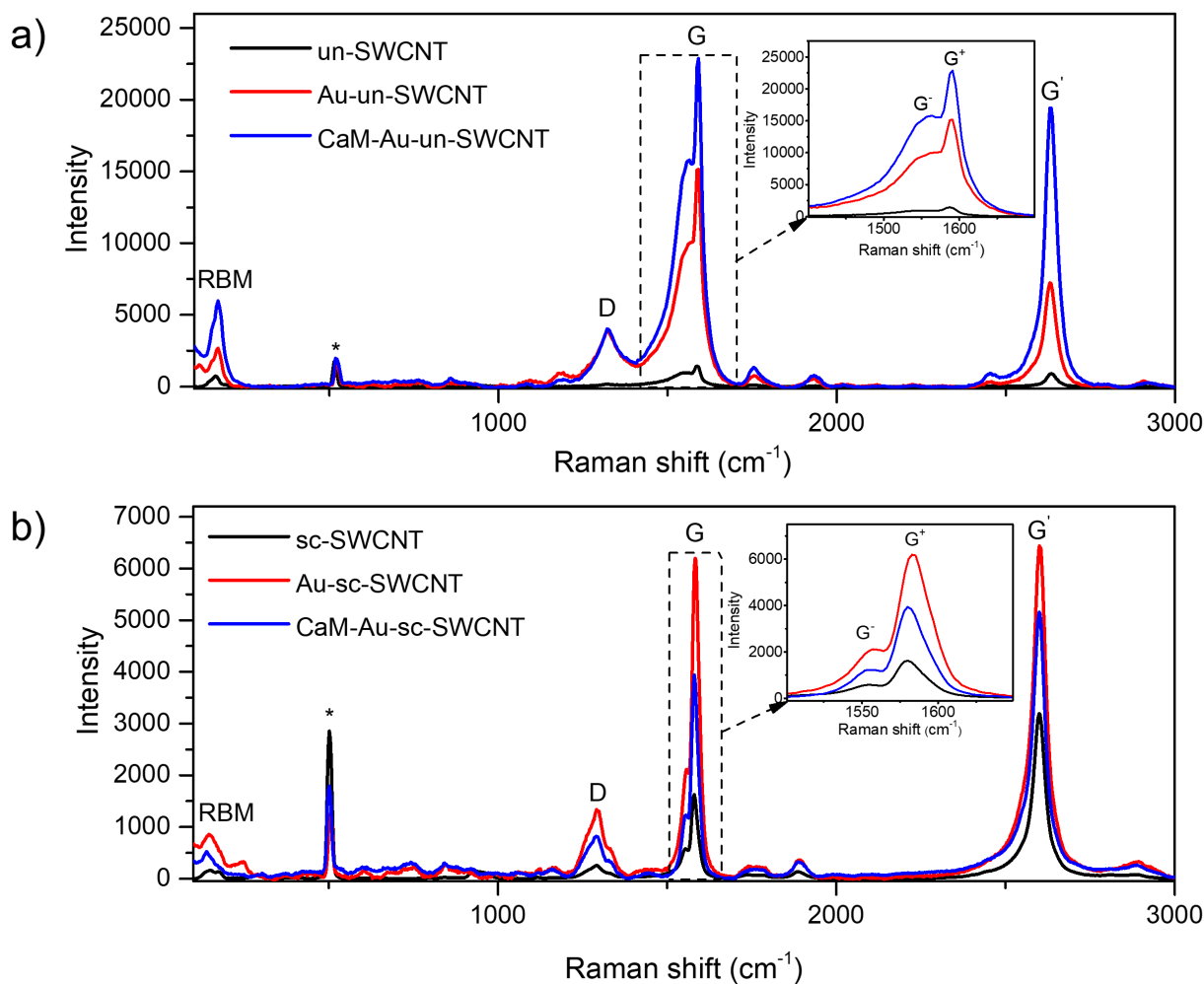


Figure 2-3 Raman spectroscopy of un-SWCNT and sc-SWCNT during functionalization. Raman spectra of (a) bare un-SWCNT (black), AuNPs decorated un-SWCNT (red) and CaM-functionalized Au-un-SWCNT (blue) and (b) sc-SWCNT (black), AuNPs decorated sc-SWCNT (red) and CaM-functionalized Au-sc-SWCNT (blue). Insets show G region of un- and sc-SWCNT. The peaks labeled with asterisks are associated with silicon substrate.

Gold nanoparticle-decoration resulted in a 10.6 X and 3.8 X enhancement in G peak intensity for un-SWCNT and sc-SWCNT respectively, which is due to surface-enhanced Raman scattering (SERS) effect that arises from the excitation of surface plasmons on metal nanoparticles.¹⁴⁹ The larger enhancement of Raman intensities of un-SWCNTs corresponds to the larger quantities of AuNPs on un-SWCNTs. In addition to the enhancement effect, the G⁺ peak of both types of SWCNTs experienced shifting toward higher energy (3.0 cm⁻¹ for un-SWCNT and 3.3 cm⁻¹ for sc-SWCNT). The blueshift of the G⁺ peak suggests that the coupling between AuNPs and SWCNTs induced an electron transfer from SWCNTs to AuNPs, thus p-doping the SWCNTs, hardening the G⁺ peak.^{150, 151} This result is consistent with our conclusion from UV-vis-NIR absorption spectroscopy. Upon CaM binding, featured peaks from CaM are almost unnoticeable in the spectra.¹³¹ Therefore, we use SWCNTs as a proxy chromophore to investigate the binding of CaM on Au-SWCNTs. A redshift from 1583 cm⁻¹ to 1580 cm⁻¹ of the G⁺ peak of sc-SWCNTs was observed, indicative of electron transfer back to un-SWCNTs.¹⁵⁰ However, for un-SWCNTs, the charge donation mainly affected the metallic portion of un-SWCNTs, narrowing the G⁻ peak.¹⁵²

The Ca²⁺-induced conformational change of CaM was first studied in solution via circular dichroism (CD) spectroscopy. CD spectra of 5.9×10⁻³ M calcium-free CaM and 5.9×10⁻³ M CaM solutions containing 10⁻¹⁵ M to 10⁻³ M Ca²⁺ were recorded. Increase in the negative bands at 208 nm and 221 nm was observed due to the increase in α -helical content as more CaM changed from calcium-free to calcium-bound conformation (**Appendix Figure A-4**).^{153, 154} We further used enhanced green fluorescent protein fused calmodulin (EGFP-CaM) to confirm the conformational change of CaM on Au-SWCNT surfaces. EGFP-CaM was expressed from cells and purified (**Appendix Figure A-5**). EGFP-CaM was attached on Au-SWCNT surfaces by incubating 2 μ M EGFP-CaM solution on chip, and fluorescence images of the device surface were captured before

and after addition of Ca^{2+} . An enhanced fluorescent signal between interdigitated gold electrodes was observed under 489 nm excitation light (**Figure 2-4**). Previous studies of EGFP-CaM have shown that the conformational change of CaM can induce a structural perturbation of the GFP moiety, modulating its fluorescence activity, resulting in an increase in EGFP fluorescence upon Ca^{2+} binding to CaM.^{155, 156} Therefore the enhancement of fluorescence suggests the occurrence of the Ca^{2+} -induced conformational change of CaM on the FET device surface.

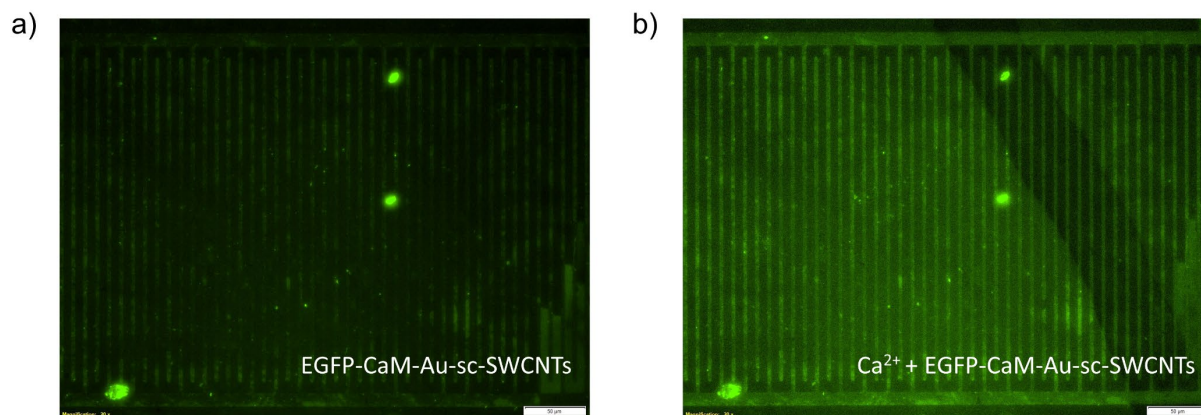


Figure 2-4 Fluorescence images of EGFP-CaM functionalized Au-SWCNT FET device. (a) Before Ca^{2+} binding. (b) After Ca^{2+} binding.

To investigate the effect of Ca^{2+} -induced conformational change of CaM on carbon nanotube FET devices, liquid-gated FET measurements were performed with a Ag/AgCl electrode as the gate electrode. For each FET measurement, both nanotube devices were first incubated with CaCl_2 solution for 2 min, then rinsed with nanopure water, and measured in 0.01X DPBS as the electrolyte medium with gate voltage sweeping from +0.6 V to -0.6 V. Measurement at constant ionic strength is important to eliminate any impact of different CaCl_2 salt concentrations on the Debye length and the measured signal of carbon nanotube FET devices.

Responses of CaM-Au-un-SWCNT FET devices were recorded in 0.01 X DPBS after incubation in a series of Ca^{2+} solutions with concentrations from 10^{-11} M to 10^{-3} M. By plotting the source-drain conductance (G) vs. applied gate voltage (V_g), a consistent decrease in the overall conductance of the device with increasing concentrations of calcium ions was observed (**Figure 2-5a**). A calibration curve was constructed by plotting the relative conductance change at $-0.5 V_g$ ($\Delta G/G_0$, where $\Delta G = |G_{-0.5V_g} - G_0|$, and G_0 is the conductance in buffer solution before Ca^{2+} exposure at $-0.5 V_g$) against concentrations of Ca^{2+} solution. The calibration curve was fit using a five-parameter logistic model¹⁵⁷, and the linear range of CaM-Au-un-SWCNT FET devices was determined to be 10^{-9} M to 10^{-7} M with a calibration sensitivity (m , defined as the slope of the linear region of the calibration curve) of 0.080 (**Figure 2-5b**). The FET transfer characteristics of CaM-Au-sc-SWCNT FET devices, on the other hand, showed a consistent shift towards more positive region in the threshold voltage with increasing concentration of Ca^{2+} (**Figure 2-5c**), and the linear range of the device was from 10^{-15} M to 10^{-13} M with a calibration sensitivity of 0.12 (**Figure 2-5d**). FET characteristics measured on different devices showed larger device-to-device variation for sc-SWCNT FET devices (**Appendix Figure A-6**).

Control experiments were performed to compare their sensitivity with the sensitivity of the CaM-Au-SWCNT FET devices. **Figure 2-5e** shows the calibration sensitivity of the active and control systems. The active system for both types of SWCNT FET devices have the best sensitivity in the corresponding dynamic range. Among control systems, both types of devices display sensitivity towards Ca^{2+} when having CaM on bare SWCNTs, but the sensitivity is significantly less than that of the active system which we attribute to reduced CaM present and random orientation of binding on the defect sites of SWCNTs (**Appendix Figure A-7**). In the absence of CaM on the SWCNTs and Au-SWCNTs, the responses of both types of devices show minimal

sensitivity or poor linearity towards different concentrations of Ca^{2+} due to the lack of conformational change of CaM (**Appendix Figure A-7**). Additionally, the poor sensitivity of the active systems towards Mg^{2+} , an ion that induces less pronounced structural changes of CaM than Ca^{2+} does when bound to the protein,¹⁵⁸ provides further evidence that the sensitivity of the devices is a result of the conformational change of CaM. In the presence of bovine serum albumin (BSA), an interfering protein that has a calcium binding constant of $\sim 90 \text{ M}^{-1}$ in 0.01 X PBS buffer (3-4 orders of magnitude lower than that of CaM),¹⁵⁹ the active systems still show good sensitivity toward Ca^{2+} with 41% lost in calibration sensitivities for un-SWCNT devices and 27% for sc-SWCNT devices. However, it is demonstrated that the devices are not sensitive toward BSA itself (**Figure 2-5e**). The loss in calibration sensitivity is likely due to the binding between Ca^{2+} and BSA, reducing the amount of CaM that undergoes the conformational change.

Gate leakage current in both types of devices was also analyzed to investigate whether not encapsulating Au source and drain electrodes would affect the sensing performance. The results show (**Appendix Figure A-8**) that the leakage current is insignificant compared with the measured source-drain current, therefore the effect of leakage current is negligible.

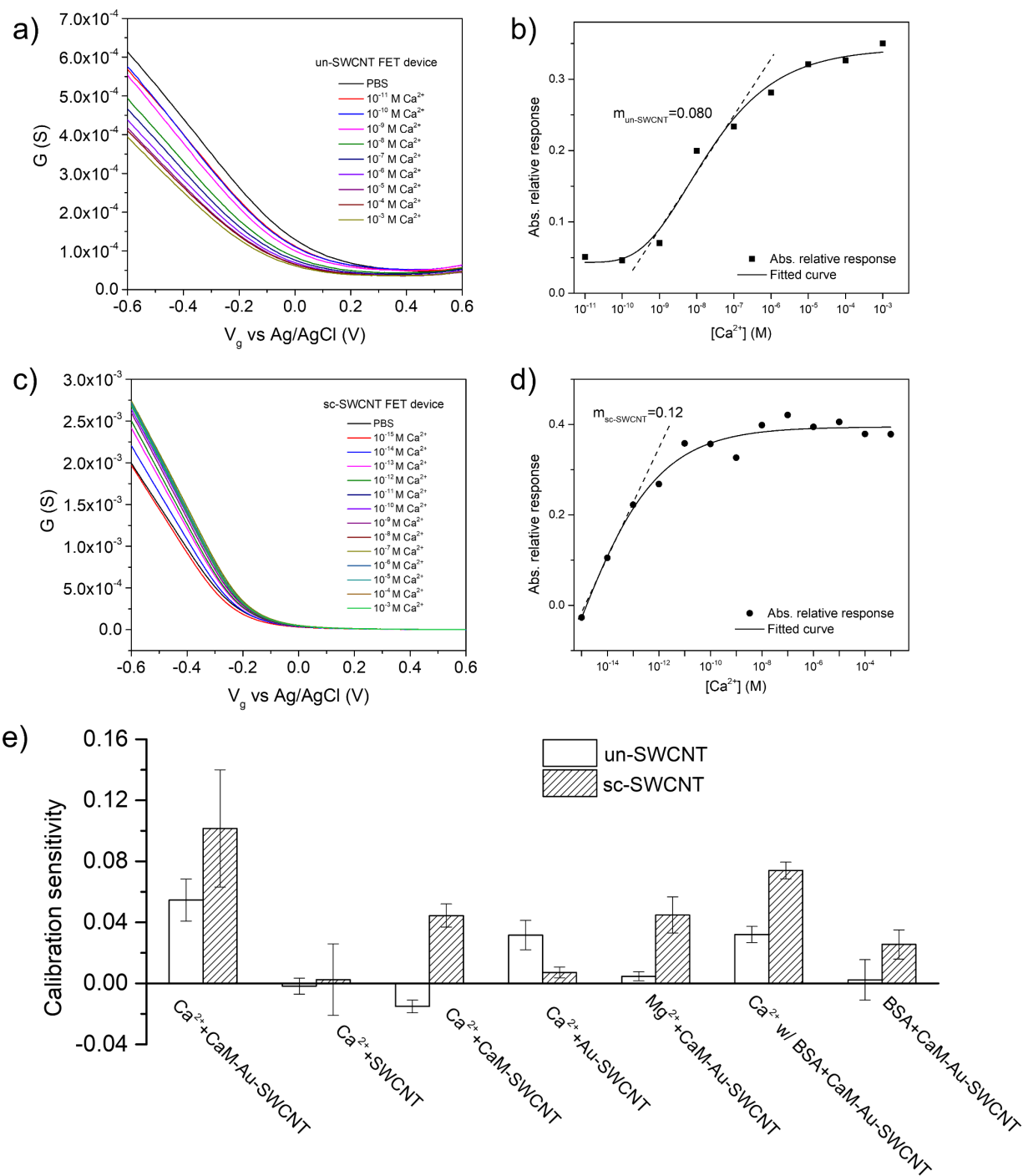


Figure 2-5 Ca^{2+} sensing with CaM-un-SWCNT and sc-SWCNT FET devices. (a) FET characteristic curves of un-SWCNT FET devices upon exposure to increasing concentrations of $CaCl_2$. (b) Calibration plot for Ca^{2+} sensing with un-SWCNT FET devices. (c) FET characteristic curves of sc-SWCNT FET devices with exposure to increasing concentrations of $CaCl_2$. (d) Calibration plot for Ca^{2+} sensing with sc-SWCNT devices.

e) Calibration sensitivity of the active system and control systems for un- and sc-SWCNT FET devices.

Calibration sensitivity is defined as the slope of the linear range. (Error bars are calculated from multiple devices).

For Au-un-SWCNT devices, the sensing mechanism behind the consistent drop in device conductance is attributed to the Schottky barrier effect. With the occurrence of conformational change at the SWCNT-AuNPs contact region, the local work function of metal is reduced, which leads to an alteration of the Schottky barrier of the nanotube-metal interfaces, therefore decreasing the conductance of the FET device.¹⁶⁰ This effect is further amplified by the presence of multiple nanoscale Schottky barriers formed across AuNP-nanotube interfaces.⁹¹⁻¹⁶¹ However, the opposite shift of the FET characteristics of Au-sc-SWCNT devices suggests an alternative sensing mechanism due to the different properties between un-SWCNT and sc-SWCNT. Instead of Schottky barrier effect, the conformational change of CaM caused an exposure of its negatively charged side chains to the local environment,¹⁶² inducing additional hole carriers in sc-SWCNTs, therefore shifting the I-V_g curves toward more positive gate voltages due to electrostatic gating effect.¹⁶³ This effect does not play a dominant role in un-SWCNT due to the presence of metallic SWCNTs and multiple interfaces between AuNP and SWCNTs. M-SWCNTs have constant density of state (DOS) near the Fermi level,¹⁶⁴ making them less sensitive to Fermi level shifts, and Schottky barrier modulation consequently overwhelms the doping effect on semiconducting nanotubes in un-SWCNTs.

Interestingly, the sc-SWCNT FET devices display a higher slope of the calibration curve and a linear range over lower Ca²⁺ concentrations when compared with un-SWCNT FET devices. The higher slope of the calibration curve can be attributed to the high on/off ratio of the transistor. In our case, the on/off ratio of un-SWCNT FET device is only ~3, whereas the on/off ratio of sc-

SWCNT FET device is $\sim 10^4$ (**Appendix Figure A-9**). Higher on/off ratio can lead to higher relative response, making the FET more sensitive to small shift in the threshold voltage, hence the better calibration sensitivity for sc-SWCNT FET devices (**Appendix Figure A-10**). The high purity of semiconducting SWCNT contributes to the high on/off ratio of sc-SWCNT FET devices. In contrast, the presence of metallic SWCNTs in un-SWCNTs provides electrically conducting pathways, inhibiting the ability of the transistor to reach low off state conductance. However, sc-SWCNT FET devices saturated at lower concentrations of Ca^{2+} than un-SWCNT devices. The absolute relative conductance change increased linearly with Ca^{2+} from 10^{-15} M to 10^{-13} M (in logarithmic scale), and then reached a plateau after 10^{-11} M, showing saturation of the devices (**Figure 2-5d** and **Appendix Figure A-6**). This can be attributed to the limited amount of CaM detectable on sc-SWCNT devices. As mentioned earlier, AuNP deposition formed larger and denser AuNPs on un-SWCNTs than sc-SWCNTs, but the average size of CaM after binding to AuNPs on un-SWCNTs and sc-SWCNTs, 137.7 ± 37.4 nm ($n = 45$) and 155.2 ± 42.5 nm ($n = 26$) respectively (calculated from SEM images of CaM-Au-un-SWCNTs and CaM-Au-sc-SWCNTs, including 8 nm palladium coating), are relatively comparable considering the large standard deviation. This is indicative of more CaM aggregates on each AuNP on sc-SWCNTs due to limited binding sites for CaM. However, due to the limitation of Debye screening length, only the conformational change of CaM occurring at the SWCNT-AuNPs contact region can be probed. Therefore, with smaller AuNP surface area on sc-SWCNT devices, the amount of CaM detectable upon conformational change is reduced, making the sc-SWCNT FET devices saturate at lower concentration of Ca^{2+} than un-SWCNT devices.

Therefore, high-purity sc-SWCNTs FETs, besides their outstanding sensing performance towards small molecules such as hydrogen and ammonia gas, sensitively detect the change of

charge distribution of CaM upon Ca^{2+} -induced conformational change with Ca^{2+} as low as 10^{-15} M. This low limit of detection indicates only 0.2 femtomolar CaM is required for the detection of the conformational change,¹⁶⁵ which significantly lowered the amount of CaM sample required by other techniques such as NMR¹³⁴ and X-ray crystallography.¹³⁶ Furthermore, with the limit of detection of 10^{-15} M Ca^{2+} , our CaM-functionalized Au-sc-SWCNT FET device can also function as a Ca^{2+} sensor that provides ultrasensitivity and selectivity when compared to other Ca^{2+} detection methods (**Appendix Table A-1**).¹⁶⁶⁻¹⁶⁹

2.5 Conclusions

In summary, we compared FET responses of un- and sc-SWCNT FET devices during Ca^{2+} -induced conformational change of CaM. The sc-SWCNT FET devices exhibited better sensitivity towards the conformational change of CaM. The higher sensitivity can be attributed to the high on/off ratio of sc-SWCNT FET devices, arising from the effective bandgap of high purity sc-SWCNT. The dynamic range at lower concentrations of Ca^{2+} , on the other hand, was due to the low CaM density on the device surface induced by the polymer wrapping on sc-SWCNT. Our SWCNT FET devices provide a label-free, highly sensitive and efficient way to probe the conformational change of CaM. To further improve our device for reliable and standardized sensing, controllable deposition and alignment of SWCNTs on FET devices are crucial. For example, uniform SWCNT networks can be formed in the channel by inkjet printing¹⁴² or dip coating¹⁷⁰ for making thin-film transistors (TFTs) with <10% variability. We envision that our AuNPs-decorated high-purity semiconducting SWCNT FET devices can have further applications in detecting protein interactions.

2.6 Acknowledgement

The XplorA Raman-AFM/TERS system was purchased via Defense University Research Instrumentation Program (DURIP) grant from the Office of Naval Research, ONR (N000141410765).

3.0 Cerebrospinal Fluid Leak Detection with a Carbon Nanotube-Based Field-Effect Transistor Biosensing Platform

3.1 Chapter Preface

The aim of this work was to present a three-step strategy for the rapid detection of cerebrospinal fluid (CSF) leak. The 3-step design, which includes two steps of affinity chromatography and a rapid sensing step using a high-purity semiconducting (sc-) single-walled carbon nanotube (SWCNT) field-effect transistor (FET) device, circumvented the lack of selectivity that anti-transferrin antibody exhibits for transferrin isoforms, and markedly shortened detection time to 1 hour. Furthermore, three different sensing configurations for the sc-SWCNT FET sensor were investigated for obtaining the optimal β 2-Tf sensing results. The work presented in this chapter will be submitted for publication in the near future.

List of Authors: Wenting Shao, Galina V. Shurin, Xiaoyun He, Michael R. Shurin and Alexander Star

3.2 Introduction

Leakage of cerebrospinal fluid (CSF) is a serious condition that can result from trauma, invasive tumors, congenital malformation, or surgical procedures and results in significant morbidity and mortality if left untreated.¹⁷¹ Without appropriate treatment, CSF leaks can lead to life-threatening cases of meningitis, intracranial hypotension, or pneumocephalus. Identification

of CSF in non-native sites requires immediate surgical intervention, usually in the form of endoscopic endonasal or transcranial surgery.¹⁷² However, the diagnosis of CSF leak is often difficult to confirm. Traditional chemical analyses of biological fluids (e.g., glucose, total protein, specific gravity) are unreliable and have been largely abandoned. Radiographic and magnetic imaging methods, especially those involving the injection of dyes or radiographic agents, are not always successful, require expensive, time-consuming procedures, and may introduce additional risks to the patient.¹⁷³ Accumulating clinical data do not support the use of the ring sign, glucose testing, radionuclide cisternography, or computed tomography cisternography for identification of CSF leak.

Clinical laboratory detection of CSF leak takes advantage of the heterogeneity of transferrins in bodily fluids and utilizes beta2-transferrin (β 2-Tf) detection in available specimens as an indicator of CSF presence.¹⁷⁴ Transferrin is a 79 kDa iron-binding protein transporting and maintaining iron homeostasis.¹⁷⁵ The number of sialic acid groups varies to create 9 transferrin isoforms ranging from 0 to 8 sialic acid groups.¹⁷⁶ The major isoform with 4 sialic acid groups is β ₁-transferrin, the predominant form in most body fluids including serum. In contrast, β 2-TF (carbohydrate-free, desialated), is formed by loss of sialic acid due to the presence of neuraminidase in the central nervous system (CNS) and is confined to the CSF, aqueous humor, and perilymph.^{177, 178} Thus, β 2-TF is a CSF-specific variant of transferrin used as an endogenous marker of CSF leakage if detected in nasal or aural fluid. β 2-Tf can be resolved from the other isoforms of transferrin because differences in sialic acid content change the isoelectric point of the protein, allowing separation by gel electrophoresis.^{179, 180} However, the main problem with electrophoretic separation of transferrins and their staining is a running time required for electrophoresis + transfer + Western blot: 3 to 6 h, which is not always adequate for the β 2-TF

assay when ordered on STAT turnaround time priority level (from the Latin *statim* - immediately or without delay) by neurosurgeons. Another problem is the result interpretation which requires a pathologist or a highly trained and experience medical technologist who are not always available for STAT procedures.

Nanomaterial-based biosensors have shown great potential in diagnostic tools as they offer high sensitivity, label-free and rapid detection of biomolecules as well as easy fabrication and miniaturization.¹⁸¹⁻¹⁸⁷ In particular, CNT-based field-effect transistor (FET) biosensors are promising candidates for point-of-care diagnostic devices, owing to the outstanding electronic and mechanical properties of CNTs.^{81, 188, 189} CNT-based FET biosensors probe the interactions of biomolecules with the semiconducting (sc-) single-walled carbon nanotube (SWCNT) channel causing alteration in the electrical conductance of the sc-SWCNTs. Therefore, high-purity sc-SWCNTs, which enable high on-state conductance and high on/off ratio for FETs, are ideal material in order to develop high-performance FET devices.^{59, 79, 118} Recently, high-purity sc-SWCNTs have shown promise for sensing applications, such as gas sensors,^{123-125, 190} humidity monitor,¹²⁶ infrared imaging sensor,¹⁹¹ as well as ultrasensitive biosensors, such as aptasensors^{127, 128} and label-free protein sensors.^{110, 129, 130} Herein, we present a new β 2-Tf laboratory detection method for different biological fluids with high sensitivity, short turnaround time and easy instrument access. The 3-step strategy for β 2-Tf detection includes two steps of affinity chromatography to isolate β 2-Tf and a rapid β 2-Tf sensing step utilizing a high-purity sc-SWCNT FET device. Three different sensing configurations for the sc-SWCNT FET sensor were investigated for obtaining the optimal β 2-Tf sensing results. Finally, β 2-Tf detection in body fluids, namely CSF and serum, employing the 3-step strategy demonstrated markedly improvement in the

sensitivity and responsiveness than the gold standard electrophoresis method, indicating a proof-of-principle for use as a rapid CSF leak diagnostic tool.

3.3 Experimental Section

Affinity column preparation. Anti-transferrin antibody functionalized column was prepared by immobilizing anti-transferrin antibody (Tf-ab, Fisher Scientific, Cat#: PA184854) on CNBr-activated Sepharose® 4B (MilliporeSigma, Cat#: C9142) according to manufacturer's instructions. Briefly, 25 mg of lyophilized CNBr-Sepharose were suspended in 1 mM HCl in a spin column (Thermo Fisher Scientific, Cat#: 69725), pH 3.0 and subsequently washed with 1 mM HCl for 15 min. Tf-ab was diluted 10-fold in coupling buffer (0.1 M NaHCO₃, 0.5 M NaCl, pH 8.3), mixed with Sepharose (1 mg of Tf-ab per mg of Sepharose 4B) and incubated at room temperature for 2 h. After incubation, excess ligand was washed away with coupling buffer by centrifugation. The suspension was then incubated with 300 µL of 1 M ethanolamine, pH 8.0 for 2 h at room temperature in order to block any remaining active groups. After blocking, the material was washed with three cycles of alternating pH (0.1 M sodium acetate, 0.5 M NaCl, pH 4.0 and coupling buffer, pH 8.0). The final product was then washed with 300 µL nanopure water and stored in 0.5 M NaCl at 4°C.

Serotonin (MilliporeSigma, Cat#: H9523) was immobilized via its amine on CNBr-Sepharose by the cyanogen bromide method, similar to Tf-ab functionalization. Briefly, 25 mg of lyophilized CNBr-Sepharose were suspended in 1 mM HCl, pH 3.0 and subsequently washed with 1 mM HCl for 15 min. 40 mg serotonin-HCl were dissolved in 10 mL coupling buffer (0.1 M NaHCO₃, 0.5 M NaCl, pH 8.3) and added to the activated CNBr-Sepharose in a spin column and

incubated for 2 h at room temperature with light protection. Following, excess ligands were washed away, and the remaining active groups were blocked using 1 M ethanolamine, pH 8.0 for 2 h at room temperature. After blocking, the column was washed with three cycles of alternating pH, and then equilibrated in 0.5 M NaCl for storage at 4 °C.

Affinity chromatography. CSF (Thermo Fisher Scientific, Cat#: 50-203-6082) and serum (Thermo Fisher Scientific, Cat#: BP2657100) samples were used as a positive and a negative control. Serum samples were diluted 100-fold with 1× phosphate buffered saline (PBS) prior to chromatography steps. CSF samples had no pretreatments.

In step 1, 200 µL of CSF (or 100-fold diluted serum) sample was loaded onto the Tf-ab functionalized column and incubated for 20 min at room temperature before centrifugation at 10,000 × g for 2 min for elution. The bound total transferrin was eluted from Tf-ab/Sepharose column by applying the stripping buffer (0.1 M Glycine HCl, pH = 2.6, 200 µL each time) twice. The pH of the eluate was recovered immediately by adding 1 M Tris (pH 8.3) and loaded to the serotonin functionalized column for step 2. After a 20 min incubation at room temperature, the column was centrifuged at 10,000 × g for 2 min and the eluate was collected for β2-Tf detection in step 3. The column was then stripped with 500 mM sodium chloride in 20 mM sodium phosphate (pH = 6).

Enzyme-linked immunosorbent assay (ELISA). Transferrin human ELISA kit was purchased from ThermoFisher Scientific (Cat#: EHTF). For the standard curve, transferrin standards at concentrations of 0.1 ng/mL, 1 ng/mL, 10 ng/mL, 100 ng/mL, 500 ng/mL, 1 µg/mL and 10 µg/mL were prepared using recombinant human serum transferrin (MilliporeSigma, Cat#: T8158). A 2 mg/mL recombinant human serum transferrin solution mixed with 10 mg/mL BSA in PBS was treated with neuraminidase (MilliporeSigma, Cat#: N7885) and used as the positive

sample. The same solution without the neuraminidase treatment was used as the negative sample. Both positive and negative samples were run through the two steps of separation using Tf-ab functionalized and serotonin functionalized affinity columns. The eluate from step 2 was collected for ELISA test.

ELISA was performed following the instruction provided with the kit. Absorbance was measured at both 450 nm and 550 nm (as background) using a Tecan M1000 pro plate reader. For data analysis, background was subtracted from all samples measured. The standard curves were run twice to determine the intra-assay precision. Both positive and negative samples were run twice, and the blank was run 5 times. All data reported in the figure and table were Mean \pm SD.

Device fabrication. High-purity semiconducting single-walled carbon nanotubes were obtained commercially (IsoSol-S100, Raymor Industries Inc.) and were prepared at 0.02 mg/mL in toluene. Interdigitated gold electrodes (channel length of 10 μ m) were patterned on a Si/SiO₂ substrate using photolithography. SWCNTs were then deposited between gold electrodes via dielectrophoresis (DEP) with an AC frequency of 100 kHz, applied bias voltage of 10 V, and bias duration of 120 s.

Anti-transferrin antibody (Tf-ab) functionalization on SWCNTs was achieved via 1-ethyl-3-(3-dimethylaminopropyl)carbodiimide hydrochloride (EDC)/N-hydroxysulfosuccinimide (sulfo-NHS) coupling. The SWCNT FET devices were first activated in 100 μ L of EDC/sulfo-NHS solution (50 mM/50 mM in 1 \times PBS, pH = 5.5) followed by a rinse with nanopure water. The devices were then incubated with 10 μ L of 100 μ g/mL Tf-ab (in 1 \times PBS) for 2 h at room temperature and rinsed thoroughly with nanopure water after incubation. To prevent nonspecific binding, the devices were soaked in a blocking buffer (0.1% Tween 20 and 4% polyethylene glycol in PBS) for 30 min to block unreacted surface.

FET measurements. FET characteristics of SWCNT FET devices were studied employing liquid-gated FET device configuration. Nanopure water was used as the gating electrolyte. Characteristic FET curves, i.e., source-drain conductance (G) versus gate voltage (V_g), were taken by sweeping the gate voltage from +0.6 to $-0.6 V_g$ versus a Ag/AgCl reference electrode with a fixed source-drain voltage of 50 mV.

A series of transferrin solutions ranging from 10^{-4} fg/mL to 1 μ g/mL were prepared using recombinant human serum transferrin (MilliporeSigma, Cat#: T8158). For transfer characteristic measurements using bare SWCNT and Tf-ab-SWCNT approach, the sc-SWCNT FET devices were first incubated in 10 μ L of transferrin solution for 2 min, then rinsed with nanopure water, and measured in nanopure water as the gating electrolyte. For transfer characteristic measurements using Au electrode approach, the gold disk surface (2 mm diameter) was immersed in 10 μ L of transferrin solution for 2 min. The Au electrode was then washed with nanopure water and measured in nanopure water as the gate electrolyte.

For body fluid tests, 10 μ L of the eluate from step 2 was added to the sc-SWCNT FET devices or the gold disk surface for incubation for 2 min followed by a rinse with nanopure water. All FET characteristics measurements were recorded in nanopure water as the gating electrolyte.

The relative response (R) of each FET device was calculated using $R = \Delta I_d / I_0$, where $\Delta I = |I_d - I_0|$, and I_0 is the drain current in nanopure water before transferrin exposure at $-0.5 V_g$. To construct the calibration curve, relative responses calculated from each device tested were averaged at each concentration and plotted against transferrin concentrations on a logarithmic scale. Error bars represented one standard deviation (SD). The number of devices (n) tested for each experiment was specified in the text.

Electrochemical impedance spectroscopy (EIS). All impedance measurements were

performed using a CH Instruments electrochemical workstation (Instrument model: 7042C). Recombinant transferrin solutions were prepared from 1 fg/mL to 1 µg/mL. For each concentration, 10 µL of the transferrin solution was added on the gold disk surface at an increasing concentration order and incubated for 2 min, followed by a rinse with nanopure water. The impedance was measured in PBS solution with an AC amplitude of 5 mV over a frequency (f) range of 0.05 Hz to 10⁵ Hz.

UV-vis-NIR absorption spectroscopy. 100 µL of 0.02 mg/mL sc-SWCNTs were drop casted on a 1” × 1” quartz slide and heated at 200 °C to evaporate the solvent. UV-vis-NIR spectra of sc-SWCNT were collected using a Perkin-Elmer Lambda 900 UV-vis-NIR spectrophotometer.

Fluorescence imaging. Fluorescence images were obtained using an Olympus 1X81/1X2-UCB microscope. For nonspecific binding of transferrin on sc-SWCNTs, 10 µL of 100 µg/mL Alexa Fluor 647 conjugated transferrin (Thermo Fisher Scientific, Cat#: T23366) was added to the sc-SWCNT device and incubated for 2 min at room temperature. Fluorescence images of bare sc-SWCNT devices before and after Alexa Fluor 647 conjugated transferrin binding were captured under excitation of 633 nm. For Tf-ab functionalized sc-SWCNT devices, Tf-ab was functionalized on the sc-SWCNTs via EDC/NHS coupling. 10 µL of 10 µg/mL Alexa Fluor 546 conjugated anti-IgG secondary antibody (Thermo Fisher Scientific, Cat#: A11056) was then added to the device and incubated for 10 min at room temperature. As a control, 10 µL of 10 µg/mL Alexa Fluor 546 conjugated anti-IgG secondary antibody was also added to a bare sc-SWCNT FET device with blocking. All fluorescence images were taken under excitation of 532 nm.

Raman spectroscopy. Raman spectroscopy was performed on a XplorA Raman-AFM/TERS system. 785 nm (100 mW) excitation laser was used and operated at 1% power.

Gel electrophoresis and Western blot. Gel electrophoresis was carried out on a glass slide on 1% agarose (SeaKem® Agarose, Lonza) in a barbital buffer (MilliporeSigma, Cat#: B5934). Each sample (2 µL) was applied on the gel using a 6-lane template as the alignment guide. Excess sample was removed by gently blotting the template with a Whatman filter paper. The glass slide was placed inside the electrophoresis chamber (Horizontal Electrophoresis System, C.B.S. Scientific) with 4 trimmed pieces of blotter C paper (Helena) premoistened with barbital buffer on each side as a conduit for the buffer. The gel electrophoresis was run at 250 V for 1 hour in barbital buffer with a circulated cooling solution or cold water.

After electrophoresis, a 0.45-µm pore nitrocellulose membrane (GE Healthcare Life Sciences) moistened with deionized (DI) water was placed on top of the glass slide and pressed for 30 min with weights to transfer the protein from the gel to the membrane. The membrane was then blocked with 1% nonfat dry milk in BupH™ Tris buffered saline (ThermoFisher Scientific, Cat#: 28379) for 20 min, followed with rinses with DI water for 6-8 times. Next, the membrane was first incubated in a buffer with 1:2500 diluted goat anti-transferrin antibody (Cappel, catalog# 55139), 1% bovine serum albumin (BSA), 4% polyethylene glycol (PEG), and 0.05% Tween-20, Tris-buffered saline solution for 20 min. Then blots were rinsed with DI water 6-8 times, and incubated with 1:5000 diluted horseradish peroxidase-conjugated chicken anti-goat IgG antibody (MilliporeSigma, Cat#: AP163P) in a 1% BSA, 4% PEG, and 0.05% Tween-20, Tris-buffered saline solution for 20 min. After another rinse with DI water for 6-8 times, the membrane was incubated in a 0.85% NaCl solution for 10 min and then developed in 3,3',5,5'-Tetramethylbenzidine (TMB) reagent (MilliporeSigma, Cat#: T0440). The membrane was washed 3 times with DI water when the development was finished.

3.4 Results and Discussion

Due to the lack of specific receptor for β 2-transferrin (β 2-Tf), separation steps were employed to first separate β 2-Tf from a specimen in order for the detection on a SWCNT FET sensor. Thus, here we present a 3-step design for β 2-Tf detection: 1) Isolation of all transferrin isoforms from other biological species present in the sample, 2) separation of β 2-Tf from the other isoforms and 3) β 2-Tf detection with a SWCNT FET sensor (**Figure 3-1**). Both steps 1 and 2 are achieved by utilizing commercial affinity chromatography platform. In step 1, transferrin (all isoforms) was separated from other species using an anti-transferrin antibody (Tf-ab) immobilized Sepharose column. The bound transferrin was then stripped from the column and loaded into a serotonin (5-hydroxytryptamine) functionalized column (step 2) for the separation of β 2-Tf. Serotonin is a sialic acid-binding molecule, which is nontoxic and commercially available at a relatively low price, making it suitable for clinical use.¹⁹² Affinity of serotonin towards sialylated glycoproteins was proven^{193, 194} and since then it was used successfully for the analysis and purification of glycans, glycopeptides, and glycoproteins. The successful separation of β 2-Tf using the 2-step separation approach was proved by enzyme-linked immunosorbent assay (ELISA), where transferrin was detected in eluate from step 2 from the positive sample, while no transferrin was detectable from the negative sample due to the absence of β 2-Tf in the original sample (**Appendix Figure B-1** and **Appendix Table B-1**).



Figure 3-1 The 3-step strategy for detection of $\beta 2$ -Tf. Step 1, separation of all transferrin isoforms from the sample using anti-transferrin antibody functionalized affinity column. Step 2, separation of $\beta 2$ -Tf from other isoforms using serotonin functionalized affinity column. Step 3, detection of $\beta 2$ -Tf with a sc-SWCNT FET device. Insets show 3 different approaches for $\beta 2$ -Tf detection using a sc-SWCNT FET device, i.e., I. Bare SWCNTs: nonspecific binding of $\beta 2$ -Tf to bare sc-SWCNTs; II. Tf-ab-SWCNTs: detection of $\beta 2$ -Tf via anti-transferrin antibody functionalized sc-SWCNTs; III. Au electrode: detection of $\beta 2$ -Tf through binding to a gold gate electrode.

The $\beta 2$ -Tf FET sensing device was built utilizing high purity sc-SWCNTs as the sensing material. Sc-SWCNTs were deposited via dielectrophoresis (DEP) between interdigitated gold electrodes patterned on a 2 mm \times 2 mm Si/SiO₂ wafer. Scanning electron microscopy (SEM) characterization of the device surface showed dense and interconnected networks formed by sc-SWCNTs, and UV-vis-NIR absorption spectroscopy of the sc-SWCNT sample showed no M₁₁ peak, confirming the high purity semiconducting content in the sc-SWCNT (**Appendix Figure B-2**).

Three approaches for the transferrin detection were evaluated in order to obtain the best transferrin sensing results. The first approach was using bare sc-SWCNTs for transferrin detection as proteins can bind to bare SWCNTs nonspecifically, changing the device characteristics.^{81, 85} Fluorescent images taken before and after exposing sc-SWCNT to Alexa Fluor 647 conjugated

transferrin demonstrated the nonspecific binding of transferrin on bare sc-SWCNTs, as red fluorescent became observable on the device surface after the addition of transferrin (**Appendix Figure B-3**). To test for the transferrin sensing capability of bare sc-SWCNT FET devices, a series of transferrin solutions with increasing concentrations were added to the sc-SWCNT FET devices for a 2-min incubation, and all FET transfer characteristics were recorded in nanopure water to eliminate any impact on the sensing results caused by having different ionic strengths. The calibration curve was constructed by plotting the relative response (R) at $-0.5 V_g$ against concentrations of transferrin on a logarithmic scale (**Figure 3-2**). FET transfer characteristics showed a decrease in the ON state current as transferrin being absorbed on sc-SWCNTs nonspecifically. However, the calibration curve demonstrated poor dose-dependent responses, and the sensitivity was significantly limited by the large device-to-device variability due to the uncontrollable amount of protein binding to each device. Furthermore, the large variance in each device may render low reliability of the sensing results, which can result in serious problems in clinical practices.

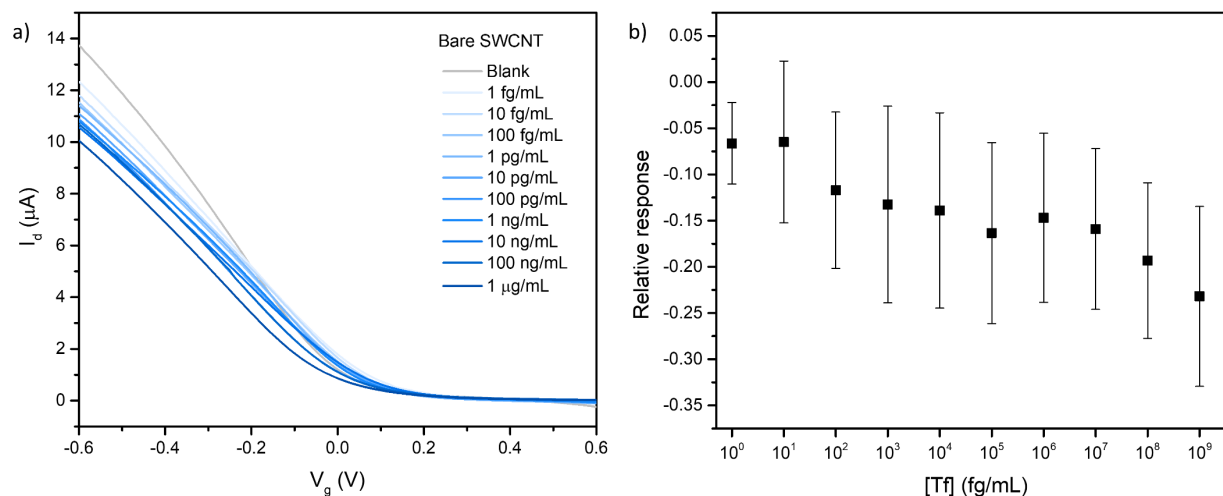


Figure 3-2 Detection of transferrin using bare SWCNT FET devices. (a) FET characteristic curve of bare SWCNT FET devices upon exposure to increasing concentration of transferrin. (b) Calibration plot for transferrin detection using bare SWCNT FET devices. All data points in the calibration plot are Mean \pm SD (n = 5 devices).

In order to improve the reliability, we introduced specificity to the transferrin sensor by functionalizing Tf-ab on the sc-SWCNT FET device via EDC/NHS coupling. In this case, the detection of transferrin relies upon the specific interaction between transferrin and Tf-ab near the sc-SWCNT surface. The successful integration of Tf-ab on sc-SWCNT was characterized using fluorescence microscopy (**Appendix Figure B-4**). Moreover, Raman spectroscopy revealed a diameter dependent functionalization of Tf-ab on sc-SWCNTs (**Appendix Figure B-5**). **Figure 3-3a** shows the FET transfer characteristic (I - V_g) curves of the Tf-ab functionalized FET device upon exposure to recombinant transferrin at varying concentrations. The threshold voltage shifted toward less negative values with increasing concentration of transferrin, which can be attributed to the introduction of negatively charged transferrin (pI ranges from 5.4 to 6.2)¹⁹⁵ near the sc-SWCNT surface, thus p-doping the SWCNTs.¹⁶³ The sensing performance of the Tf-ab functionalized sc-SWCNT FET sensor was then evaluated by plotting the calibration curve

(Figure 3-3b, black). The limit of detection of the sensor was determined to be 0.01 fg/mL, suggesting an ultrasensitivity toward transferrin. The dynamic range (linear region) of the sensor was 10 fg/mL to 1 pg/mL and the calibration sensitivity, which is defined as the slope of the linear region of the calibration curve, was determined to be 0.06.

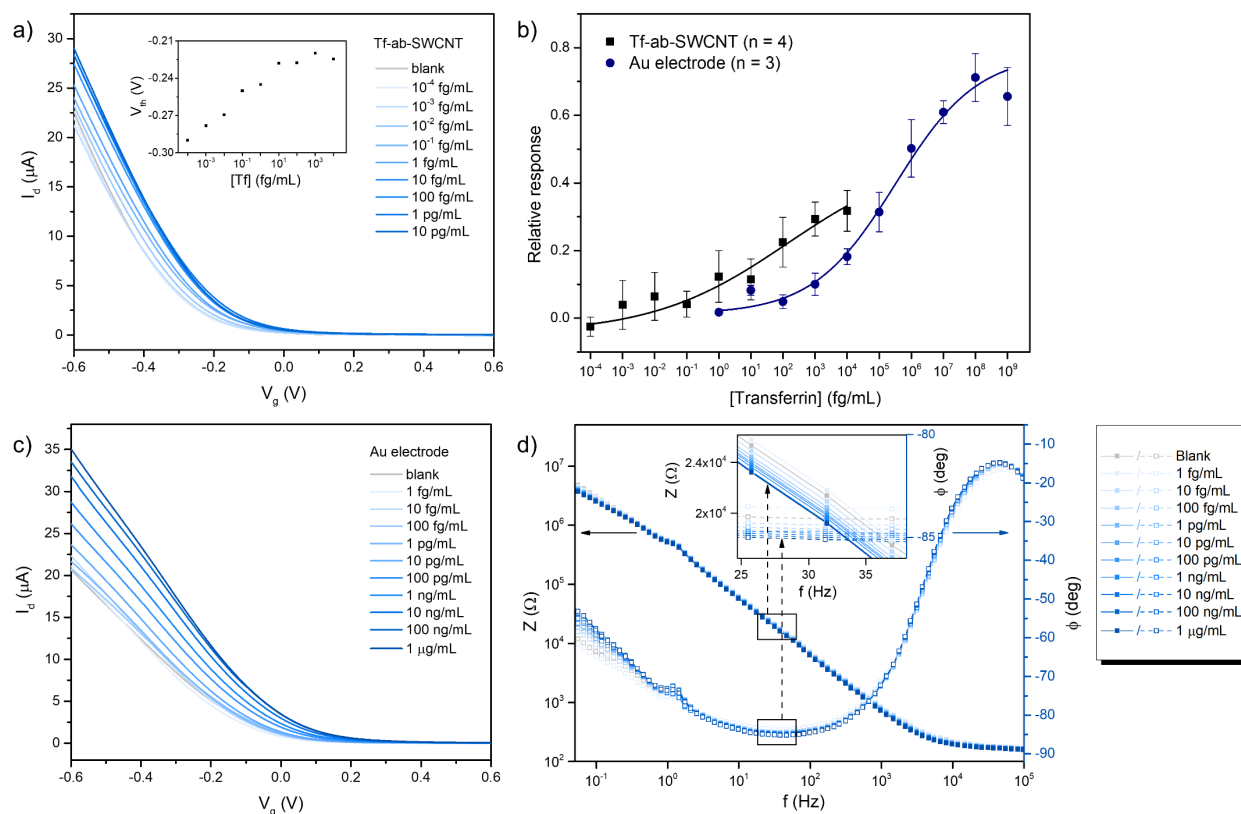


Figure 3-3 Detection of recombinant transferrin using sc-SWCNT FET devices. **(a)** FET characteristic curves of Tf-ab functionalized SWCNT (Tf-ab-SWCNT) FET device upon exposure to increasing concentration of recombinant transferrin. The inset shows the threshold voltage shift. **(b)** Calibration plot for transferrin detection using Tf-ab-SWCNT approach and Au electrode approach. Results are Mean \pm SD. The number (n) of devices used for calculation are indicated in the parenthesis in the legend. **(c)** FET characteristic curves of sc-SWCNT FET device with increasing concentration of recombinant transferrin absorbing on the Au gate electrode. **(d)** Bode plot of EIS measurement of the Au electrode upon transferrin binding. The inset shows a zoom-in view of the impedance of the Au electrode surface in the capacitive response region.

While Tf-ab functionalized sc-SWCNT FET sensor demonstrated ultrasensitivity toward transferrin, this type of sensor also suffered from quick saturation at around 1 pg/mL of transferrin due to the limited binding sites available on the Tf-ab functionalized sc-SWCNTs. It led us to the third approach where the gate electrode was replaced by a gold electrode, which provided a 2 mm diameter gold disk for binding target analyte. In this configuration, instead of altering the chemical environment of SWCNT surfaces, the transferrin was being absorbed on the gold surface of the gold disk electrode, and the capacitance in the gate/electrolyte interface is changed through modulation on the gate electrode, therefore changing the total capacitance between the gate and the semiconducting channels, inducing characteristic changes of the devices.¹⁹⁶⁻¹⁹⁸ **Figure 3-3c** showed an increase in the ON state current with transferrin absorbing on the Au surface, and the calibration curve, constructed the same way as previously described, indicated a limit of detection at 10 fg/mL and a dynamic range from 10 pg/mL to 10 ng/mL with a calibration sensitivity of 0.15 (**Figure 3-3b**, navy).

The capacitance change in the gate/electrolyte interface during transferrin detection was monitored using non-faradaic EIS. Non-faradaic EIS, which is performed without a redox probe, measures the impedance upon analyte binding to the gold surface by charging and discharging the double-layer capacitance, therefore eliminates the effect of charge transfer resistance (R_{ct}).^{199, 200} A decrease in the imaginary impedance was observed in the Nyquist plot, suggesting an increasing double-layer capacitance as higher concentrations of transferrin being absorbed on the Au electrode (**Appendix Figure B-6**).²⁰⁰ Bode plot (**Figure 3-3d**) also showed a decrease in the overall impedance with increasing concentrations of transferrin in the frequency range where capacitive response was dominant, indicated by the phase angle around -85° . These results can be explained as more transferrin molecules bind to the gold surface, more charges were stored within

the double layer, increasing the double-layer capacitance, which lead to the decrease in the overall impedance.²⁰¹ This increase in the gate capacitance with higher concentrations of transferrin consequently also induced the increase in transconductance (g_m) of the FET characteristics (**Appendix Figure B-7**),²⁰² which was observable as the increasing ON state current in the I- V_g curves.

Figure 3-3b compares the sensing performances of the Tf-ab-SWCNT and Au electrode approach for the detection of transferrin. Tf-ab functionalized sc-SWCNT FET devices exhibited ultrasensitivity at a limit of detection of 0.01 fg/mL while the Au electrode approach showed evident response toward transferrin at 10 fg/mL. The lower limit of detection of Tf-ab-SWCNT approach is consistent with the lower dissociation constant of the binding between transferrin and Tf-ab (18 fg/mL for Tf-ab and 202 pg/mL for Au electrode), which corresponds to the concentration at half-maximum response.²⁰³ However, transferrin sensing with Au electrode outperformed the Tf-ab-SWCNT approach in terms of dynamic range of the sensor and its calibration sensitivity, as Au electrode provided a larger sensing area, hence more available binding sites for transferrin molecules. Therefore, various factors, such as transferrin concentration, sensitivity and specificity requirements, need to be considered before choosing the optimal transferrin sensing method.

Our 3-step strategy for β 2-Tf detection was then applied to differentiate samples of CSF and serum. Transferrin component of both CSF and serum were studied using electrophoresis and western blot (**Appendix Figure B-8**). CSF, which contains β 2-Tf, showed two transferrin bands with the leading band representing β 2-Tf. Serum, on the other hand, only yielded one transferrin band due to the lack of β 2-Tf. Four pairs of CSF and serum samples were tested following the 3-step method, and the β 2-Tf detection in step 3 was carried out using both Tf-ab-SWCNTs and Au

electrode approach. Both detection methods achieved the differentiation between CSF and serum samples, but Tf-ab functionalized sc-SWCNT FET devices displayed better sensing performance by yielding higher signal and more reliable results due to the ultrasensitivity in the lower transferrin concentration range. However, as previously mentioned, the Au electrode approach might outperform the Tf-ab-SWCNT approach with higher transferrin concentration present in the sample. Therefore, the selection of the sensing approach in step 3 should depend on the transferrin concentration.

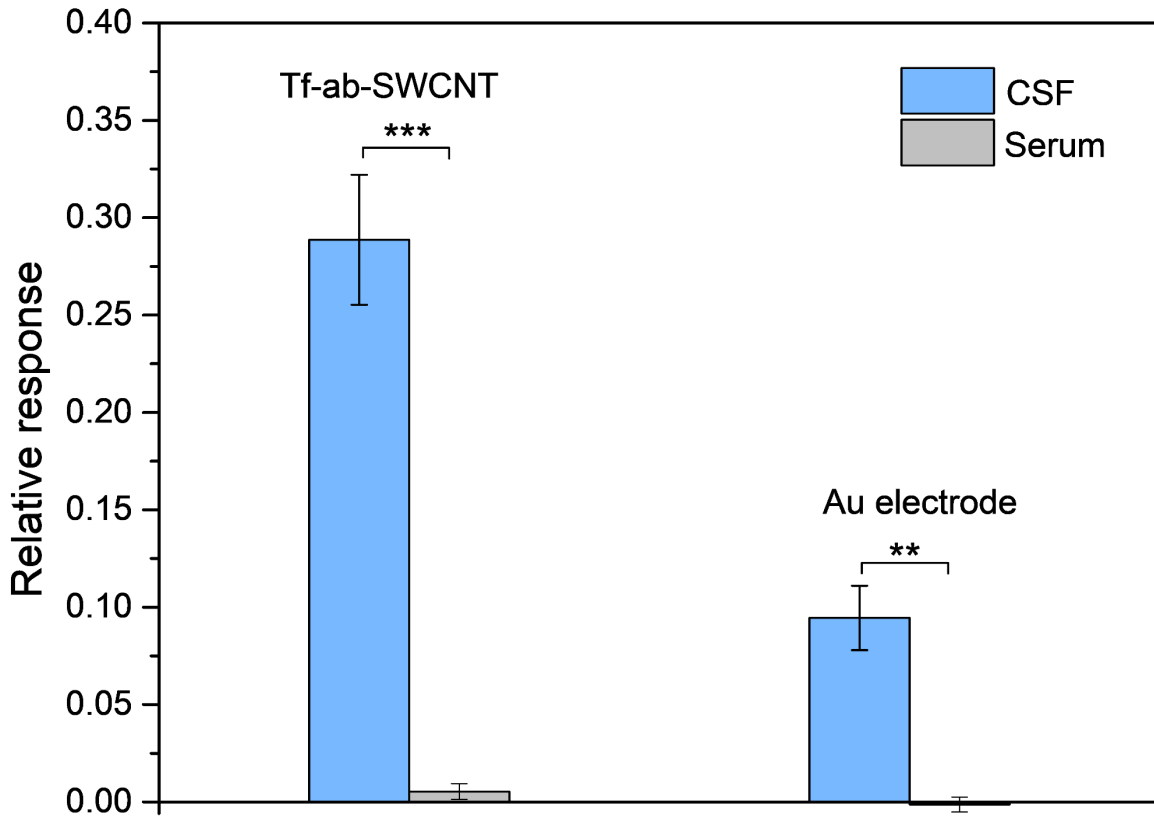


Figure 3-4 β_2 -Tf detection in CSF (blue) and serum (grey) using Tf-ab-SWCNT FET devices and Au electrode approach. Results are mean \pm SEM. The number (n) of devices tested for each sample was summarized in Appendix Table B-2. (ANOVA; **, $p < 0.01$; *, $p < 0.001$)**

The successful discrimination between CSF and serum samples employing our 3-step strategy with a sc-SWCNT FET biosensor platform suggested the potential for its application in the clinical practice for CSF leak detection. With the 3-step strategy and the sc-SWCNT FET biosensor platform, we shorten the detection time from at least 3-6 hours (using gel electrophoresis with Western blot) to around 1 h. Moreover, unlike radiographic and magnetic imaging methods, our method only requires simple instruments and easy operations, making CSF leak detection more accessible for patients in need.

3.5 Conclusions

In this work, we presented a 3-step strategy for rapid β 2-Tf detection in body fluids, which is required in clinical diagnostic of CSF leakage after traumatic brain injury (TBI) or surgical procedures. The 3-step strategy includes two steps of affinity columns for separating β 2-Tf from other proteins present in the fluid sample, and a third step using high purity sc-SWCNT FET devices for β 2-Tf detection. Both Tf-ab-SWCNT and Au electrode approach in step 3 have shown their capability of β 2-Tf detection with high sensitivity and reliability. Tf-ab functionalized sc-SWCNT FET devices exhibited ultrasensitivity at a limit of detection of 0.01 fg/mL with a dynamic range of 10 fg/mL to 1 pg/mL, hence suitable for the ultrasensitive β 2-Tf detection in sub-pg/mL range. On the other hand, transferrin sensing with Au electrode outperformed the Tf-ab-SWCNT approach in the ng/mL transferrin range with wider dynamic range and higher calibration sensitivity. By applying the 3-step strategy to body fluids, we have successfully differentiated CSF (positive) and serum (negative) samples using both Tf-ab-SWCNT and Au

electrode approach. Compared to current methods for CSF leak diagnosis, such as electrophoresis and imaging methods, our 3-step strategy is capable of offering high quality CSF leak detection with a short turnaround time, easy instrument access and simple operations, which could potentially benefit patient care for TBI patients and other people in need.

3.6 Acknowledgement

The work was supported by the National Science Foundation under Grant No. 2003302. The XplorA Raman-AFM/TERS system was purchased via Defense University Research Instrumentation Program (DURIP) grant from the Office of Naval Research, ONR (N000141410765).

4.0 Rapid Detection of SARS-CoV-2 Antigens using High-Purity Semiconducting Single-Walled Carbon Nanotube-Based Field-Effect Transistors

4.1 Chapter Preface

The aim of this work is to develop a rapid COVID-19 diagnostic tool utilizing high-purity semiconducting (sc-) single-walled carbon nanotube (SWCNT)-based field-effect transistor (FET) decorated with specific binding chemistry to assess the presence of SARS-CoV-2 antigens in clinical nasopharyngeal samples. The results showed that the SARS-CoV-2 antibody functionalized sc-SWCNT FET biosensor has achieved sub-fg/mL detection of SARS-CoV-2 antigens in calibration samples and an 82% accuracy with NAAT positive nasopharyngeal swab samples. The material contained in this chapter was published in *ACS Applied Materials & Interfaces* in 2021. The full citation is listed as Reference 187 in the bibliography section. Reprinted with permission from Shao et al., *ACS Appl. Mater. Interfaces*, **2021**, *13*, 10321–10327. Copyright 2021 American Chemical Society.

List of Authors: Wenting Shao, Michael R. Shurin, Sarah E. Wheeler, Xiaoyun He and Alexander Star

4.2 Introduction

Rapid detection of SARS-CoV-2 infection is critical for reducing morbidity and mortality of Coronavirus disease 2019 (COVID-19).²⁰⁴ The current methodology in assessing the present

infection of SARS-CoV-2 relies on nucleic acid amplification tests (NAAT) which detect the genetic material from SARS-CoV-2.²⁰⁵ While NAAT-based tests demonstrate excellent sensitivity for detection of viral RNA, it is a high complexity test requiring specialized equipment and training, and current shortages mean results can take up to a week to be returned in some areas.

Testing for SARS-CoV-2 antigens is an appropriate addition to NAAT. Antigen detection in general is relatively inexpensive, can have a short turnaround time, and is amenable to point-of-care diagnostic methodologies. Currently existing rapid antigen testing tools in both laboratories and clinics are mostly based on lateral flow immunoassay (LFA) platforms.^{25, 26, 206-209} LFA is cheap and easily mass-produced, making it advantageous for rapid in-field detection of SARS-CoV-2 antigens.³⁶ However, the sensitivity of LFA is generally not high enough to accurately screen COVID-19 patients.

Among several potentially useful detection methods for viral protein detection, field-effect transistor (FET)-based biosensing devices are advantageous as they offer high sensitivity, small size, and label-free and real-time detection.²¹⁰⁻²¹² Recently, graphene-based FETs have been applied for COVID-19 detection. Zhang et al.²¹³ have developed a label-free graphene-FET immunosensor that can identify and capture the SARS-CoV-2 spike protein S1 within 2 min with a limit of detection of 0.2 pM. The detection relies on the highly specific interaction between SARS-CoV-2 spike protein S1 and the SARS-CoV-2 spike S1 subunit protein antibody (CSAb) or human angiotensin-converting enzyme 2 (ACE2)-functionalized graphene surface. Seo et al.²¹⁴ developed a SARS-CoV-2 viral detection platform with a graphene-based FET biosensing device functionalized with the anti-SARS-CoV-2 spike antibody. The reported COVID-19 FET sensor detects SARS-CoV-2 spike proteins in nasopharyngeal swabs without preprocessing of the samples and can detect SARS-CoV-2 when RNA is present at 2.4×10^2 copies/mL. Both graphene-

based FET sensors showed promise for applications in COVID-19 diagnosis albeit with lower sensitivity compared to NAAT but with a short detection time.

Herein, we developed a SARS-CoV-2 antigen (Ag) FET nanobiosensor by employing high-purity semiconducting (sc-) single-walled carbon nanotube (SWCNT) functionalized with a specific antibody to access the presence of two SARS-CoV-2 structural proteins: spike protein (S antigen, SAg) and nucleocapsid protein (N antigen, NAg) (**Figure 4-1**). High-purity sc-SWCNTs offer high on-state conductance and high on/off ratio for FETs, providing higher analytical sensitivity toward the target analyte compared to other carbon nanomaterials such as unsorted SWCNT and graphene. Sc-SWCNT FETs have demonstrated value as ultrasensitive biosensors including applications as aptasensors^{128, 215} and label-free protein sensors.^{110, 129, 130} Moreover, the SWCNT is significantly cheaper and more widely available than CVD graphene films, thus lowering the cost of SWCNT FET sensors.

By integrating the anti-SARS-CoV-2 spike protein antibody (SAb) and anti-nucleocapsid protein antibody (NAb) with high-purity sc-SWCNTs, our SARS-CoV-2 Ag FET biosensor showed ultrasensitivity at an order of magnitude lower than other sensors to date and high analytical specificity towards SARS-CoV-2 SAg and NAg in calibration samples. Qualitative comparison of the NAAT and our SARS-CoV-2 Ag FET device indicated successful discrimination between positive samples and negative samples, suggesting their potential in COVID-19 diagnostics.

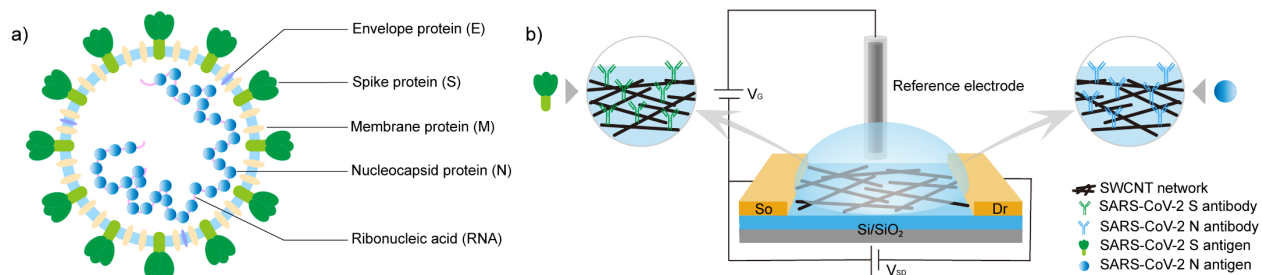


Figure 4-1 Detection of SARS-CoV-2 Ag using SWCNT-based FET biosensors. (a) Schematic structure of SARS-CoV-2 to demonstrate targeting proteins. (b) Schematic illustration of a liquid-gated SWCNT FET for detection of SARS-CoV-2 SAg and NAg. Interdigitated gold electrodes (yellow blocks) are configured as the source (So) and drain (Dr). Source-drain bias (V_{sd}) is 50 mV. Gate voltage (V_g) is applied through a silver/silver chloride reference electrode. Insets show SAB- and NAb-functionalized SWCNTs for specific detection of SAg and NAg, respectively.

4.3 Experimental Section

Device fabrication. Interdigitated gold electrodes were patterned on a Si/SiO₂ substrate using photolithography, forming 10 μm channels. Semiconducting SWCNTs (IsoSol-S100, Raymor Industries Inc.) were prepared at 0.02 mg/mL in toluene, and deposited between gold electrodes via dielectrophoresis (DEP) with an ac frequency of 100 kHz, applied bias voltage of 10 V, and bias duration of 120 s. The devices were annealed at 200 $^{\circ}\text{C}$ for 1 h before use.

The functionalization of the SARS-CoV-2 antibody on SWCNTs was achieved via 1-ethyl-3-(3-dimethylaminopropyl)carbodiimide (EDC)/N-hydroxysulfosuccinimide (sulfo-NHS) coupling. Specifically, 50 μL of EDC/sulfo-NHS solution [50 mM/50 mM in 1X phosphate-buffered saline (PBS), pH = 5.5] was first added to the devices to activate the carboxylic acid

groups on SWCNTs. The devices were then rinsed with nanopure water and incubated with 2 μ L of 100 μ g/mL SARS/SARS-CoV-2 coronavirus spike protein (subunit 1) polyclonal antibody (Thermo Fisher Scientific, Waltham, MA, USA; Cat# PA5-81795) for 12 h at 4 $^{\circ}$ C for SAb-functionalized devices, and 4 μ L of 50 μ g/mL anti-SARS-CoV-2 NP antibody (Clone# 6F10) (BioVision Inc., Milpitas, CA, USA; Cat# A2060) for NAb-functionalized devices. After a thorough rinse with nanopure water, the devices were soaked in a blocking buffer (0.1% Tween 20 and 4% polyethylene glycol in PBS) for 30 min to block unreacted surfaces. After blocking, the devices were rinsed again with nanopure water before any FET measurements.

Fluorescence imaging. Fluorescence images were obtained using an Olympus 1X81/1X2-UCB microscope. The enhanced green fluorescent protein (EGFP) antibody (Antibodies-online Inc, Limerick, PA, USA) was immobilized on the SWCNT FET device using the same method as described in the “Device Fabrication” section. EGFP protein solution (2 μ L, 10 μ g/mL) was then added to the device and incubated for 10 min at room temperature. Fluorescence images before and after the addition of EGFP were captured under an excitation of 489 nm. As a control, 2 μ L of 10 μ g/mL EGFP protein solution was also added to a bare SWCNT FET device with blocking. Fluorescence images of the bare SWCNT FET device before and after EGFP binding were also taken under an excitation of 489 nm.

UV-Vis-NIR absorption spectroscopy. Sc-SWCNTs (100 μ L, 0.02 mg/mL) were drop casted on a 1” \times 1” quartz slide and heated at 200 $^{\circ}$ C to evaporate the solvent. UV-vis-NIR spectra of sc-SWCNT were collected using a PerkinElmer LAMBDA 900 UV-vis-NIR spectrophotometer.

Atomic force microscopy. Atomic force microscopy (AFM) data were collected using Bruker Multimode 8 AFM system with a Veeco Nanoscope IIIa controller in the tapping mode.

The AFM image and height profiles were processed and obtained in Gywddion.

X-ray photoelectron spectroscopy. X-ray photoelectron spectroscopy (XPS) data were generated on a Thermo ESCALAB 250 Xi XPS using monochromated Al K α X-rays as the source. A 650- μ m spot size was used, and the samples were charge-compensated using an electron flood gun.

Raman spectroscopy. The XplorA Raman-AFM/TERS system was used to record all Raman spectra. The radial breathing mode (RBM) region was recorded using a 785 nm (100 mW) excitation laser operating at 1% power. D and G peak regions were recorded using a 638 nm (24 mW) excitation laser operating at 1% power.

FET measurements. Liquid-gated FET device configuration was employed to study the FET transfer characteristics of SARS-CoV-2 antibody-functionalized FET devices for the detection of SARS-CoV-2 antigens. Nanopure water was used as the gating electrolyte. FET characteristic curves were recorded by collecting the source-drain current (I_d) while sweeping the gate voltage from +0.6 to -0.6 V versus a Ag/AgCl reference electrode with a fixed drain voltage of 50 mV.

A series of SARS-CoV-2 spike S1-His recombinant protein (Sino Biological, Beijing, China; Cat# 40591-V08H) solutions ranging from 0.55 fg/mL to 55 μ g/mL, and recombinant coronavirus nucleoprotein (BioVision Inc.; Cat# P1523) ranging from 0.016 fg/mL to 16 μ g/mL were prepared in PBS. All protein solutions were tested from the lowest to the highest concentrations. For each measurement, 2 μ L of the protein solution was added to the antibody-functionalized devices and incubated for 2 min. The devices were then washed three times with nanopure water to remove any unbound protein and measured in nanopure water as the gating electrolyte.

The relative response (R) of each FET device was calculated using $R = \Delta I_d / I_0$ at $-0.5 V_g$, where $\Delta I = I_d - I_0$, and I_0 is the drain current in nanopure water before antigen exposure at $-0.5 V_g$. The final results reported were averaged relative responses of two to six devices with standard deviation (SD) as error bars. The number of devices (n) tested for each experiment was specified in the figure.

Clinical sample tests. Remnant nasopharyngeal swab samples tested by NAAT for SARS-CoV-2 RNA on emergency use authorized platforms for standard clinical care were used under the auspices of the University of Pittsburgh IRB study number 20040220. A total of 28 PCR-positive samples and 10 negative nasopharyngeal swab samples were tested. Each sample (10 μ L) was added to the antibody-functionalized devices and incubated for 2 min. After 2 min, the sample was removed from the devices and the devices were washed three times with water. FET measurements were taken in water as the gating electrolyte.

The relative responses were calculated using the same method as previously described in “FET Measurements”. The final results reported were averaged relative responses of one to four devices with SD as error bars. The number of devices (n) tested for each sample is summarized in the supporting information.

4.4 Results and Discussion

As shown in **Figure 4-2a**, the sensor chip contains four FET devices with interdigitated gold source and drain electrodes patterned on a Si/SiO₂ substrate. The channel length is 10 μ m. To fabricate the SWCNT FET devices, sc-SWCNTs were deposited between interdigitated gold electrodes via DEP, forming dense and interconnected networks on the Si/SiO₂ surface (**Figure**

4-2b). UV-vis-NIR absorption spectroscopy was utilized to investigate the semiconducting content in the sc-SWCNTs (**Appendix Figure C-1**), and the absence of the M_{11} peak confirmed the high-purity semiconducting content.

SARS-CoV-2 SAb and NAb were conjugated onto sc-SWCNTs via EDC/sulfo-NHS coupling between the carboxylic acid groups on the SWCNT sidewalls and the amine groups on the antibody. The EDC/sulfo-NHS coupling of antibodies on sc-SWCNTs was visualized using the EGFP antibody and EGFP (**Appendix Figure C-2**). The morphology of SAb on SWCNTs was characterized using scanning electron microscopy (SEM) and AFM (**Figure 4-2c,d**). The height profiles indicated a 12-15 nm increase in height after SAb immobilization (**Figure 4-2e**). XPS provided complementary evidence for the integration of the antibody on SWCNTs. The high-resolution C 1s scan of the bare SWCNTs confirmed the presence of oxygenated defect sites on SWCNTs (**Appendix Figure C-3**). The appearance of the N 1s peak and C-N (285.3 eV) peak after antibody coupling also suggested successful conjugation of the antibody on SWCNTs (**Figure 4-2f,g** and **Appendix Figure C-3**). Raman spectroscopy revealed the effect of antibody functionalization on SWCNTs. Two major peaks were observed in the radial breathing mode (RBM) region. The peak that ranged from 125 to 225 cm^{-1} decreased in intensity during functionalization, suggesting a preference of antibody functionalization on SWCNTs with larger diameters (**Figure 4-2h**).²¹⁶ Meanwhile, the I_D/I_G ratio increased from 0.044 to 0.085, indicating an increase in the degree of functionalization on SWCNTs due to the covalent bonding of antibodies to the SWCNTs (**Figure 4-2i**). In FET transfer characteristics (**Figure 4-2j,k**), the shift of threshold voltage toward more negative gate voltages and the decrease in the device conductance in the p-type region also revealed the successful functionalization of SAb and NAb on sc-SWCNTs. Further shift of the threshold voltage and decrease in the conductance were

detected after the addition of blocking buffer (0.1% Tween 20 and 4% polyethylene glycol) to prevent nonspecific binding. Meanwhile, the gate leakage current was negligible compared with the ON state source-drain current, suggesting good insulation between the gate and source-drain electrodes, therefore no encapsulation was required for Au electrodes (**Appendix Figure C-4**).

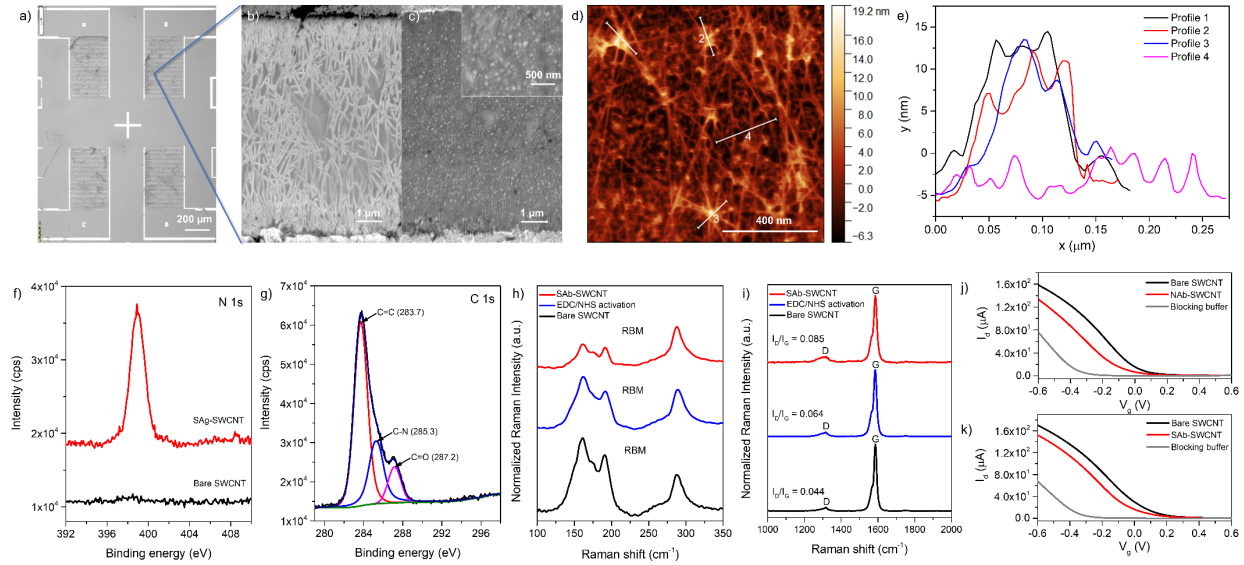


Figure 4-2 Characterizations of SARS-CoV-2 antibody-functionalized SWCNT FET devices. (a) Microscopic image of SWCNT FET devices. (b) SEM image of SWCNT networks deposited on a FET device and (c) after SAb functionalization. The inset shows a zoom-in view of SAb-functionalized SWCNTs. (d) AFM image of SAb-functionalized SWCNTs. (e) Height profiles of SAb immobilized on the SWCNT and bare SWCNTs. (f) High-resolution XPS spectra of N 1s of the bare SWCNT and antibody-functionalized SWCNT, and (g) C 1s of the antibody-functionalized SWCNT with deconvolutions of the overall signal. (h) RBM region and (i) D and G peak regions of Raman spectra of the SWCNT during antibody functionalization. The RBM region was recorded using a 785 nm excitation laser. All spectra were normalized to the Si peak at 507 cm^{-1} . D and G peak regions were recorded using a 638 nm excitation laser. All spectra were normalized to the G peak at 1587 cm^{-1} . (j) FET transfer characteristics of an SWCNT FET device during NAb functionalization and (k) SAb functionalization.

We first investigated the performance of our SARS-CoV-2 Ag FET biosensors using SARS-CoV-2 SAg and NAg in calibration samples. All FET transfer characteristics were recorded by employing a liquid-gated FET configuration using nanopure water as the gating media to eliminate the impact of different ionic strength on the sensing results. **Figure 4-3a** shows the $I-V_g$ curve of SARS-CoV-2 SAb-functionalized FET devices for the detection of SAg. A shift toward more positive threshold voltages can be observed in the FET characteristics when only 0.55 fg/mL SAg was introduced to the device. The threshold voltage shifted further toward more positive values with increasing concentration of SAg (**Appendix Figure C-5a**). This positive shift of the $I-V_g$ curve can be attributed to the introduction of negatively charged SAg ($pI = 6.24$) near the SWCNT surface,²¹⁷ inducing additional hole carriers, thus p-doping the SWCNTs.^{110, 163} The calibration curve (**Figure 4-3b**) was constructed by plotting the relative response (R , $R = \Delta I_d/I_0$, where $\Delta I = I_d - I_0$, and I_0 is the drain current in nanopure water before antigen exposure at $-0.5 V_g$) against concentrations of SAg in a logarithmic scale, where the dynamic range of the SAg sensor can be determined to be 5.5 fg/mL to 5.5 pg/mL and the calibration sensitivity, defined as the slope of the linear region of the calibration curve, to be 0.25 by fitting the calibration curve (**Appendix Figure C-5b**). Control experiments with NAg demonstrated the high specificity of the SAb-functionalized devices. The low relative response of the bare SWCNT FET sensor with or without blocking toward SAg further indicated that the responses of the SAb-functionalized device toward SAg were indeed induced by the specific antigen-antibody interaction.

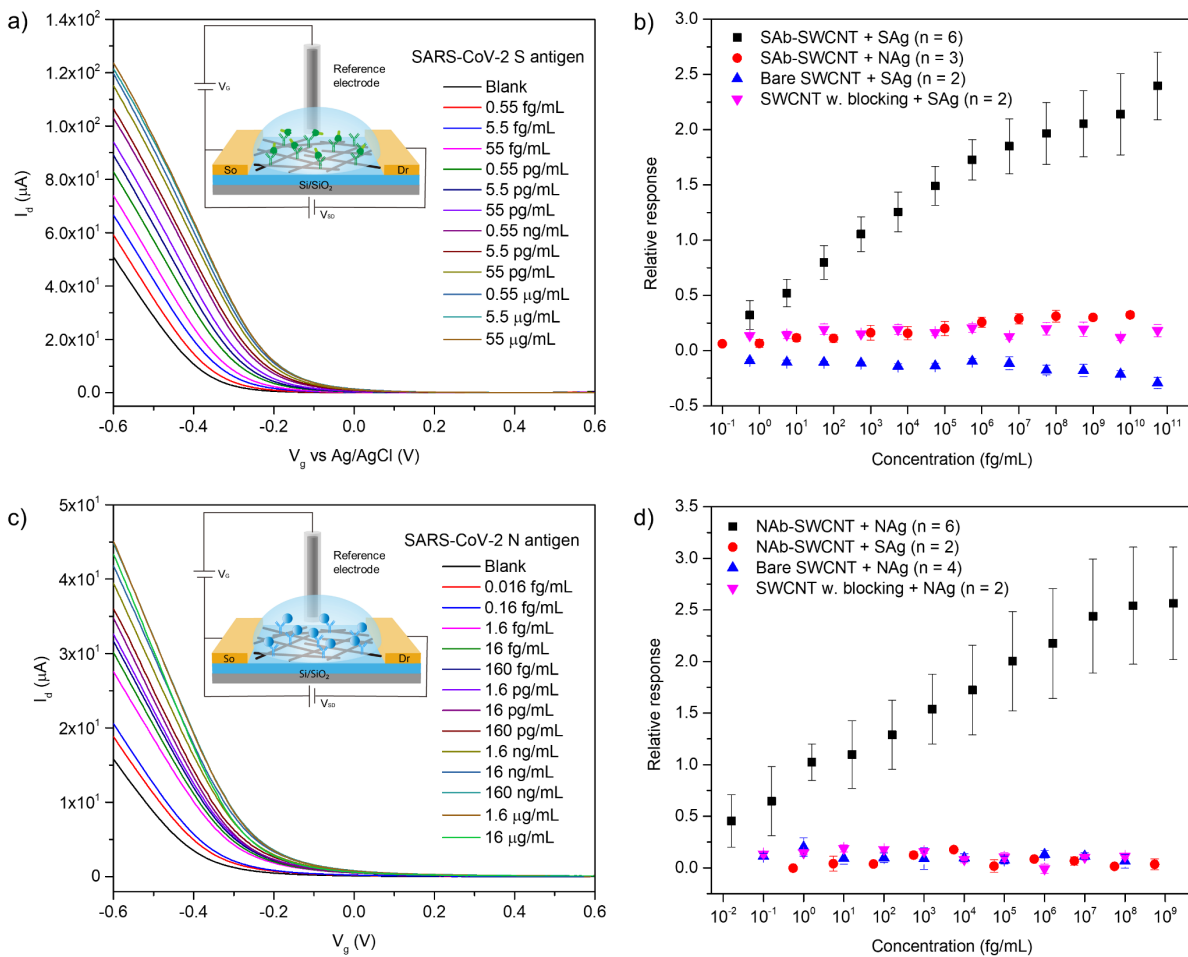


Figure 4-3 Detection of recombinant SARS-CoV-2 antigen proteins. (a) FET characteristic curves of SAB-functionalized SWCNT (SAB-SWCNT) FET devices upon exposure to increasing concentration of recombinant SARS-CoV-2 SAg. The inset shows the schematic illustration of FET configuration for SAg detection. (b) Calibration plot for SAg detection and nonspecific protein detection. (c) FET characteristic curves of NAb-functionalized SWCNT (NAb-SWCNT) FET devices upon exposure to increasing concentration of recombinant SARS-CoV-2 NAg. The inset shows the schematic illustration of FET configuration for NAg detection. (d) Calibration plot for NAg detection and nonspecific protein detection. All data points plotted in the calibration plots are mean \pm SD. The number of devices (n) used for calculation is indicated in the parenthesis in the legend.

Similar to SAg detection, FET transfer characteristics of NAb-functionalized FET devices showed a consistent shift of the threshold voltage towards the more positive region with increasing NAg concentration (**Figure 4-3c** and **Appendix Figure C-6a**) due to the electrostatic gating effect. However, with the addition of positively charged NAg, the sensing mechanism is likely due to the neutralization of the positively charged antibody upon NAg binding.²¹⁸ By fitting the calibration curve, the dynamic range is found to be 16 fg/mL to 16 pg/mL and the calibration sensitivity is 0.22, displaying similar sensing performance to SAg detection (**Appendix Figure C-6b**). Meanwhile, the NAb-functionalized FET devices showed minimal responses to nonspecific proteins, and SWCNT FET devices without NAb conjugation also did not respond to the addition of NAg, exhibiting the high specificity of the NAg sensor (**Figure 4-3d**).

Our SARS-CoV-2 Ag FET biosensors were then tested with clinical samples. A total of 28 NAAT positive samples and 10 NAAT negative samples were tested using both SAb- and NAb-functionalized FET biosensors. All clinical samples were nasopharyngeal swabs suspended in the viral transport medium (VTM), and the viral load of each sample was measured by approved FDA EUA NAAT assays. The existing literature indicates that the NAAT and antigen detection are biologically well correlated but not 100% concordant.^{21, 219} The NAAT can detect RNA before a significant antigen is produced, additionally, the temporal course of the antigen versus RNA clearance after active infection is unclear. **Figure 4-4** summarizes the relative responses of both SAb- and NAb-functionalized sensors for all samples and blank VTM. A total of 23 out of 28 SAb-functionalized FET devices responded positively to NAAT positive samples, consistent with what was observed previously, yielding a 17.8% false negative rate compared to the EUA NAAT. On the other hand, 7 out of 10 gave negligible or negative responses toward NAAT-negative samples. The blank VTM, which contains Hank's balanced salt solutions, fetal bovine serum

(FBS), gentamicin, and amphotericin B, only induced small negative relative response of the devices. Therefore, the negative responses and false positive responses from the NAAT negative samples may come from other biological species collected from the nasopharyngeal swab or represent the continued presence of the antigen after RNA clearance. The results suggested that our SAb-functionalized FET biosensor has the potential to work as a rapid clinical SARS-CoV-2 antigen detection diagnostic.

The NAb-functionalized FET devices demonstrated less effective discrimination between positive and negative samples as 15 out of 28 positive samples produced positive responses. Moreover, the induced responses are in general lower than those of SAb-functionalized devices. The less effective detection of NAg may be attributed to the lower concentration of available NAg present in the clinical samples. While SAg is on the surface of SARS-CoV-2 virus, NAg, whose primary function is to form a capsid to protect the viral genome and enter the host cell, is released only when the virus enters the host cell.²²⁰⁻²²² Without further sample processing, NAg might be limited within the virus or infected cell and therefore cannot be detected. For negative samples, although NAb-functionalized devices yielded the same false positive rate as SAb-functionalized devices, they had increased comparative responses to negative samples and blank VTM. This may indicate a higher susceptibility of NAb-functionalized devices to nonspecific binding of biomolecules or cross-reactivity of the antibody with other proteins. However, it is worth mentioning that the results for NAg detection are antibody-specific. Better sensing performance might be achieved using a different NAb.

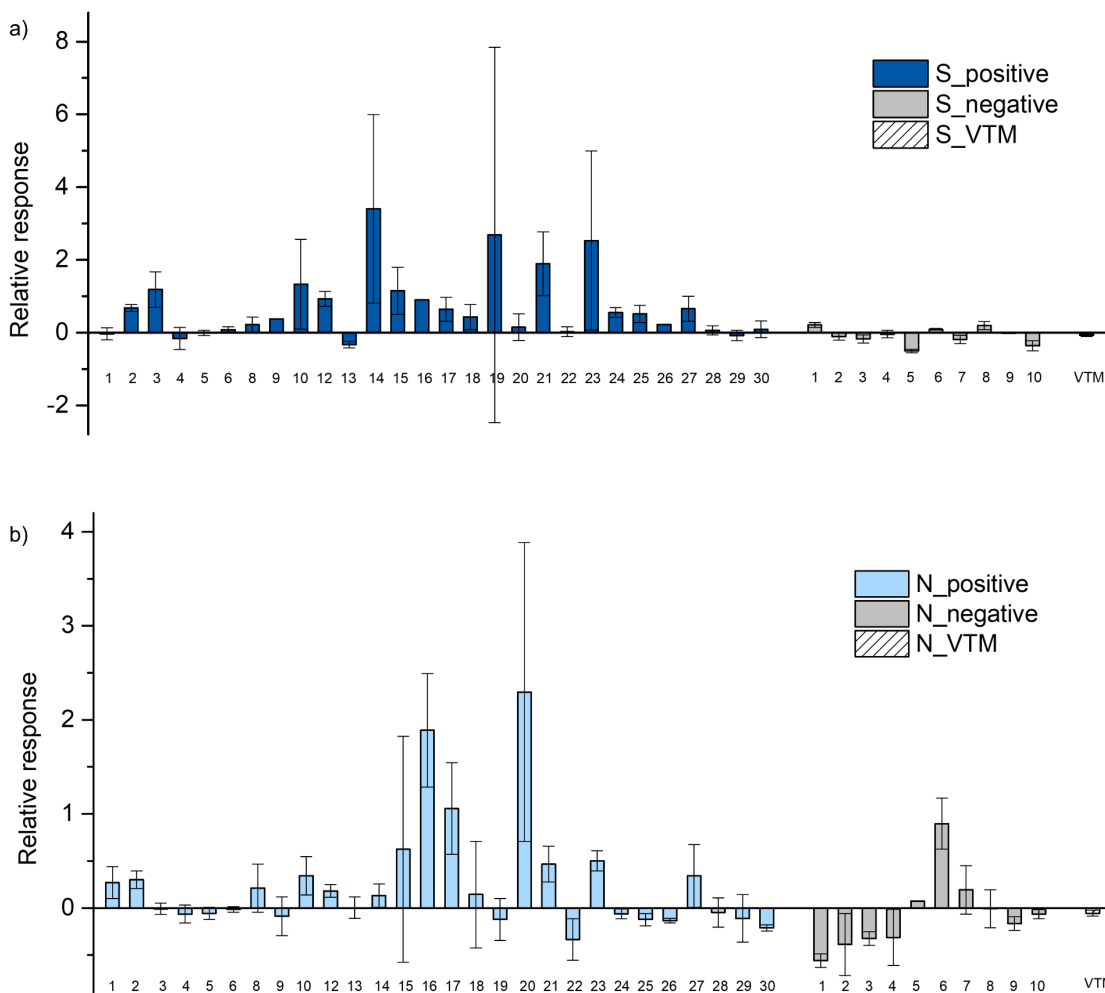


Figure 4-4 Clinical sample tests with a SAb and NAb functionalized FET devices. (a) Sensing performance of SAb-functionalized devices. (b) Sensing performance of NAb-functionalized devices. All data plotted are mean \pm SD. The number of devices (n) tested for calculation are summarized in Appendix Table C-1.

4.5 Conclusions

In conclusion, we used SARS-CoV-2 antibody-functionalized SWCNT-based FET biosensors to assess the presence of the SARS-CoV-2 antigen in less than 5 min and at a few cents per test. Both SAb- and NAb-functionalized FET biosensors exhibited ultrasensitivity and high

specificity towards their specific SARS-CoV-2 antigen in calibration samples. The limit of detection is determined to be 0.55 fg/mL for SAg and 0.016 fg/mL for NAg. Our SARS-CoV-2 Ag FET biosensor also achieved rapid detection of SARS-CoV-2 antigens in clinical samples without prior sample processing, and the results suggested that SAb-functionalized devices performed better than NAb-functionalized devices in discriminating COVID-19 positive and negative samples collected from nasopharyngeal swabs, and are less susceptible to nonspecific species present in the clinical samples. Furthermore, our sc-SWCNT FET detection assay approach opens the opportunity for multiplex detection of not only viral antigens but also antibodies recognizing these antigens.

4.6 Acknowledgement

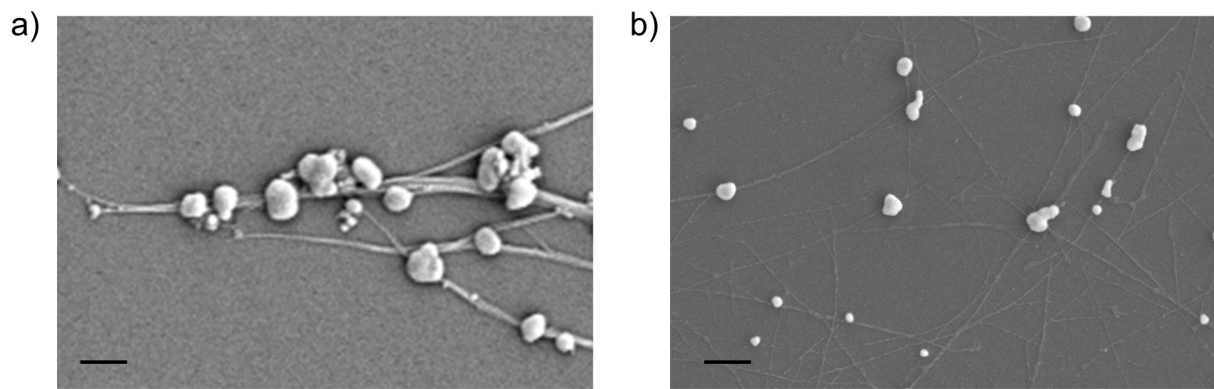
This study was supported by a grant awarded under the Pitt Innovation Challenge (PInCh), through the Clinical and Translational Science Institute at the University of Pittsburgh. The authors would like to acknowledge Dr. Esta Abelev from the Nanoscale Fabrication and Characterization Facility at University of Pittsburgh for obtaining the SEM images. The XplorA Raman-AFM/TERS system was purchased via Defense University Research Instrumentation Program (DURIP) grant from the Office of Naval Research, ONR (N000141410765).

5.0 Future Outlook

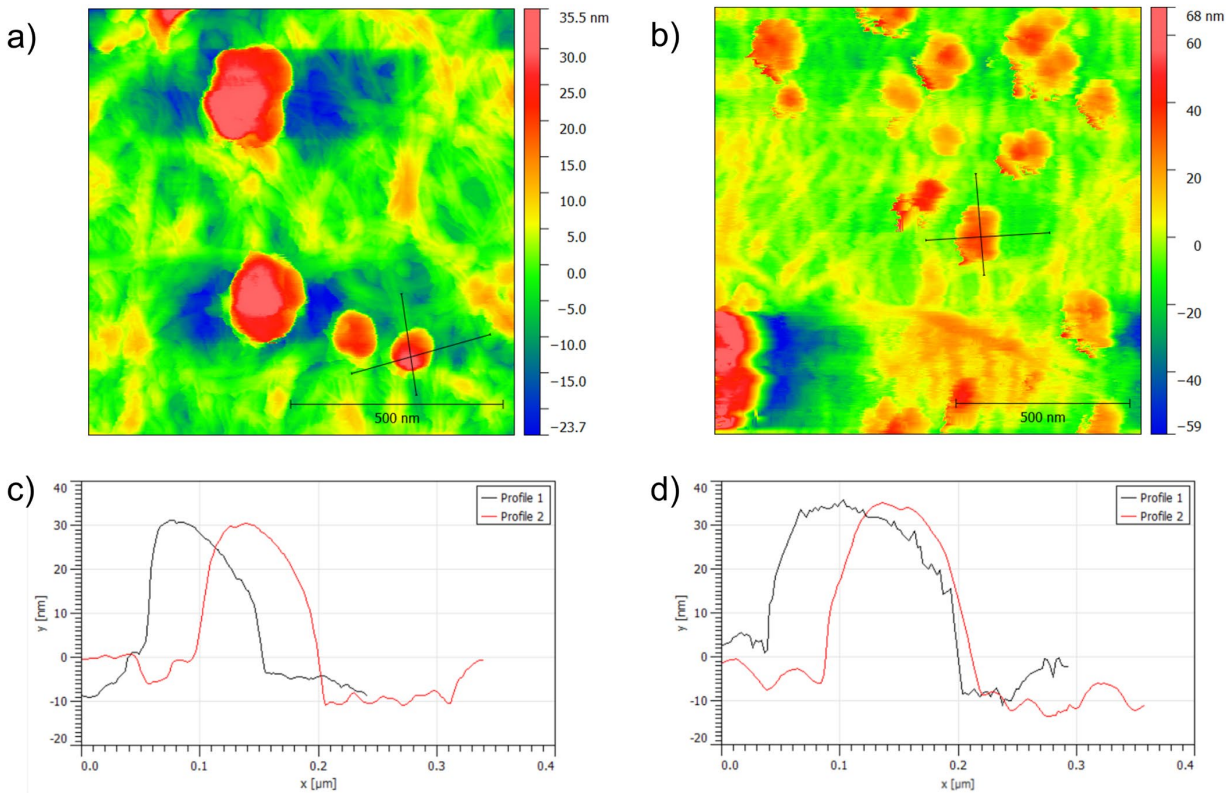
The sc-SWCNT FET detection assay approach presented in this dissertation opens the opportunity for a variety of disease relevant protein detection. Future endeavors will be focusing on improving sensitivity, specificity, reproducibility, and reliability of sc-SWCNT based FET biosensors for protein sensing.

The protein sensing performances of sc-SWCNT FET devices that based on antibody-antigen interactions are highly dependent on the antibody used. Therefore, finding the optimal biorecognition element for the FET sensing devices is necessary to improve the avidity and expand the dynamic range of the devices. On the other hand, controllable deposition of sc-SWCNTs on FET devices, such as inkjet printing, is key to produce FET devices with low variability, thus improving the reproducibility of sensing results. To improve the reliability of sc-SWCNT FET biosensors as potential disease diagnostic tools, a sensor array composed of sc-SWCNT FET biosensors decorated with various specific receptors for the related proteins can be developed as a multiplex sensor. Moreover, a high throughput automated sensor test system can be developed, which will drastically increase the efficiency of disease relevant protein testing in clinical laboratories.

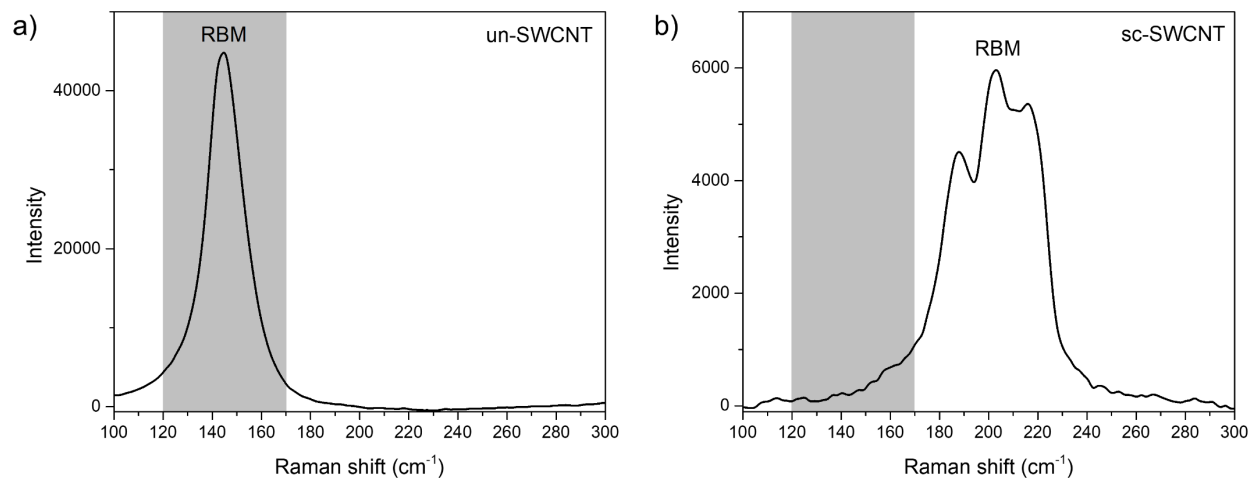
Appendix A Chapter 2 Supporting Information



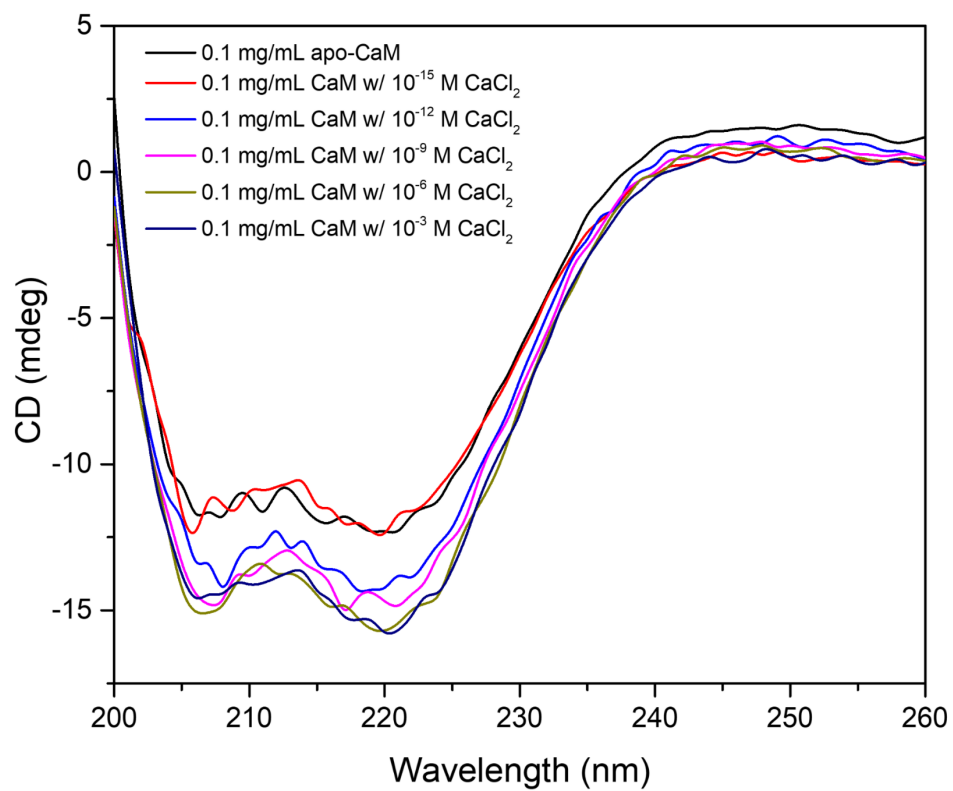
Appendix Figure A-1 SEM characterization of Au-un-SWCNTs and Au-sc-SWCNTs. (a) SEM image of AuNPs decorated un-SWCNTs. (b) SEM image of AuNPs decorated sc-SWCNTs. Both SEM images show an area of 1578 nm X 2353 nm on the device surface. It can be observed that less un-SWCNTs were deposited on the substrate than sc-SWCNT, indicating that sc-SWCNT formed denser networks than un-SWCNTs. [Scale bar: (a) 200 nm; (b) 200 nm]



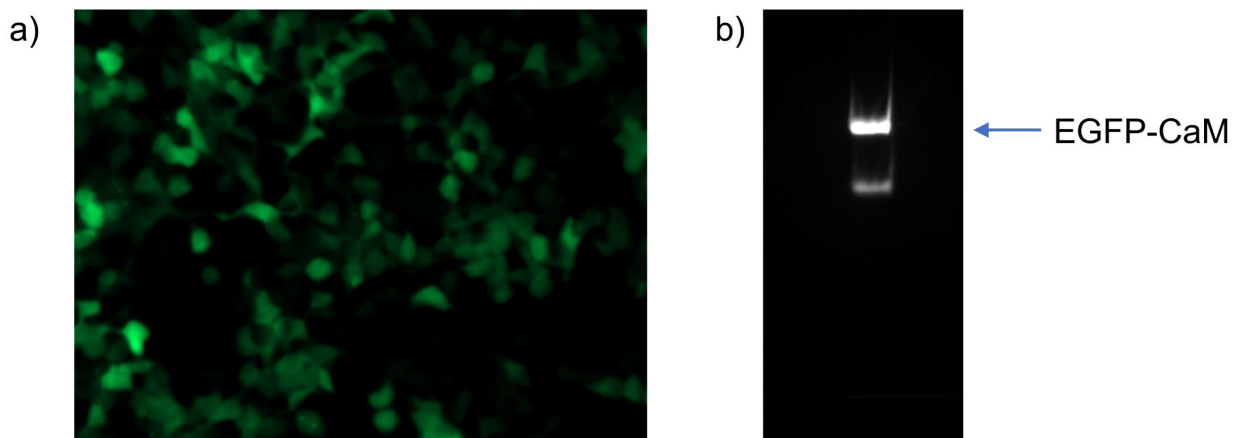
Appendix Figure A-2 AFM characterization of Au-unSWCNTs before and after CaM binding. (a) AFM image of Au-SWCNTs. (b) AFM image of Au-SWCNTs after CaM binding. (c) Height profile of Au-SWCNTs. (d) Height profile of CaM-Au-sc-SWCNTs.



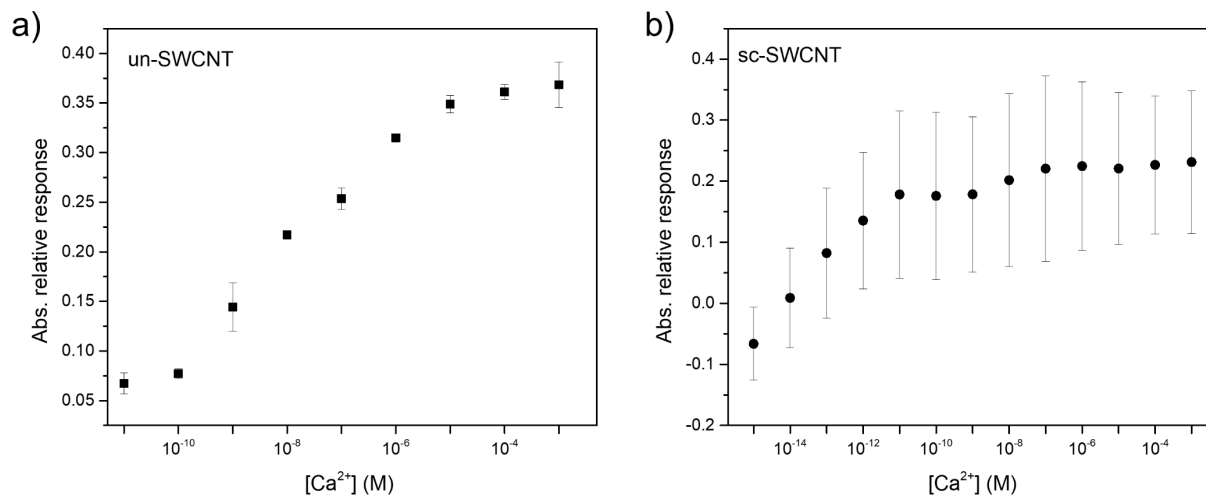
Appendix Figure A-3 Raman spectroscopy characterization of un-SWCNTs and sc-SWCNTs in the RBM region. (a) RBM peaks of un-SWCNTs. (b) RBM peak of sc-SWCNTs. Both spectra were recorded under 785 nm laser excitation. Peaks in the shaded area from 120 cm⁻¹ to 170 cm⁻¹ are associated with the metallic features of SWCNTs. un-SWCNT has an RBM peak centered around 145 cm⁻¹. In contrast, this peak is absent in sc-SWCNT, a broad and splitting RBM peak arises at 204 cm⁻¹ instead. This result confirms the high purity content of sc-SWCNT.^{74, 79, 98}



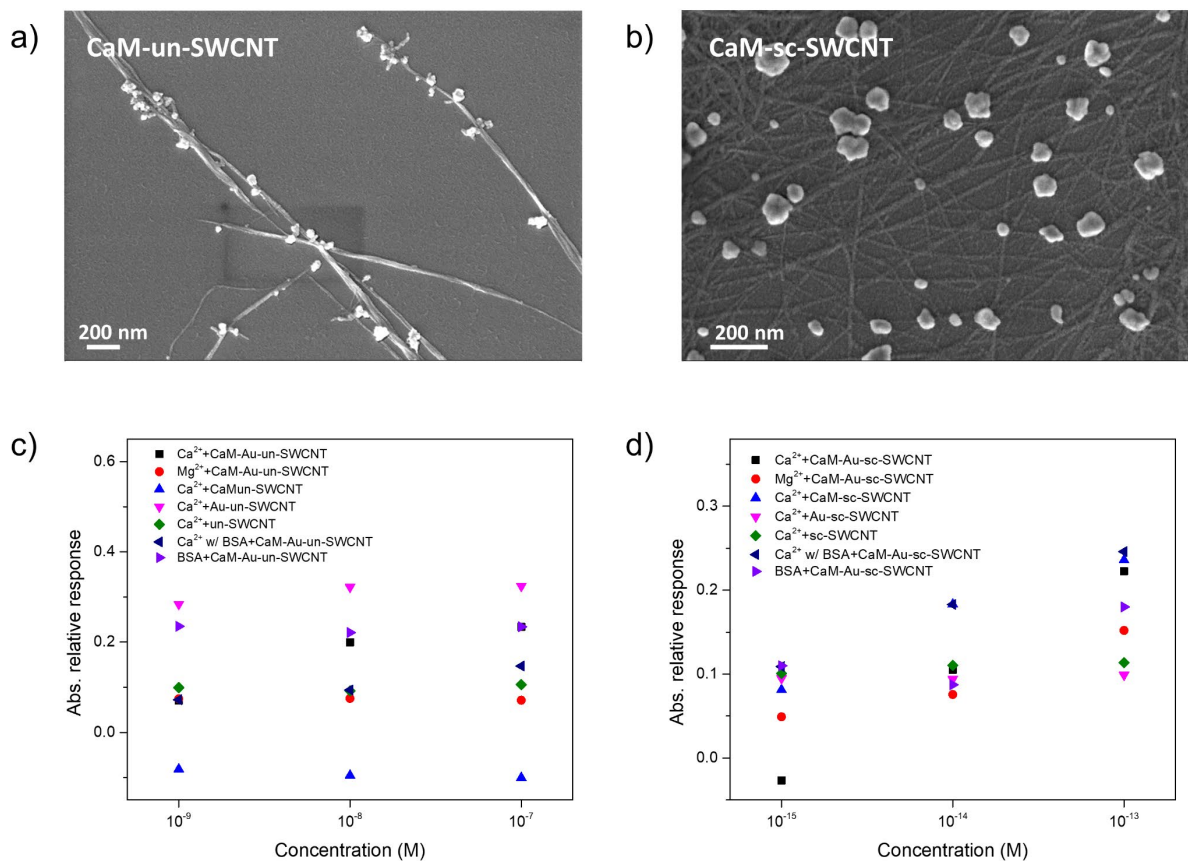
Appendix Figure A-4 Circular Dichroism solution spectra of calcium-free CaM (apo-CaM) and calcium-bound CaM with different concentrations of CaCl_2 .



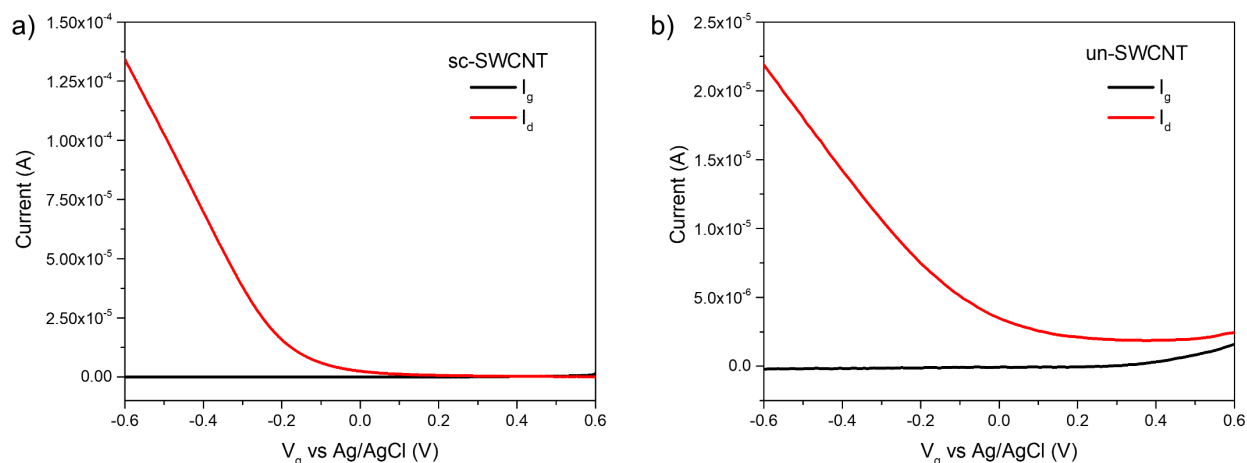
Appendix Figure A-5 Expression of EGFP-CaM in HEK293T cells. (a) Successful expression of EGFP-CaM in HEK293T cells was confirmed by live-cell imaging using Zeiss microscope. (b) In-gel fluorescence showing purified EGFP-CaM protein.



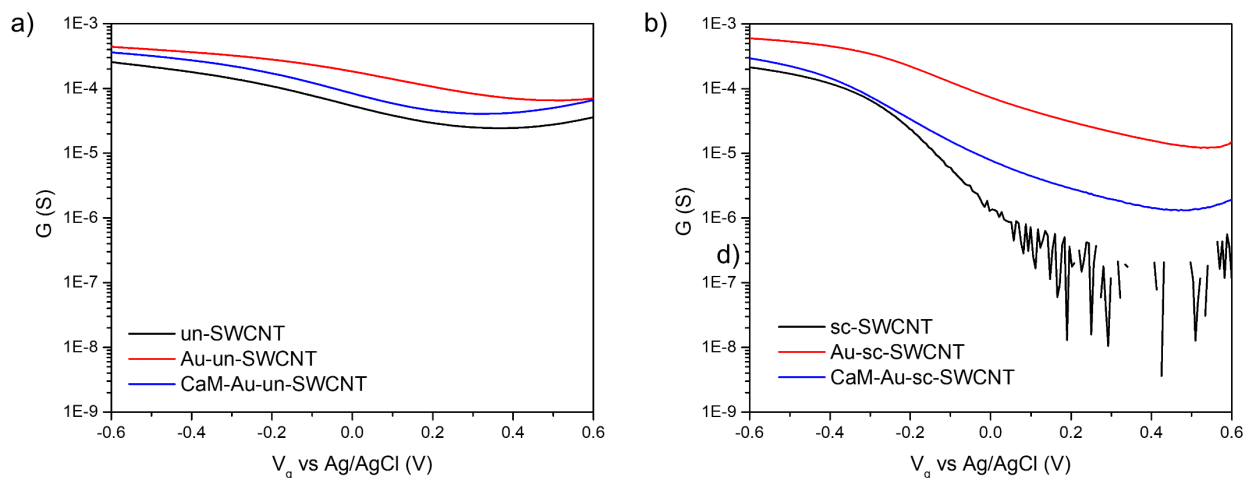
Appendix Figure A-6 Device reproducibility of un-SWCNT and sc-SWCNT FET devices. (a) Calibration plot for un-SWCNT FET devices. (b) Calibration plot for sc-SWCNTs devices. Both calibration curves were constructed by plotting the averaged relative conductance changes from multiple devices at $-0.5 V_g$ against concentrations of Ca^{2+} solution. Error bars were calculated from 4 different devices for un-SWCNT devices, and 5 different devices for sc-SWCNT devices. The larger error bars for sc-SWCNT devices suggest larger device-to-device variations for sc-SWCNT devices.



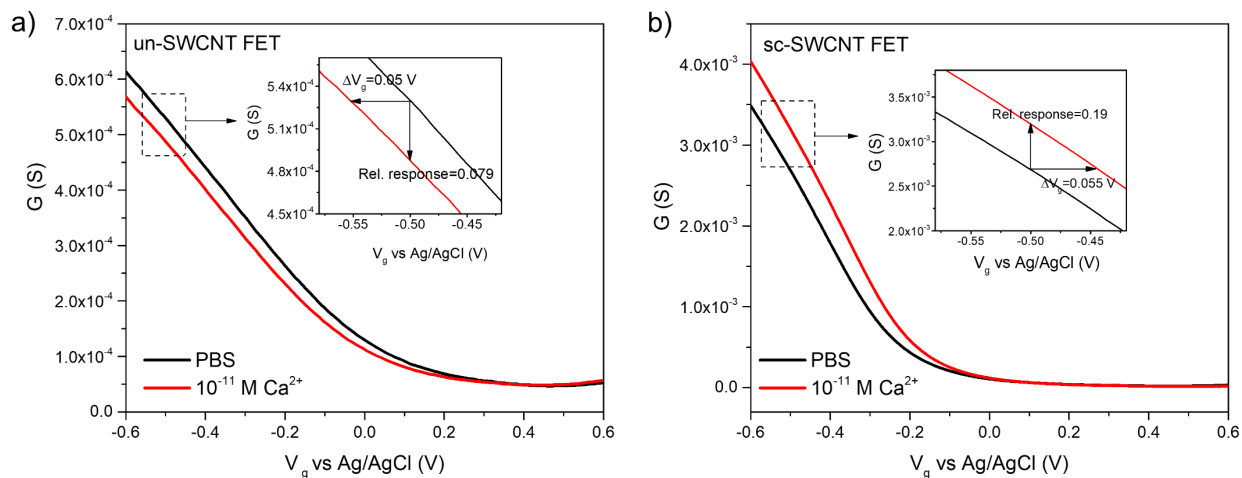
Appendix Figure A-7 Control experiments with un-SWCNT and sc-SWCNT FET devices. (a) SEM image of CaM on un-SWCNT networks. (b) SEM image of CaM on sc-SWCNT networks. (c) Calibration plot of the active system and control systems of un-SWCNT FET devices. (d) Calibration plot of the active system and control systems of sc-SWCNT FET devices in the corresponding linear range.



Appendix Figure A-8 Comparison of source-drain current (I_d) and gate leakage current (I_g) for sc-SWCNT and un-SWCNT FET devices. For both (a) sc-SWCNT and (b) un-SWCNT FET devices, the gate current is insignificant compared to the source-drain current, therefore the effect of leakage current is negligible.



Appendix Figure A-9 Comparison of on/off ratio of un-SWCNT and sc-SWCNT FET devices. (a) FET characteristic curves of CaM-Au-un-SWCNT FET device during each step of functionalization plotting in logarithmic scale. (b) FET characteristic curves of CaM-Au-sc-SWCNT FET device during each step of functionalization plotting in logarithmic scale. The on/off ratio of un-SWCNT FET device was ~ 3 , while the on/off ratio of sc-SWCNT FET device was $\sim 10^4$. sc-SWCNT FET devices show better on/off ratio due to the lack of metallic carbon nanotubes, therefore efficiently turning off the device.



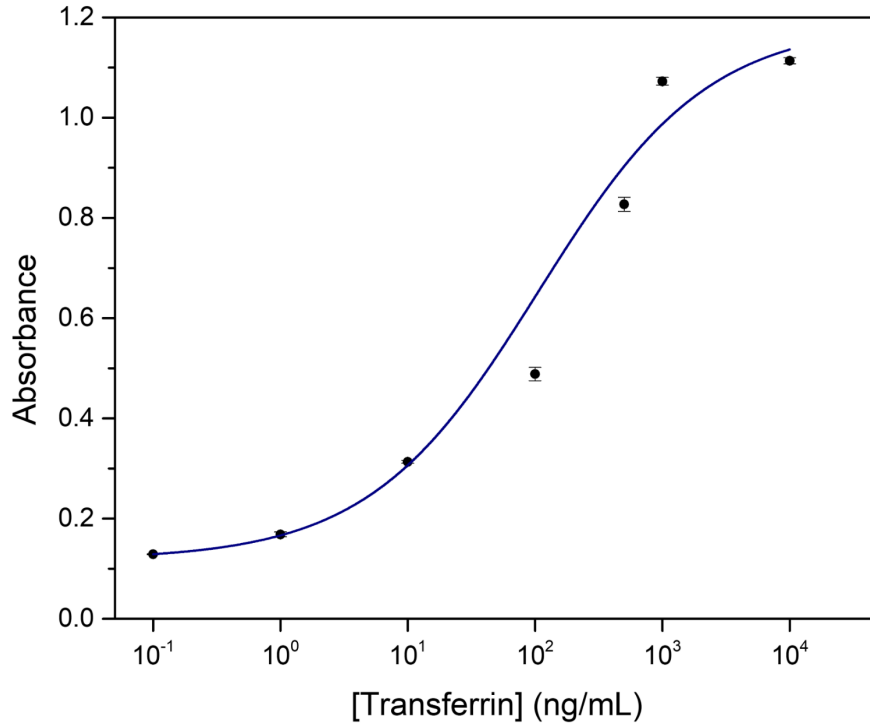
Appendix Figure A-10 Comparison of calibration sensitivity of un-SWCNT and sc-SWCNT FET devices.

Absolute relative response of (a) CaM-Au-un-SWCNT FET device and (b) CaM-Au-sc-SWCNT FET device to 10^{-11} M Ca^{2+} . With higher on/off ratio, sc-SWCNT FET device had a significant higher absolute relative response than un-SWCNT FET device, even though the shift of gate voltage was similar.

Appendix Table A-1 Comparison of various methods for Ca²⁺ detection

Ca ²⁺ detection method	Ca ²⁺ detection limit	Reference
Ca ²⁺ selective PVC-membrane electrode	7.5×10^{-7} M	164
Solid-contact Ca ²⁺ selective electrode	$(3.4-8.2) \times 10^{-6}$ M	165
NiCo ₂ O ₄ /3-D Graphene	0.38 μ M	166
Fluorescent carbon quantum dot	77 pM (in human serum)	167
CaM-Au-sc-SWCNT FET	10^{-15} M	This work

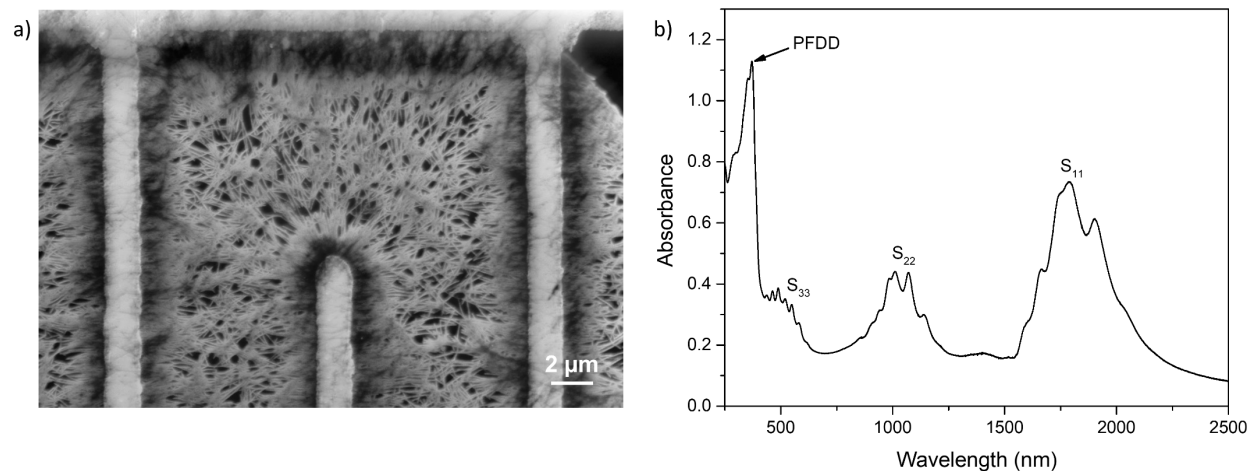
Appendix B Chapter 3 Supporting Information



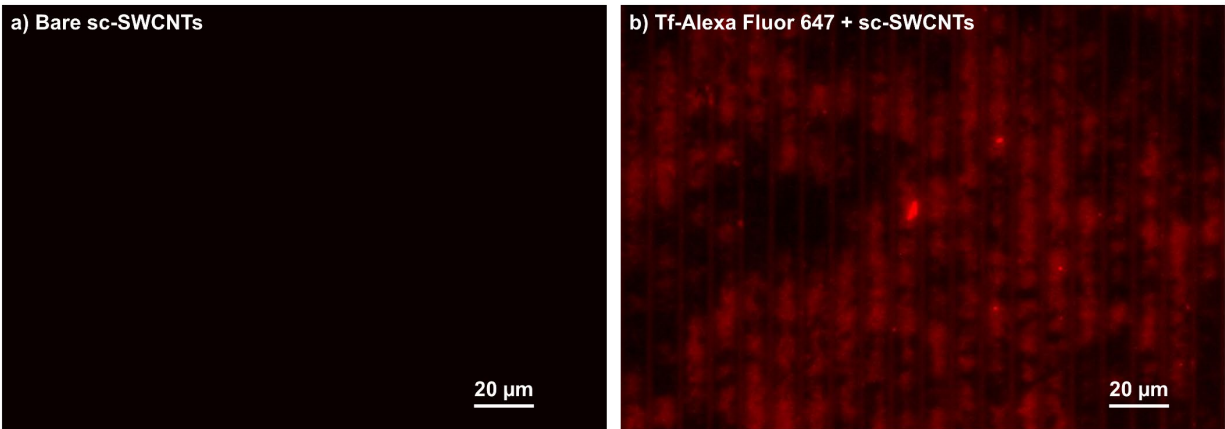
Appendix Figure B-1 Transferrin ELISA standard curve. All data points are Mean \pm SD ($n=2$).

Appendix Table B-1 Transferrin concentration of positive and negative sample after 2 steps of separation determined from the standard curve. (n is the number of samples tested.)

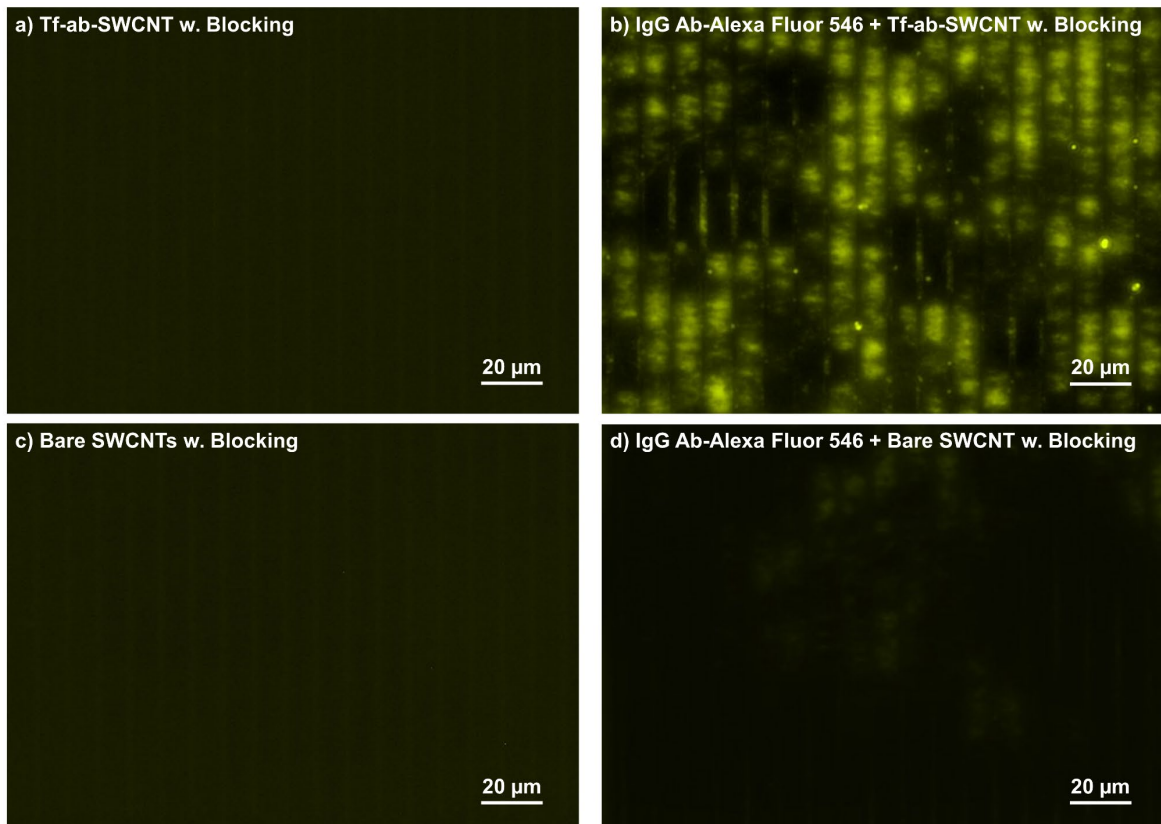
Sample	Absorbance	Transferrin concentration
Positive ($n = 2$)	0.15 \pm 0.02	0.46 ng/mL
Negative ($n = 2$)	0.0217 \pm 0.0006	0 ng/mL
Blank ($n = 5$)	0.021 \pm 0.001	0 ng/mL



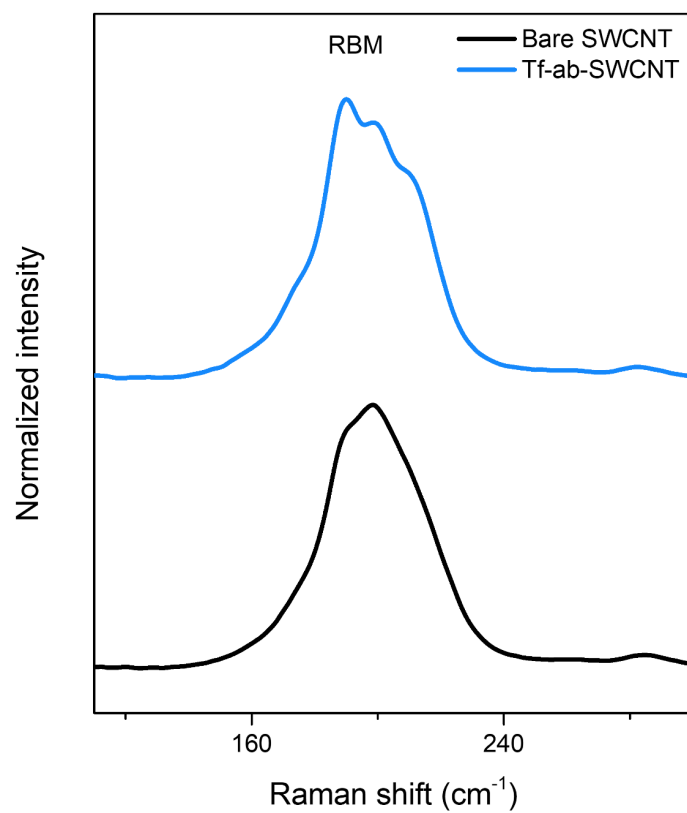
Appendix Figure B-2 Characterizations of high-purity semiconducting single-walled carbon nanotubes. (a) Scanning electron microscopy (SEM) image of sc-SWCNT deposited on a FET device, forming dense and interconnected networks. (b) UV-vis-NIR spectrum of sc-SWCNT. The S₁₁, S₂₂ and S₃₃ peaks are characteristic of the semiconducting SWCNTs. The absence of M₁₁ peak confirms the high-purity semiconducting content of sc-SWCNT samples. The polyfluorene-dodecyl (PFDD) peak appeared at 392nm corresponds to the polymer coating on sc-SWCNT during sorting process.



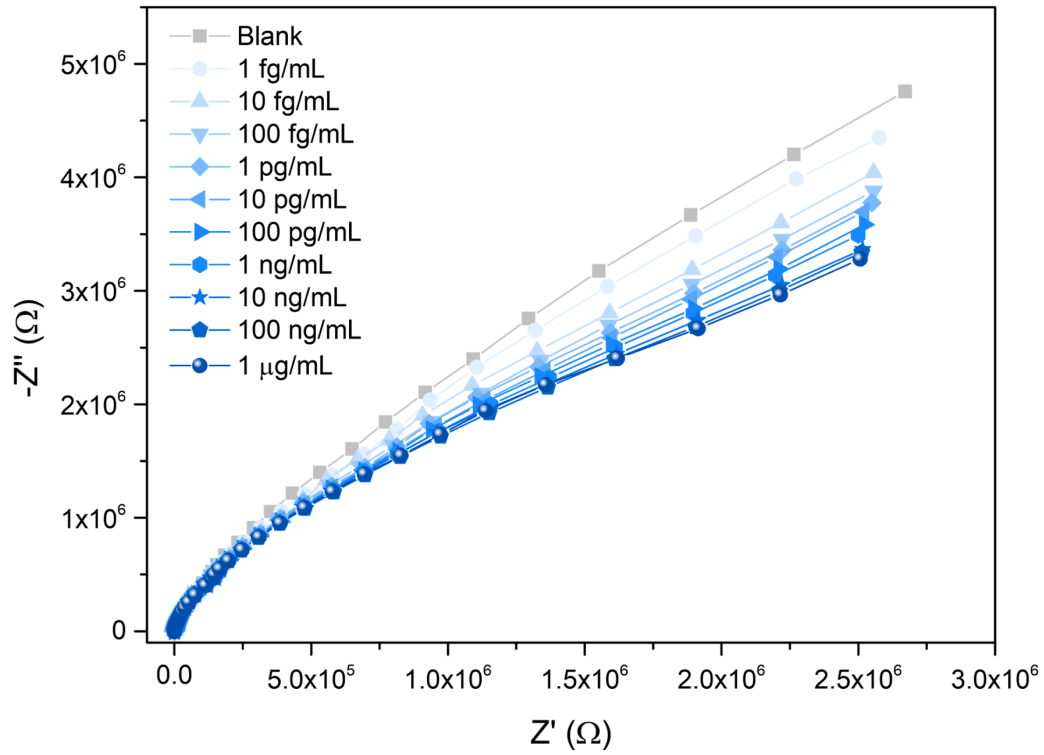
Appendix Figure B-3 Nonspecific binding of Alexa Fluor 647 conjugated transferrin on bare sc-SWCNTs. (a- b) Fluorescent image of sc-SWCNT FET device (a) before and (b) after Alexa Fluor 647 conjugated transferrin binding. Red fluorescence was observable after adding Alexa Fluor 647 conjugated transferrin, indicating the absorbing of transferrin on bare sc-SWCNTs.



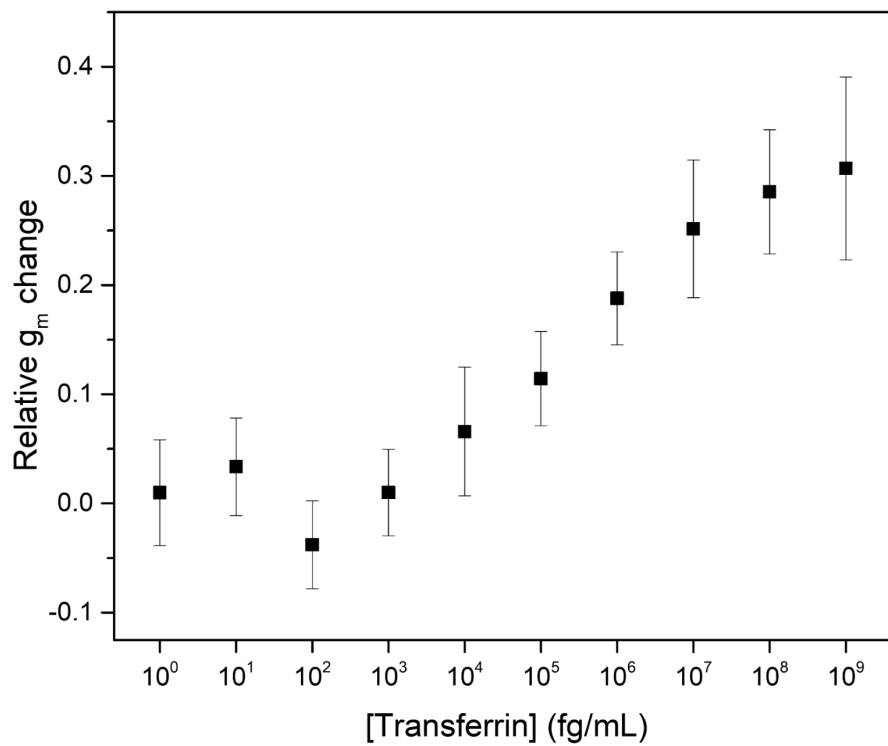
Appendix Figure B-4 Fluorescence characterization of Tf-ab functionalized sc-SWCNT FET device. (a-b) Fluorescence images of Tf-ab functionalized sc-SWCNT FET device (a) before and (b) after Alexa Fluor 546 conjugated anti-IgG antibody binding. (c-d) Fluorescence images of a blocked bare sc-SWCNT FET device (c) before and (d) after Alexa Fluor 546 conjugated anti-IgG antibody binding. Fluorescence was observable when the secondary antibody was added to Tf-ab functionalized device but not on blocked sc-SWCNT device without Tf-ab, indicating the successful functionalization of Tf-ab on the sc-SWCNT surface.



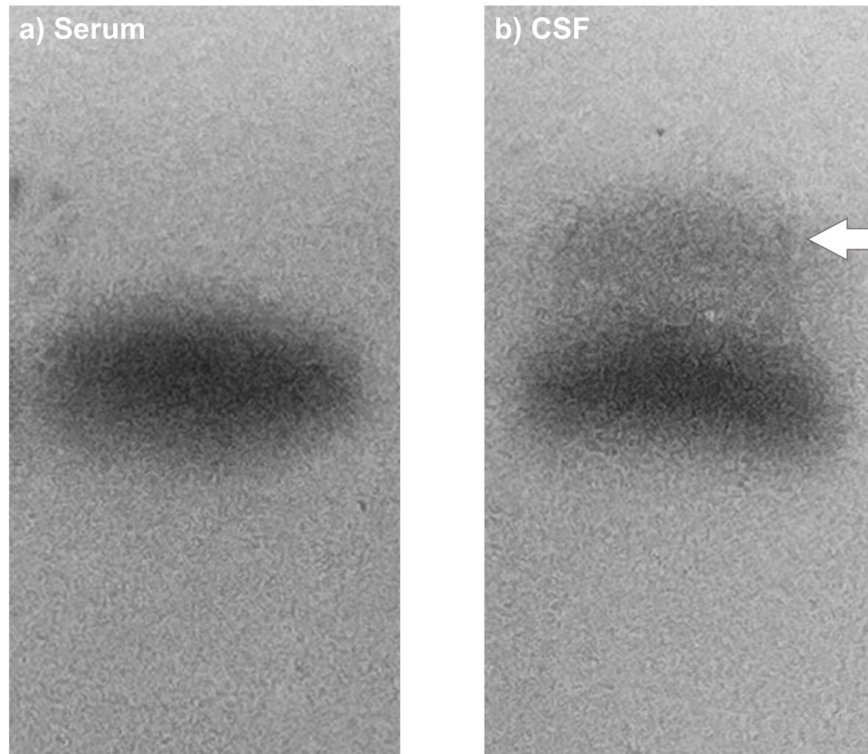
Appendix Figure B-5 RBM region of Raman spectra of sc-SWCNTs before (black) and after (blue) Tf-ab functionalization. All spectra were normalized to Si peak at 502 cm⁻¹. A split of RBM peak was observed after the immobilization of Tf-ab, and the peak at higher wavenumber decreased in intensity, suggesting a diameter dependent functionalization of Tf-ab on sc-SWCNTs.



Appendix Figure B-6 Nyquist plot for EIS measurement of the gold disk surface upon exposing to increasing concentrations of transferrin.



Appendix Figure B-7 Relative transconductance change of sc-SWCNT FET devices for transferrin sensing using the Au electrode approach.

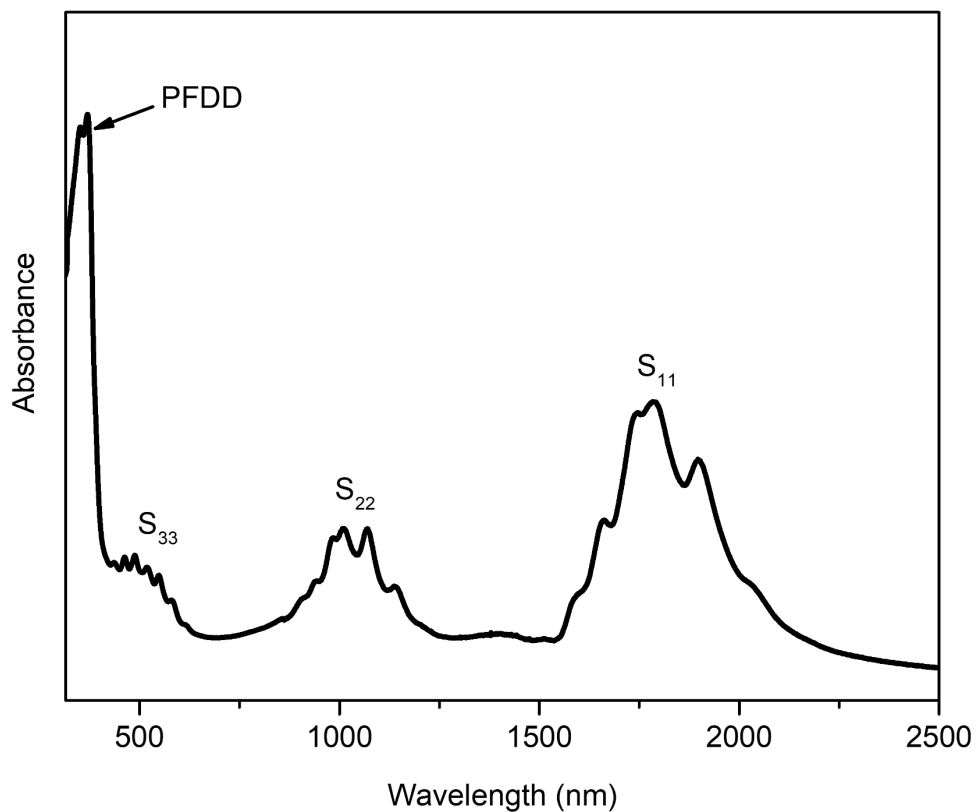


Appendix Figure B-8 Western blot of Serum and CSF. (a) Serum sample, as the negative control, yielded only 1 transferrin band due to the lack of β 2-Tf. (b) CSF yielded 2 transferrin bands with the leading band (indicated by the arrow) representing β 2-Tf.

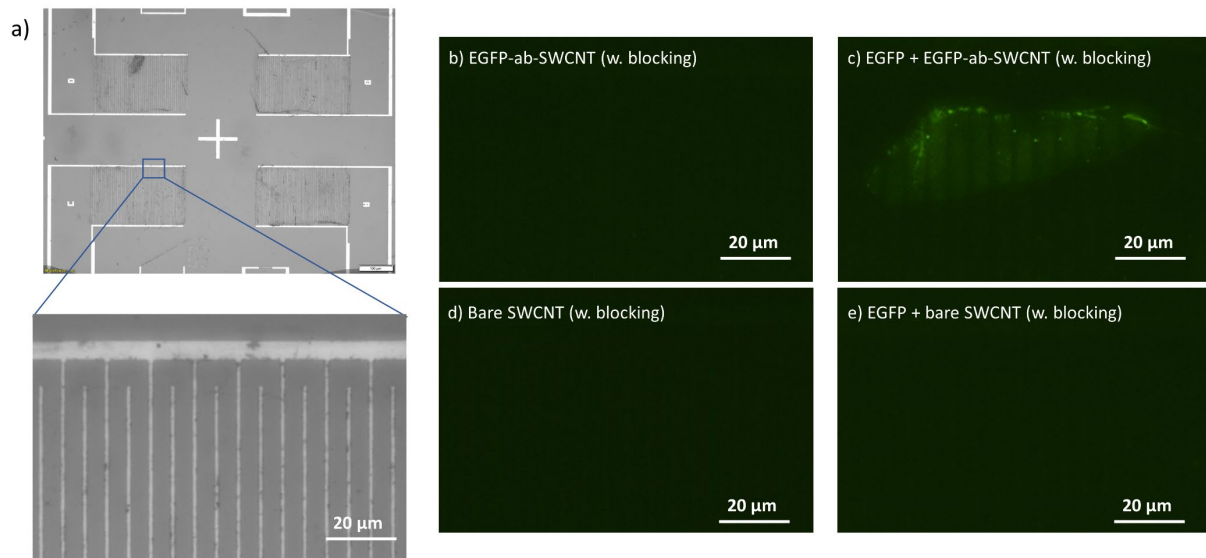
Appendix Table B-2 Relative response of each body fluid sample tested with sc-SWCNT FET devices using Tf-ab-SWCNT and Au electrode approach.

Samples	Tf-ab-SWCNT			Au electrode		
	Average	SD	# of dev.	Average	SD	# of dev.
CSF1	0.383	0.041106	n = 4	0.107	0.015359	n = 4
CSF2	0.302	0	n = 1	0.0806	0	n = 1
CSF3	0.196	0.066343	n = 2	0.0505	0.018261	n = 3
CSF4	0.274	0.001462	n = 2	0.140	0.030117	n = 4
Serum1	0.000436	0.008957	n = 3	0.00194	0.010033	n = 4
Serum2	0.004995	0.013606	n = 3	-0.0139	0.013089	n = 3
Serum3	-0.00271	0.011827	n = 3	-0.000547	0.00018	n = 2
Serum4	0.018587	0.008431	n = 3	0.00713	0.00458	n = 2

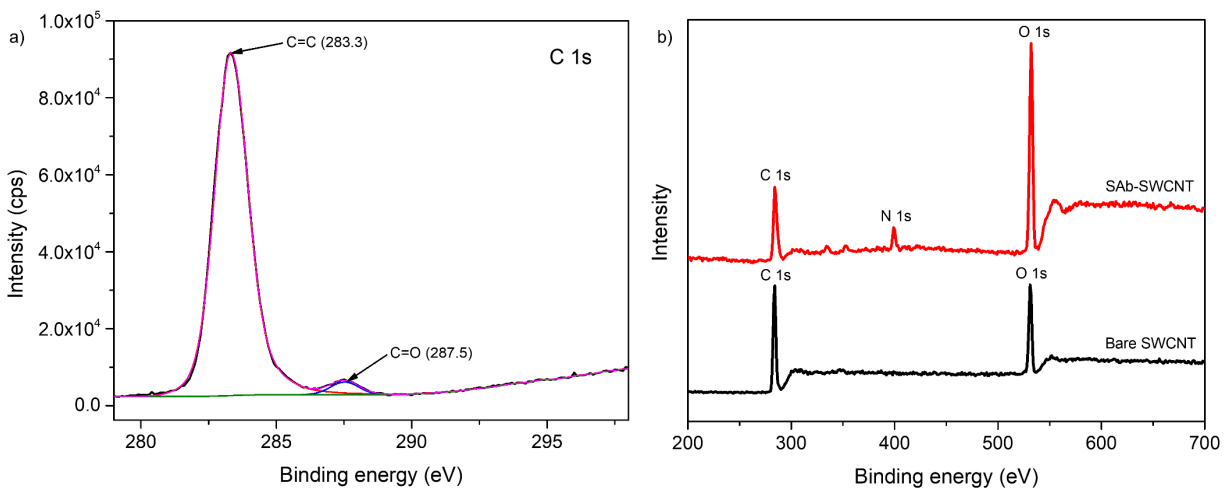
Appendix C Chapter 4 Supporting Information



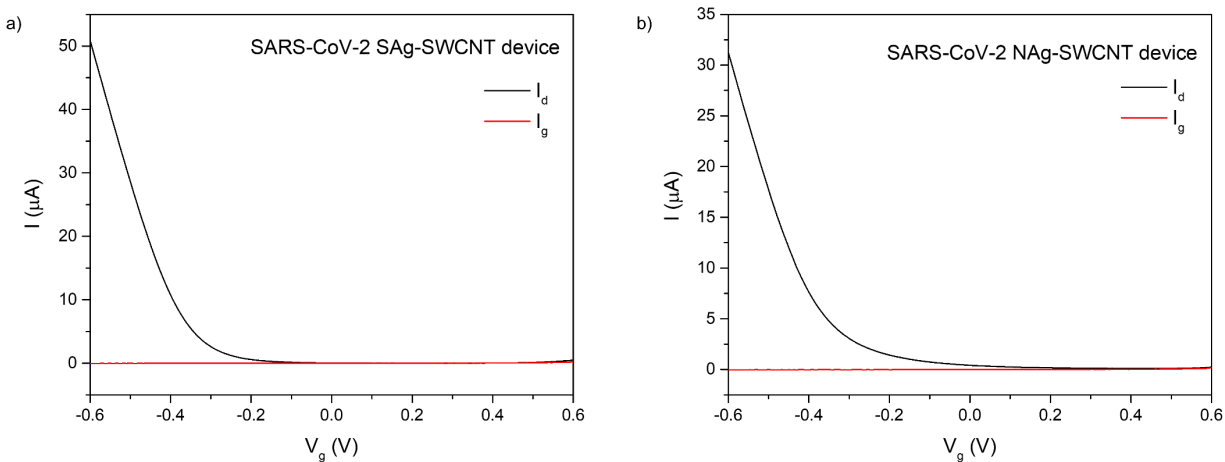
Appendix Figure C-1 UV-vis-NIR spectrum of sc-SWCNT. The S₁₁, S₂₂ and S₃₃ peaks are characteristic of the semiconducting SWCNTs. The absence of M₁₁ peak further confirms the high-purity semiconducting content of sc-SWCNT samples. The sharp peak at 392 nm can be attributed to polyfluorene-dodecyl (PFDD) polymer coating on sc-SWCNT due to the commercial sorting process.



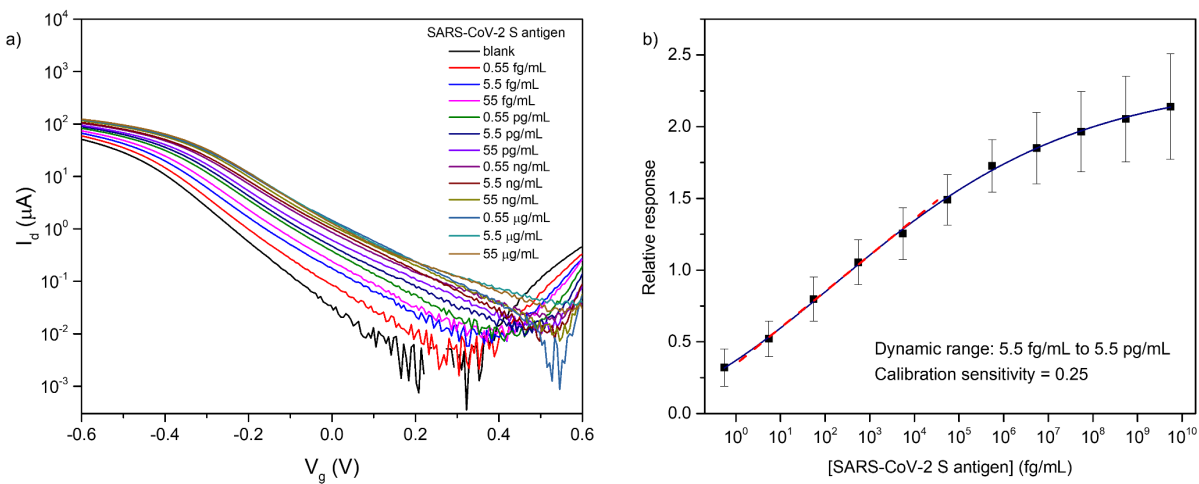
Appendix Figure C-2 Functionalization of enhanced green fluorescent protein (EGFP) antibody on a SWCNT FET device. (a) Top: Microscopic image of the 4-device FET biosensing chip. (Scale bar: 200 μm) Bottom: Zoomed in image shows the area where fluorescence images were taken. (b-c) Fluorescence images of EGFP antibody functionalized SWCNT FET device (b) before and (c) after EGFP binding. (d-e) Fluorescence images of a blocked bare SWCNT FET device (d) before and (e) after EGFP binding. Green fluorescence was observable when EGFP was added to EGFP antibody functionalized device but not on bare SWCNTs without EGFP antibody, indicating the successful functionalization of EGFP antibody on the SWCNT surface.



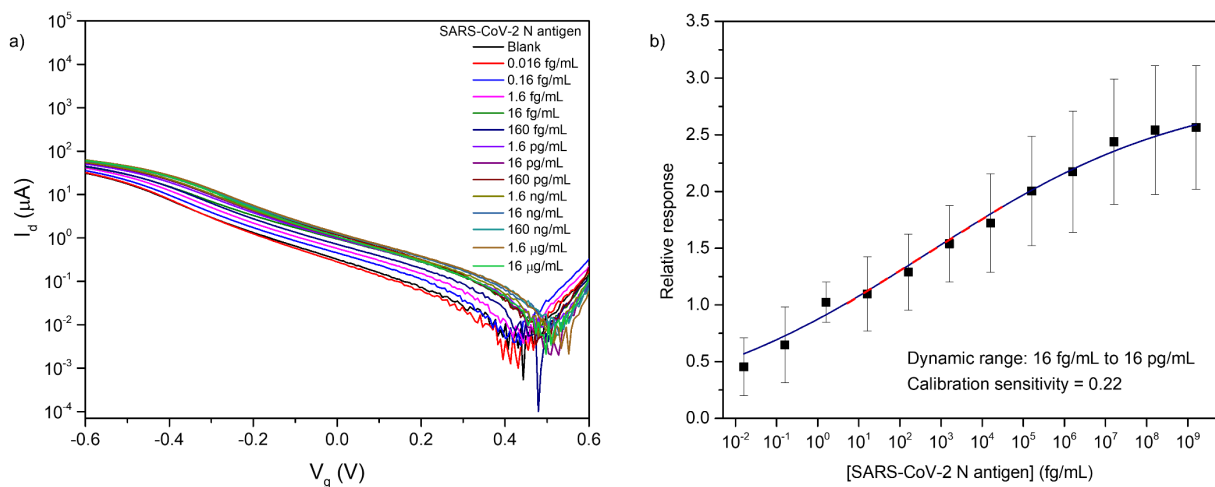
Appendix Figure C-3 XPS spectra of sc-SWCNT FET devices. (a) High resolution C 1s XPS spectrum of sc-SWCNT. The deconvoluted C 1s spectrum indicated the presence of C=C (283.3 eV) and C=O (287.5 eV), thus confirming the presence of COOH functional groups on sc-SWCNT. (b) XPS survey of sc-SWCNT device before and after SAb functionalization. N 1s peak appeared after SAb functionalization, and the atomic percent of N increased from 0% to 5%, suggesting the successful immobilization of SAb on SWCNTs.



Appendix Figure C-4 Comparison of source-drain current (I_d) and gate leakage current (I_g) of SAb-SWCNT FET device and NAb-SWCNT FET device. (a) I_d and I_g for SAb-SWCNT FET device. (b) I_d and I_g for NAb-SWCNT FET device. The effect of leakage current is negligible as I_g is insignificant compared to I_d .



Appendix Figure C-5 FET characteristic curves and calibration curve of S antigen detection using S antibody functionalized FET devices. (a) I_d - V_g curves of the SAb-SWCNT FET device showed shift of the threshold voltage towards the more positive region with increasing concentration of SAg. (b) The calibration curve was fit using a five-parameter logistic model. The dynamic range was indicated by the dashed red line. The calibration sensitivity, defined as the slope of the linear region of the calibration curve, was determined to be 0.25.



Appendix Figure C-6 FET characteristic curves and calibration curve of N antigen detection using N antibody functionalized FET devices. (a) I_d - V_g curves of the NAb-SWCNT FET device showed shift of the threshold voltage towards the more positive region with increasing concentration of NAg. (b) The calibration curve was fit using a five-parameter logistic model. The dynamic range was indicated by the dashed red line. The calibration sensitivity, defined as the slope of the linear region of the calibration curve, was determined to be 0.22.

Appendix Table C-1 Number of devices (n) tested for each clinical sample.

Sample	S antibody functionalized FET device	N antibody functionalized FET device
Positive 1	n = 4	n = 3
Positive 2	n = 3	n = 3
Positive 3	n = 4	n = 3
Positive 4	n = 3	n = 4
Positive 5	n = 4	n = 3
Positive 6	n = 3	n = 2
Positive 8	n = 2	n = 3
Positive 9	n = 1	n = 4
Positive 10	n = 4	n = 4
Positive 12	n = 4	n = 3
Positive 13	n = 3	n = 3
Positive 14	n = 4	n = 4
Positive 15	n = 2	n = 2
Positive 16	n = 1	n = 3
Positive 17	n = 3	n = 3
Positive 18	n = 2	n = 3
Positive 19	n = 4	n = 3
Positive 20	n = 3	n = 3
Positive 21	n = 3	n = 2
Positive 22	n = 2	n = 4

Positive 23	n = 3	n = 2
Positive 24	n = 3	n = 3
Positive 25	n = 3	n = 2
Positive 26	n = 1	n = 3
Positive 27	n = 4	n = 4
Positive 28	n = 4	n = 3
Positive 29	n = 3	n = 4
Positive 30	n = 2	n = 3
Negative 1	n = 2	n = 4
Negative 2	n = 3	n = 4
Negative 3	n = 3	n = 2
Negative 4	n = 3	n = 3
Negative 5	n = 3	n = 1
Negative 6	n = 3	n = 2
Negative 7	n = 2	n = 2
Negative 8	n = 3	n = 2
Negative 9	n = 3	n = 2
Negative 10	n = 4	n = 3

Appendix D List of Publications during PhD Study

- (1) Zeng, Z.; Sorescu, D. C.; White, D. L.; Hwang, S. I.; Shao, W.; He, X.; Schulte, Z. M.; Rosi, N. L.; Star, A. Heterogeneous Growth of UiO-66-NH₂ on Oxidized Single-Walled Carbon Nanotubes to Form “Beads-on-a-String” Composites, *ACS Appl. Mater. Interfaces*, **2021**, DOI: 10.1021/acsami.0c21509.
- (2) Shao, W.; Shurin, M. R.; Wheeler, S. E.; He, X.; Star, A., Rapid Detection of SARS-CoV-2 Antigens Using High-Purity Semiconducting Single-Walled Carbon Nanotube-Based Field-Effect Transistors. *ACS Appl. Mater. Interfaces* **2021**, *13*, 10321–10327.
- (3) Shao, W.; Burkert, S. C.; White, D. L.; Scott, V. L.; Ding, J.; Li, Z.; Ouyang, J.; Lapointe, F.; Malenfant, P. R. L.; Islam, K.; Star, A., Probing Ca²⁺-Induced Conformational Change of Calmodulin with Gold Nanoparticle-Decorated Single-Walled Carbon Nanotube Field-Effect Transistors. *Nanoscale* **2019**, *11*, 13397–13406.
- (4) Mukherjee, S. P.; Gliga, A. R.; Lazzaretto, B.; Brandner, B.; Fielden, M.; Vogt, C.; Newman, L.; Rodrigues, A. F.; Shao, W.; Fournier, P. M.; Toprak, M. S.; Star, A.; Kostarelos, K.; Bhattacharya K.; Fadeel, B. Graphene Oxide is Degraded by Neutrophils and the Degradation Products are Non-genotoxic, *Nanoscale*, **2018**, *10*, 1180–1188.
- (5) Michael, Z. P.; Shao, W.; Sorescu, D. C.; Euler, R. W.; Burkert, S. C.; Star, A., Probing Biomolecular Interactions with Gold Nanoparticle-Decorated Single-Walled Carbon Nanotubes. *J. Phys. Chem. C* **2017**, *121*, 20813–20820.
- (6) Seo, W.; Carpenter, K. L.; Gaugler, J. A.; Shao, W.; Werling, K. A.; Fournier, P. M.; Lambrecht, D. A.; Star, A. Polybenzobisimidazole-Derived Two-Dimensional Supramolecular Polymer, *J. Polym. Sci. A Polym. Chem.*, **2017**, *55*, 1095–1101.

Bibliography

- (1) Srinivas, P. R.; Kramer, B. S.; Srivastava, S., Trends in Biomarker Research for Cancer Detection. *Lancet Oncol.* **2001**, *2*, 698–704.
- (2) Pourhassan-Moghaddam, M.; Rahmati-Yamchi, M.; Akbarzadeh, A.; Daraee, H.; Nejati-Koshki, K.; Hanifehpour, Y.; Joo, S. W., Protein Detection Through Different Platforms of Immuno-Loop-Mediated Isothermal Amplification. *Nanoscale Res. Lett.* **2013**, *8*, 485.
- (3) Ray, P.; Le Manach, Y.; Riou, B.; Houle, T. T., Statistical Evaluation of a Biomarker. *Anesthesiology* **2010**, *112*, 1023–1040.
- (4) Sawyers, C. L., The Cancer Biomarker Problem. *Nature* **2008**, *452*, 548–552.
- (5) Khanmohammadi, A.; Aghaie, A.; Vahedi, E.; Qazvini, A.; Ghanei, M.; Afkhami, A.; Hajian, A.; Bagheri, H., Electrochemical Biosensors for the Detection of Lung Cancer Biomarkers: A Review. *Talanta* **2020**, *206*, 120251.
- (6) Wu, L.; Qu, X., Cancer Biomarker Detection: Recent Achievements and Challenges. *Chem. Soc. Rev.* **2015**, *44*, 2963–2997.
- (7) Crosby, D.; Lyons, N.; Greenwood, E.; Harrison, S.; Hiom, S.; Moffat, J.; Quallo, T.; Samuel, E.; Walker, I., A Roadmap for the Early Detection and Diagnosis of Cancer. *Lancet Oncol.* **2020**, *21*, 1397–1399.
- (8) Li, J.; Li, S.; Yang, C. F., Electrochemical Biosensors for Cancer Biomarker Detection. *Electroanalysis* **2012**, *24*, 2213–2229.
- (9) Senf, B.; Yeo, W. H.; Kim, J. H., Recent Advances in Portable Biosensors for Biomarker Detection in Body Fluids. *Biosensors* **2020**, *10*, 127.
- (10) Suntornsuk, W.; Suntornsuk, L., Recent Applications of Paper-Based Point-of-Care Devices for Biomarker Detection. *Electrophoresis* **2020**, *41*, 287–305.
- (11) Mahmoudi, T.; de la Guardia, M.; Baradaran, B., Lateral Flow Assays Towards Point-of-Care Cancer Detection: A Review of Current Progress and Future Trends. *Trends Anal. Chem.* **2020**, *125*, 115842.
- (12) Shao, B.; Xiao, Z., Recent Achievements in Exosomal Biomarkers Detection by Nanomaterials-Based Optical Biosensors - A Review. *Anal. Chim. Acta* **2020**, *1114*, 74–84.
- (13) Blennow, K.; Zetterberg, H., Biomarkers for Alzheimer's Disease: Current Status and Prospects for the Future. *J. Intern. Med.* **2018**, *284*, 643–663.

- (14) Parnetti, L.; Gaetani, L.; Eusebi, P.; Paciotti, S.; Hansson, O.; El-Agnaf, O.; Mollenhauer, B.; Blennow, K.; Calabresi, P., CSF and Blood Biomarkers for Parkinson's Disease. *Lancet Neurol.* **2019**, *18*, 573–586.
- (15) Qureshi, A.; Gurbuz, Y.; Niazi, J. H., Biosensors for Cardiac Biomarkers Detection: A Review. *Sens. Actuators B Chem.* **2012**, *171–172*, 62–76.
- (16) Gao, G. F., For a Better World: Biosafety Strategies to Protect Global Health. *Biosaf. Health* **2019**, *1*, 1–3.
- (17) Ward, M. D.; Kenny, T.; Bruggeman, E.; Kane, C. D.; Morrell, C. L.; Kane, M. M.; Bixler, S.; Grady, S. L.; Quizon, R. S.; Astatke, M.; Cazares, L. H., Early Detection of Ebola Virus Proteins in Peripheral Blood Mononuclear Cells From Infected Mice. *Clin. Proteom.* **2020**, *17*, 11.
- (18) Ferdin, J.; Goricar, K.; Dolzan, V.; Plemenitas, A.; Martin, J. N.; Peterlin, B. M.; Deeks, S. G.; Lenassi, M., Viral Protein Nef is Detected in Plasma of Half of HIV-Infected Adults with Undetectable Plasma HIV RNA. *PLoS One* **2018**, *13*, e0191613.
- (19) Li, Y. H.; Li, J.; Liu, X. E.; Wang, L.; Li, T.; Zhou, Y. H.; Zhuang, H., Detection of the Nucleocapsid Protein of Severe Acute Respiratory Syndrome Coronavirus in Serum: Comparison with Results of Other Viral Markers. *J. Virol. Methods* **2005**, *130*, 45–50.
- (20) Anderson, M. R.; Pleet, M. L.; Enose-Akahata, Y.; Erickson, J.; Monaco, M. C.; Akpamagbo, Y.; Velluci, A.; Tanaka, Y.; Azodi, S.; Lepene, B.; Jones, J.; Kashanchi, F.; Jacobson, S., Viral Antigens Detectable in Csf Exosomes From Patients with Retrovirus Associated Neurologic Disease: Functional Role of Exosomes. *Clin. Transl. Med.* **2018**, *7*, 24.
- (21) Centers for Disease Control and Prevention. Interim Guidance for Antigen Testing for SARS-CoV-2. <https://www.cdc.gov/coronavirus/2019-ncov/lab/resources/antigen-tests-guidelines.html> (accessed March 13, 2021).
- (22) U.S. Food and Drug Administration. FDA Allows Marketing of First Rapid Diagnostic Test for Detecting Ebola Virus Antigens. <https://www.fda.gov/news-events/press-announcements/fda-allows-marketing-first-rapid-diagnostic-test-detecting-ebola-virus-antigens> (accessed March 13, 2021).
- (23) Diederens, B. M. W.; Veenendaal, D.; Jansen, R.; Herpers, B. L.; Ligtvoet, E. E. J.; IJzerman, E. P. F., Rapid Antigen Test for Pandemic (H1N1) 2009 Virus. *Emerg. Infect. Dis.* **2010**, *16*, 897–898.
- (24) Louie, J. K.; Guevara, H.; Boston, E.; Dahlke, M.; Nevarez, M.; Kong, T.; Schechter, R.; Glaser, C. A.; Schnurr, D. P., Rapid Influenza Antigen Test for Diagnosis of Pandemic (H1N1) 2009. *Emerg. Infect. Dis.* **2010**, *16*, 824–826.

- (25) Mak, G. C.; Cheng, P. K.; Lau, S. S.; Wong, K. K.; Lau, C. S.; Lam, E. T.; Chan, R. C.; Tsang, D. N., Evaluation of Rapid Antigen Test for Detection of SARS-CoV-2 Virus. *J. Clin. Virol.* **2020**, *129*, 104500.
- (26) Mak, G. C. K.; Lau, S. S. Y.; Wong, K. K. Y.; Chow, N. L. S.; Lau, C. S.; Lam, E. T. K.; Chan, R. C. W.; Tsang, D. N. C., Evaluation of Rapid Antigen Detection Kit From the WHO Emergency Use List for Detecting SARS-CoV-2. *J. Clin. Virol.* **2021**, *134*, 104712.
- (27) Alemany, A.; Baro, B.; Ouchi, D.; Rodo, P.; Ubals, M.; Corbacho-Monne, M.; Vergara-Alert, J.; Rodon, J.; Segales, J.; Esteban, C.; Fernandez, G.; Ruiz, L.; Bassat, Q.; Clotet, B.; Ara, J.; Vall-Mayans, M.; C, G. B.; Mitja, O., Analytical and Clinical Performance of the Panbio COVID-19 Antigen-Selecting Rapid Diagnostic Test. *J. Infect.* **2021**, *In press*.
- (28) Darwish, I. A., Immunoassay Methods and their Applications in Pharmaceutical Analysis: Basic Methodology and Recent Advances. *Int. J. Biomed. Sci.* **2006**, *2*, 217–235.
- (29) Wu, L.; Li, G.; Xu, X.; Zhu, L.; Huang, R.; Chen, X., Application of Nano-ELISA in Food Analysis: Recent Advances and Challenges. *Trends Anal. Chem.* **2019**, *113*, 140–156.
- (30) Leva-Bueno, J.; Peyman, S. A.; Millner, P. A., A Review on Impedimetric Immunosensors for Pathogen and Biomarker Detection. *Med. Microbiol. Immunol.* **2020**, *209*, 343–362.
- (31) ThermoFisher Scientific. Overview of ELISA. <https://www.thermofisher.com/us/en/home/life-science/protein-biology/protein-biology-learning-center/protein-biology-resource-library/pierce-protein-methods/overview-elisa.html> (accessed March 13, 2021).
- (32) Zhao, L. J.; Yu, R. J.; Ma, W.; Han, H. X.; Tian, H.; Qian, R. C.; Long, Y. T., Sensitive Detection of Protein Biomarkers using Silver Nanoparticles Enhanced Immunofluorescence Assay. *Theranostics* **2017**, *7*, 876–883.
- (33) Wang, Y.-W.; Chen, L.; Liang, M.; Xu, H.; Tang, S.; Yang, H.-H.; Song, H., Sensitive Fluorescence Immunoassay of Alpha-Fetoprotein Through Copper Ions Modulated Growth of Quantum Dots In-Situ. *Sens. Actuators B Chem.* **2017**, *247*, 408–413.
- (34) Lin, Q.; Wu, J.; Fang, X.; Kong, J., Washing-Free Centrifugal Microchip Fluorescence Immunoassay for Rapid and Point-of-Care Detection of Protein. *Anal. Chim. Acta* **2020**, *1118*, 18–25.
- (35) Cinquanta, L.; Fontana, D. E.; Bizzaro, N., Chemiluminescent Immunoassay Technology: What Does It Change in Autoantibody Detection? *Auto Immun. Highlights* **2017**, *8*, 9.
- (36) Ji, T.; Liu, Z.; Wang, G.; Guo, X.; Akbar Khan, S.; Lai, C.; Chen, H.; Huang, S.; Xia, S.; Chen, B.; Jia, H.; Chen, Y.; Zhou, Q., Detection of COVID-19: A Review of the Current Literature and Future Perspectives. *Biosens. Bioelectron.* **2020**, *166*, 112455.
- (37) Bishop, J. D.; Hsieh, H. V.; Gasperino, D. J.; Weigl, B. H., Sensitivity Enhancement in Lateral Flow Assays: A Systems Perspective. *Lab Chip* **2019**, *19*, 2486–2499.

- (38) Mashayekhi, F.; Le, A. M.; Nafisi, P. M.; Wu, B. M.; Kamei, D. T., Enhancing the Lateral-Flow Immunoassay for Detection of Proteins using an Aqueous Two-Phase Micellar System. *Anal. Bioanal. Chem.* **2012**, *404*, 2057–2066.
- (39) Shen, M.; Li, N.; Lu, Y.; Cheng, J.; Xu, Y., An Enhanced Centrifugation-Assisted Lateral Flow Immunoassay for the Point-of-Care Detection of Protein Biomarkers. *Lab Chip* **2020**, *20*, 2626–2634.
- (40) Lin, W. Z.; Ma, I. C.; Wang, J. P.; Hsieh, P. C.; Liu, C. C.; Hou, S. Y., Highly Sensitive Protein Detection using Recombinant Spores and Lateral Flow Immunoassay. *Anal. Bioanal. Chem.* **2021**, *413*, 2235–2246.
- (41) Baldwin, M. A., Protein Identification by Mass Spectrometry: Issues to be Considered. *Mol. Cell. Proteom.* **2004**, *3*, 1–9.
- (42) Wang, P.; Wilson, S. R., Mass Spectrometry-Based Protein Identification by Integrating De Novo Sequencing with Database Searching. *BMC Bioinformatics* **2013**, *14*(Suppl 2), S24.
- (43) Domon, B.; Aebersold, R., Mass Spectrometry and Protein Analysis. *Science* **2006**, *312*, 212–217.
- (44) Lin, D.; Tabb, D. L.; Yates, J. R., Large-Scale Protein Identification using Mass Spectrometry. *Biochim. Biophys. Acta Proteins Proteom.* **2003**, *1646*, 1–10.
- (45) Zhang, C.; Glaros, T.; Manicke, N. E., Targeted Protein Detection Using an All-in-One Mass Spectrometry Cartridge. *J. Am. Chem. Soc.* **2017**, *139*, 10996–10999.
- (46) Luo, X.; Davis, J. J., Electrical Biosensors and the Label Free Detection of Protein Disease Biomarkers. *Chem. Soc. Rev.* **2013**, *42*, 5944–5962.
- (47) Zhao, W.; Xu, J.; Chen, H., Photoelectrochemical DNA Biosensors. *Chem. Rev.* **2014**, *114*, 7421–7441.
- (48) Zhou, Q.; Son, K.; Liu, Y.; Revzin, A., Biosensors for Cell Analysis. *Annu. Rev. Biomed. Eng.* **2015**, *17*, 165–190.
- (49) Haes, A. J.; Duyne, R. P. V., A Nanoscale Optical Biosensor: Sensitivity and Selectivity of an Approach Based on the Localized Surface Plasmon Resonance Spectroscopy of Triangular Silver Nanoparticles. *J. Am. Chem. Soc.* **2002**, *124*, 10596–10604.
- (50) Kim, J.; Campbell, A. S.; de Avila, B. E.; Wang, J., Wearable Biosensors for Healthcare Monitoring. *Nat. Biotechnol.* **2019**, *37*, 389–406.
- (51) Munzer, A. M.; Michael, Z. P.; Star, A., Carbon Nanotubes for the Label-Free Detection of Biomarkers. *ACS Nano* **2013**, *7*, 7448–7453.

- (52) Janssen, J.; Lambeta, M.; White, P.; Byagowi, A., Carbon Nanotube-Based Electrochemical Biosensor for Label-Free Protein Detection. *Biosensors (Basel)* **2019**, *9*, 144.
- (53) Vanova, V.; Mitrevska, K.; Milosavljevic, V.; Hynek, D.; Richtera, L.; Adam, V., Peptide-Based Electrochemical Biosensors Utilized for Protein Detection. *Biosens. Bioelectron.* **2021**, *180*, 113087.
- (54) Ando, T., The Electronic Properties of Graphene and Carbon Nanotubes. *NPG Asia Mater.* **2009**, *1*, 17–21.
- (55) Cao, Y.; Cong, S.; Cao, X.; Wu, F.; Liu, Q.; Amer, M. R.; Zhou, C., Review of Electronics Based on Single-Walled Carbon Nanotubes. *Top Curr. Chem.* **2017**, *375*, 75.
- (56) Bachilo, S. M.; Strano, M. S.; Kittrell, C.; Hauge, R. H.; Smalley, R. E.; Weisman, R. B., Structure-Assigned Optical Spectra of Single-Walled Carbon Nanotubes. *Science* **2002**, *298*, 2361–2366.
- (57) Barbero, D. R.; Stranks, S. D., Functional Single-Walled Carbon Nanotubes and Nanoengineered Networks for Organic- and Perovskite-Solar-Cell Applications. *Adv. Mater.* **2016**, *28*, 9668–9685.
- (58) Wildoer, J. W. G.; Venema, L. C.; Rinzler, A. G.; Smalley, R. E.; Dekker, C., Electronic Structure of Atomically Resolved Carbon Nanotubes. *Nature* **1998**, *391*, 59–62.
- (59) Lefebvre, J.; Ding, J.; Li, Z.; Finnie, P.; Lopinski, G.; Malenfant, P. R. L., High-Purity Semiconducting Single-Walled Carbon Nanotubes: A Key Enabling Material in Emerging Electronics. *Acc. Chem. Res.* **2017**, *50*, 2479–2486.
- (60) Si, J.; Zhong, D.; Xu, H.; Xiao, M.; Yu, C.; Zhang, Z.; Peng, L. M., Scalable Preparation of High-Density Semiconducting Carbon Nanotube Arrays for High-Performance Field-Effect Transistors. *ACS Nano* **2018**, *12*, 627–634.
- (61) Liu, L.; Han, J.; Xu, L.; Zhou, J.; Zhao, C.; Ding, S.; Shi, H.; Xiao, M.; Ding, L.; Ma, Z.; Jin, C.; Zhang, Z.; Peng, L.-M., Aligned, High-Density Semiconducting Carbon Nanotube Arrays for High-Performance Electronics. *Science* **2020**, *368*, 850–856.
- (62) Ma, Z.; Kong, D.; Pan, L.; Bao, Z., Skin-Inspired Electronics: Emerging Semiconductor Devices and Systems. *J. Semicond.* **2020**, *41*, 041601.
- (63) Lei, T.; Shao, L. L.; Zheng, Y. Q.; Pitner, G.; Fang, G.; Zhu, C.; Li, S.; Beausoleil, R.; Wong, H. P.; Huang, T. C.; Cheng, K. T.; Bao, Z., Low-Voltage High-Performance Flexible Digital and Analog Circuits Based on Ultrahigh-Purity Semiconducting Carbon Nanotubes. *Nat. Commun.* **2019**, *10*, 2161.
- (64) Shulaker, M. M.; Hills, G.; Patil, N.; Wei, H.; Chen, H. Y.; Wong, H. S.; Mitra, S., Carbon Nanotube Computer. *Nature* **2013**, *501*, 526–530.

- (65) Janas, D., Towards Monochiral Carbon Nanotubes: A Review of Progress in the Sorting of Single-Walled Carbon Nanotubes. *Mater. Chem. Front.* **2018**, *2*, 36–63.
- (66) Krupke, R.; Hennrich, F.; Löhneysen, H. v.; Kappes, M., Separation of Metallic from Semiconducting Single-Walled Carbon Nanotubes. *Science* **2003**, *18*, 344–347.
- (67) Tulevski, G. S.; Franklin, A. D.; Afzali, A., High Purity Isolation and Quantification of Semiconducting Carbon Nanotubes via Column Chromatography. *ACS Nano* **2013**, *7*, 2971–2976.
- (68) Silvera-Batista, C. A.; Scott, D. C.; McLeod, S. M.; Ziegler, K. J., A Mechanistic Study of the Selective Retention of SDS-Suspended Single-Wall Carbon Nanotubes on Agarose Gels. *J. Phys. Chem. C* **2011**, *115*, 9361–9369.
- (69) Hersam, M. C., Progress Towards Monodisperse Single-walled Carbon Nanotubes. *Nat. Nanotechnol.* **2008**, *3*, 387–394.
- (70) Arnold, M. S.; Green, A. A.; Hulvat, J. F.; Stupp, S. I.; Hersam, M. C., Sorting Carbon Nanotubes by Electronic Structure using Density Differentiation. *Nat. Nanotechnol.* **2006**, *1*, 60–65.
- (71) Khripin, C. Y.; Fagan, J. A.; Zheng, M., Spontaneous Partition of Carbon Nanotubes in Polymer-Modified Aqueous Phases. *J. Am. Chem. Soc.* **2013**, *135*, 6822–6825.
- (72) Yang, F.; Wang, M.; Zhang, D.; Yang, J.; Zheng, M.; Li, Y., Chirality Pure Carbon Nanotubes: Growth, Sorting, and Characterization. *Chem. Rev.* **2020**, *120*, 2693–2758.
- (73) Fagan, J. A., Aqueous Two-Polymer Phase Extraction of Single-Wall Carbon Nanotubes Using Surfactants. *Nanoscale Adv.* **2019**, *1*, 3307–3324.
- (74) Ding, J.; Li, Z.; Lefebvre, J.; Cheng, F.; Dunford, J. L.; Malenfant, P. R.; Humes, J.; Kroeger, J., A Hybrid Enrichment Process Combining Conjugated Polymer Extraction and Silica Gel Adsorption for High Purity Semiconducting Single-Walled Carbon Nanotubes (SWCNT). *Nanoscale* **2015**, *7*, 15741–15747.
- (75) Mistry, K. S.; Larsen, B. A.; Blackburn, J. L., High-Yield Dispersions of Large-Diameter Semiconducting Single-Walled Carbon Nanotubes with Tunable Narrow Chirality Distributions. *ACS Nano* **2013**, *7*, 2231–2239.
- (76) Nish, A.; Hwang, J. Y.; Doig, J.; Nicholas, R. J., Highly Selective Dispersion of Single-Walled Carbon Nanotubes Using Aromatic Polymers. *Nat. Nanotechnol.* **2007**, *2*, 640–646.
- (77) Wang, H.; Bao, Z., Conjugated Polymer Sorting of Semiconducting Carbon Nanotubes and their Electronic Applications. *Nano Today* **2015**, *10*, 737–758.
- (78) Wang, J.; Lei, T., Separation of Semiconducting Carbon Nanotubes using Conjugated Polymer Wrapping. *Polymers (Basel)* **2020**, *12*, 1548.

- (79) Ding, J.; Li, Z.; Lefebvre, J.; Cheng, F.; Dubey, G.; Zou, S.; Finnie, P.; Hrdina, A.; Scoles, L.; Lopinski, G. P.; Kingston, C. T.; Simard, B.; Malenfant, P. R., Enrichment of Large-Diameter Semiconducting SWCNTs by Polyfluorene Extraction for High Network Density Thin Film Transistors. *Nanoscale* **2014**, *6*, 2328–2339.
- (80) Bhakta, S. A.; Evans, E.; Benavidez, T. E.; Garcia, C. D., Protein Adsorption onto Nanomaterials for the Development of Biosensors and Analytical Devices: A Review. *Anal. Chim. Acta.* **2015**, *872*, 7–25.
- (81) Allen, B. L.; Kichambare, P. D.; Star, A., Carbon Nanotube Field-Effect-Transistor-Based Biosensors. *Adv. Mater.* **2007**, *19*, 1439–1451.
- (82) Zhou, Y.; Fang, Y.; Ramasamy, R. P., Non-Covalent Functionalization of Carbon Nanotubes for Electrochemical Biosensor Development. *Sensors (Basel)* **2019**, *19*, 392.
- (83) Bilalis, P.; Katsigiannopoulos, D.; Avgeropoulos, A.; Sakellariou, G., Non-Covalent Functionalization of Carbon Nanotubes with Polymers. *RSC Adv.* **2014**, *4*, 2911–2934.
- (84) Tung, N. T.; Tue, P. T.; Thi Ngoc Lien, T.; Ohno, Y.; Maehashi, K.; Matsumoto, K.; Nishigaki, K.; Biyani, M.; Takamura, Y., Peptide Aptamer-Modified Single-Walled Carbon Nanotube-Based Transistors for High-Performance Biosensors. *Sci. Rep.* **2017**, *7*, 17881.
- (85) Calvaresi, M.; Zerbetto, F., The Devil and Holy Water: Protein and Carbon Nanotube Hybrids. *Acc. Chem. Res.* **2013**, *46*, 2454–2463.
- (86) Richard, C.; Doan, B.-T.; Beloeil, J.-C.; Bessodes, M.; Tóth, É.; Scherman, D., Noncovalent Functionalization of Carbon Nanotubes with Amphiphilic Gd³⁺ Chelates: Toward Powerful T1 and T2 MRI Contrast Agents. *Nano Lett.* **2008**, *8*, 232–236.
- (87) Zhao, Y.-L.; Stoddart, J. F., Noncovalent Functionalization of Single-Walled Carbon Nanotubes. *Acc. Chem. Res.* **2009**, *42*, 1161–1171.
- (88) ThermoFisher Scientific. Carbodiimide Crosslinker Chemistry. <https://www.thermofisher.com/us/en/home/life-science/protein-biology/protein-biology-learning-center/protein-biology-resource-library/pierce-protein-methods/carbodiimide-crosslinker-chemistry.html> (accessed March 15, 2021).
- (89) Chen, R. J.; Zhang, Y.; Wang, D.; Dai, H., Noncovalent Sidewall Functionalization of Single-Walled Carbon Nanotubes for Protein Immobilization. *J. Am. Chem. Soc.* **2001**, *123*, 3838–3839.
- (90) Lerner, M. B.; Dailey, J.; Goldsmith, B. R.; Brisson, D.; Johnson, A. T., Detecting Lyme Disease using Antibody-Functionalized Single-Walled Carbon Nanotube Transistors. *Biosens. Bioelectron.* **2013**, *45*, 163–167.
- (91) Kauffman, D. R.; Star, A., Chemically Induced Potential Barriers at the Carbon Nanotube–Metal Nanoparticle Interface. *Nano Lett.* **2007**, *7*, 1863–1868.

- (92) Abdelhalim, A.; Abdellah, A.; Scarpa, G.; Lugli, P., Metallic Nanoparticles Functionalizing Carbon Nanotube Networks for Gas Sensing Applications. *Nanotechnology* **2014**, *25*, 055208.
- (93) Bian, L.; Sorescu, D. C.; Chen, L.; White, D. L.; Burkert, S. C.; Khalifa, Y.; Zhang, Z.; Sejdic, E.; Star, A., Machine-Learning Identification of the Sensing Descriptors Relevant in Molecular Interactions with Metal Nanoparticle-Decorated Nanotube Field-Effect Transistors. *ACS Appl. Mater. Interfaces* **2019**, *11*, 1219–1227.
- (94) Zhang, K.; Ji, J.; Fang, X.; Yan, L.; Liu, B., Carbon Nanotube/Gold Nanoparticle Composite-Coated Membrane as a Facile Plasmon-Enhanced Interface For Sensitive SERS Sensing. *Analyst* **2015**, *140*, 134–139.
- (95) Michael, Z. P.; Shao, W.; Sorescu, D. C.; Euler, R. W.; Burkert, S. C.; Star, A., Probing Biomolecular Interactions with Gold Nanoparticle-Decorated Single-Walled Carbon Nanotubes. *J. Phys. Chem. C* **2017**, *121*, 20813–20820.
- (96) Jorio, A.; Saito, R., Raman Spectroscopy for Carbon Nanotube Applications. *J. Appl. Phys.* **2021**, *129*, 021102.
- (97) Zhang, L.; Ni, Q.-Q.; Fu, Y.; Natsuki, T., One-Step Preparation of Water-Soluble Single-Walled Carbon Nanotubes. *Appl. Surf. Sci.* **2009**, *255*, 7095–7099.
- (98) Li, Z.; Ding, J.; Finnie, P.; Lefebvre, J.; Cheng, F.; Kingston, C. T.; Malenfant, P. R. L., Raman Microscopy Mapping for the Purity Assessment of Chirality Enriched Carbon Nanotube Networks in Thin-Film Transistors. *Nano Res.* **2015**, *8*, 2179–2187.
- (99) Tian, Y.; Jiang, H.; Laiho, P.; Kauppinen, E. I., Validity of Measuring Metallic and Semiconducting Single-Walled Carbon Nanotube Fractions by Quantitative Raman Spectroscopy. *Anal. Chem.* **2018**, *90*, 2517–2525.
- (100) Geng, H.-Z.; Lee, D. S.; Kim, K. K.; Han, G. H.; Park, H. K.; Lee, Y. H., Absorption Spectroscopy of Surfactant-Dispersed Carbon Nanotube Film: Modulation of Electronic Structures. *Chem. Phys. Lett.* **2008**, *455*, 275–278.
- (101) Strano, M. S.; Dyke, C. A.; Usrey, M. L.; Barone, P. W.; Allen, M. J.; Shan, H.; Kittrell, C.; Hauge, R. H.; Tour, J. M.; Smalley, R. E., Electronic Structure Control of Single-Walled Carbon Nanotube Functionalization. *Science* **2003**, *301*, 1519–1522.
- (102) Ryabenko, A. G.; Dorofeeva, T. V.; Zvereva, G. I., UV–vis–NIR Spectroscopy Study of Sensitivity of Single-Wall Carbon Nanotubes to Chemical Processing and Van-Der-Waals SWNT/SWNT Interaction. Verification of the SWNT Content Measurements by Absorption Spectroscopy. *Carbon* **2004**, *42*, 1523–1535.
- (103) Yun, H.; Hun Han, J.; Kim, S., Fabrication of Conductive and Transparent Single-Walled Carbon Nanotube Films with PEDOT. *Polym. J.* **2012**, *44*, 1238–1243.

- (104) Li, D.; Zhang, J.; He, Y.; Qin, Y.; Wei, Y.; Liu, P.; Zhang, L.; Wang, J.; Li, Q.; Fan, S.; Jiang, K., Scanning Electron Microscopy Imaging of Single-Walled Carbon Nanotubes on Substrates. *Nano Res.* **2017**, *10*, 1804–1818.
- (105) Stokroos, I.; Kalicharan, D.; Want, J. J. L. V. D.; Jongebloed, W. L., A Comparative Study of Thin Coatings of Au/Pd, Pt and Cr Produced by Magnetron Sputtering for FE-SEM. *J. Microsc.* **1998**, *189*, 79–89.
- (106) Sadighbayan, D.; Hasanzadeh, M.; Ghafar-Zadeh, E., Biosensing Based on Field-Effect Transistors (FET): Recent Progress and Challenges. *Trends Anal. Chem.* **2020**, *133*, 116067.
- (107) Syedmoradi, L.; Ahmadi, A.; Norton, M. L.; Omidfar, K., A Review on Nanomaterial-Based Field Effect Transistor Technology for Biomarker Detection. *Microchim. Acta* **2019**, *186*, 739.
- (108) Liu, Q.; Liu, Y.; Wu, F.; Cao, X.; Li, Z.; Alharbi, M.; Abbas, A. N.; Amer, M. R.; Zhou, C., Highly Sensitive and Wearable In₂O₃ Nanoribbon Transistor Biosensors with Integrated On-Chip Gate for Glucose Monitoring in Body Fluids. *ACS Nano* **2018**, *12*, 1170–1178.
- (109) Silva, G. O.; Michael, Z. P.; Bian, L.; Shurin, G. V.; Mulato, M.; Shurin, M. R.; Star, A., Nanoelectronic Discrimination of Nonmalignant and Malignant Cells Using Nanotube Field-Effect Transistors. *ACS Sens.* **2017**, *2*, 1128–1132.
- (110) Shao, W.; Burkert, S. C.; White, D. L.; Scott, V. L.; Ding, J.; Li, Z.; Ouyang, J.; Lapointe, F.; Malenfant, P. R. L.; Islam, K.; Star, A., Probing Ca²⁺-Induced Conformational Change of Calmodulin with Gold Nanoparticle-Decorated Single-Walled Carbon Nanotube Field-Effect Transistors. *Nanoscale* **2019**, *11*, 13397–13406.
- (111) Baughman, R. H.; Zakhidov, A. A.; de Heer, W. A., Carbon Nanotubes—the Route Toward Applications. *Science* **2002**, *297*, 787–792.
- (112) Li, J.; Ng, H. T.; Cassell, A.; Fan, W.; Chen, H.; Ye, Q.; Koehne, J.; Han, J.; Meyyappan, M., Carbon Nanotube Nanoelectrode Array for Ultrasensitive DNA Detection. *Nano Lett.* **2003**, *3*, 597–602.
- (113) Koehne, J.; Chen, H.; Li, J.; Cassell, A. M.; Ye, Q.; Ng, H. T.; Han, J.; Meyyappan, M., Ultrasensitive Label-Free DNA Analysis using an Electronic Chip Based on Carbon Nanotube Nanoelectrode Arrays. *Nanotechnology* **2003**, *14*, 1239–1245.
- (114) Li, J.; Lu, Y.; Ye, Q.; Cinke, M.; Han, J.; Meyyappan, M., Carbon Nanotube Sensors for Gas and Organic Vapor Detection. *Nano Lett.* **2003**, *3*, 929–933.
- (115) Koehne, J. E.; Chen, H.; Cassell, A. M.; Ye, Q.; Han, J.; Meyyappan, M.; Li, J., Miniaturized Multiplex Label-Free Electronic Chip for Rapid Nucleic Acid Analysis Based on Carbon Nanotube Nanoelectrode Arrays. *Clin. Chem.* **2004**, *50*, 1886–1893.

- (116) Lu, Y.; Li, J.; Han, J.; Ng, H. T.; Binder, C.; Partridge, C.; Meyyappan, M., Room Temperature Methane Detection using Palladium Loaded Single-Walled Carbon Nanotube Sensors. *Chem. Phys. Lett.* **2004**, *391*, 344–348.
- (117) Volder, M. F. L. D.; Tawfick, S. H.; Baughman, R. H.; Hart, A. J., Carbon Nanotubes: Present and Future Commercial Applications. *Science* **2013**, *339*, 535–539.
- (118) Odom, T. W.; Huang, J.-L.; Kim, P.; Lieber, C. M., Atomic Structure and Electronic Properties of Single-Walled Carbon Nanotubes. *Nature* **1998**, *391*, 62–64.
- (119) Ghosh, S.; Bachilo, S. M.; Weisman, R. B., Advanced Sorting of Single-Walled Carbon Nanotubes by Nonlinear Density-Gradient Ultracentrifugation. *Nat. Nanotechnol.* **2010**, *5*, 443–450.
- (120) Wei, L.; Flavel, B. S.; Li, W.; Krupke, R.; Chen, Y., Exploring The Upper Limit of Single-Walled Carbon Nanotube Purity by Multiple-Cycle Aqueous Two-Phase Separation. *Nanoscale* **2017**, *9*, 11640–11646.
- (121) Hennrich, F.; Li, W.; Fischer, R.; Lebedkin, S.; Krupke, R.; Kappes, M. M., Length-Sorted, Large-Diameter, Polyfluorene-Wrapped Semiconducting Single-Walled Carbon Nanotubes for High-Density, Short-Channel Transistors. *ACS Nano* **2016**, *10*, 1888–1895.
- (122) Derenskyi, V.; Gomulya, W.; Salazar Rios, J. M.; Fritsch, M.; Frohlich, N.; Jung, S.; Allard, S.; Bisri, S. Z.; Gordiichuk, P.; Herrmann, A.; Scherf, U.; Loi, M. A., Carbon Nanotube Network Ambipolar Field-Effect Transistors with 10^8 On/Off Ratio. *Adv. Mater.* **2014**, *26*, 5969–5975.
- (123) Xiao, M.; Liang, S.; Han, J.; Zhong, D.; Liu, J.; Zhang, Z.; Peng, L., Batch Fabrication of Ultrasensitive Carbon Nanotube Hydrogen Sensors with Sub-ppm Detection Limit. *ACS Sens.* **2018**, *3*, 749–756.
- (124) Li, Z.; Ding, J.; Guo, C.; Lefebvre, J.; Malenfant, P. R. L., Decomposable s-Tetrazine Copolymer Enables Single Walled Carbon Nanotube Thin Film Transistors and Sensors with Improved Sensitivity. *Adv. Funct. Mater.* **2018**, *28*, 1705568.
- (125) Jeon, J. Y.; Kang, B. C.; Byun, Y. T.; Ha, T. J., High-Performance Gas Sensors Based on Single-Wall Carbon Nanotube Random Networks For The Detection of Nitric Oxide Down to the Ppb-Level. *Nanoscale* **2019**, *11*, 1587–1594.
- (126) Zhang, H.; Xiang, L.; Yang, Y.; Xiao, M.; Han, J.; Ding, L.; Zhang, Z.; Hu, Y.; Peng, L. M., High-Performance Carbon Nanotube Complementary Electronics and Integrated Sensor Systems on Ultrathin Plastic Foil. *ACS Nano* **2018**, *12*, 2773–2779.
- (127) Zheng, H. Y.; Alsager, O. A.; Zhu, B.; Travas-Sejdic, J.; Hodgkiss, J. M.; Plank, N. O. V., Electrostatic Gating in Carbon Nanotube Aptasensors. *Nanoscale* **2016**, *8*, 13659–13668.
- (128) Thanhaichelvan, M.; Browning, L. A.; Dierkes, M. P.; Reyes, R. M.; Kralicek, A. V.; Carraher, C.; Marlow, C. A.; Plank, N. O. V., Metallic-Semiconducting Junctions Create

- Sensing Hot-Spots in Carbon Nanotube FET Aptasensors Near Percolation. *Biosens. Bioelectron.* **2019**, *130*, 408–413.
- (129) Filipiak, M. S.; Rother, M.; Andoy, N. M.; Knudsen, A. C.; Grimm, S.; Bachran, C.; Swee, L. K.; Zaumseil, J.; Tarasov, A., Highly Sensitive, Selective and Label-Free Protein Detection in Physiological Solutions using Carbon Nanotube Transistors with Nanobody Receptors. *Sens. Actuators B Chem.* **2018**, *255*, 1507–1516.
- (130) Hatada, M.; Tran, T. T.; Tsugawa, W.; Sode, K.; Mulchandani, A., Affinity Sensor for Haemoglobin A1c Based on Single-Walled Carbon Nanotube Field-Effect Transistor and Fructosyl Amino Acid Binding Protein. *Biosens. Bioelectron.* **2019**, *129*, 254–259.
- (131) Jones, E. M.; Balakrishnan, G.; Squier, T. C.; Spiro, T. G., Distinguishing Unfolding and Functional Conformational Transitions of Calmodulin using Ultraviolet Resonance Raman Spectroscopy. *Protein Sci.* **2014**, *23*, 1094–1101.
- (132) Edman, C. F.; George, S. E.; Means, A. R.; Schulman, H.; Yaswen, P., Selective Activation and Inhibition of Calmodulin-Dependent Enzymes by a Calmodulin-Like Protein Found in Human Epithelial Cells. *Eur. J. Biochem.* **1994**, *226*, 725–730.
- (133) Kretsinger, R. H.; Rudnick, S. E.; Weissman, L. J., Crystal Structure of Calmodulin. *J. Inorg. Biochem.* **1986**, *28*, 289–302.
- (134) Zhang, M.; Tanaka, T.; Ikura, M., Calcium-Induced Conformational Transition Revealed by the Solution Structure of Apo Calmodulin. *Nat. Struct. Biol.* **1995**, *2*, 758–767.
- (135) DeGrave, A. J.; Ha, J. H.; Loh, S. N.; Chong, L. T., Large Enhancement of Response Times of a Protein Conformational Switch by Computational Design. *Nat. Commun.* **2018**, *9*, 1013–1021.
- (136) Babu, Y. S.; Bugg, C. E.; Cook, W. J., Structure of Calmodulin Refined at 2.2 Å Resolution. *J. Mol. Biol.* **1988**, *204*, 191–204.
- (137) Yuan, H.; Qi, J.; Xing, C.; An, H.; Niu, R.; Zhan, Y.; Fan, Y.; Yan, W.; Li, R.; Wang, B.; Wang, S., Graphene-Oxide-Conjugated Polymer Hybrid Materials for Calmodulin Sensing by using FRET Strategy. *Adv. Funct. Mater.* **2015**, *25*, 4412–4418.
- (138) Clery, A.; Sohler, T. J. M.; Welte, T.; Langer, A.; Allain, F. H. T., SwitchSENSE: A New Technology to Study Protein-RNA Interactions. *Methods* **2017**, *118–119*, 137–145.
- (139) Li, I. T.; Walker, G. C., Signature of Hydrophobic Hydration in a Single Polymer. *Proc. Natl. Acad. Sci. U.S.A* **2011**, *108*, 16527–16532.
- (140) Choi, Y.; Moody, I. S.; Sims, P. C.; Hunt, S. R.; Corso, B. L.; Perez, I.; Weiss, G. A.; Collins, P. G., Single-Molecule Lysozyme Dynamics Monitored by an Electronic Circuit. *Science* **2012**, *335*, 319–324.

- (141) Bouilly, D.; Hon, J.; Daly, N. S.; Trocchia, S.; Vernick, S.; Yu, J.; Warren, S.; Wu, Y.; Gonzalez, R. L., Jr.; Shepard, K. L.; Nuckolls, C., Single-Molecule Reaction Chemistry in Patterned Nanowells. *Nano Lett.* **2016**, *16*, 4679–4685.
- (142) Homenick, C. M.; James, R.; Lopinski, G. P.; Dunford, J.; Sun, J.; Park, H.; Jung, Y.; Cho, G.; Malenfant, P. R. L., Fully Printed and Encapsulated SWCNT-Based Thin Film Transistors via a Combination of R2R Gravure and Inkjet Printing. *ACS Appl. Mater. Interfaces* **2016**, *8*, 27900–27910.
- (143) Balog, E. M.; Norton, L. E.; Thomas, D. D.; Fruen, B. R., Role of Calmodulin Methionine Residues in Mediating Productive Association with Cardiac Ryanodine Receptors. *Am. J. Physiol. Heart Circ. Physiol.* **2006**, *290*, H794–H799.
- (144) Munzer, A. M.; Seo, W.; Morgan, G. J.; Michael, Z. P.; Zhao, Y.; Melzer, K.; Scarpa, G.; Star, A., Sensing Reversible Protein-Ligand Interactions with Single-Walled Carbon Nanotube Field-Effect Transistors. *J. Phys. Chem. C* **2014**, *118*, 17193–17199.
- (145) Chen, Y.; Vedala, H.; Kotchey, G. P.; Audfray, A.; Cecioni, S.; Imberty, A.; Vidal, S.; Star, A., Electronic Detection of Lectins Using Carbohydrate-Functionalized Nanostructures: Graphene versus Carbon Nanotubes. *ACS Nano* **2012**, *6*, 760–770.
- (146) Kauffman, D. R.; Sorescu, D. C.; Schofield, D. P.; Allen, B. L.; Jordan, K. D.; Star, A., Understanding the Sensor Response of Metal-Decorated Carbon Nanotubes. *Nano Lett.* **2010**, *10*, 958–963.
- (147) Jorio, A.; Fantini, C.; Dantas, M. S. S.; Pimenta, M. A.; Souza Filho, A. G.; Samsonidze, G. G.; Brar, V. W.; Dresselhaus, G.; Dresselhaus, M. S.; Swan, A. K.; Ünlü, M. S.; Goldberg, B. B.; Saito, R., Linewidth of the Raman Features of Individual Single-Wall Carbon Nanotubes. *Phys. Rev. B* **2002**, *66*, 115411.
- (148) Dresselhaus, M. S.; Dresselhaus, G.; Saito, R.; Jorio, A., Raman Spectroscopy of Carbon Nanotubes. *Phys. Rep.* **2005**, *409*, 47–99.
- (149) Sabur, A.; Havel, M.; Gogotsi, Y., SERS Intensity Optimization by Controlling the Size and Shape of Faceted Gold Nanoparticles. *J. Raman Spectrosc.* **2008**, *39*, 61–67.
- (150) Voggu, R.; Rout, C. S.; Franklin, A. D.; Fisher, T. S.; Rao, C. N. R., Extraordinary Sensitivity of the Electronic Structure and Properties of Single-Walled Carbon Nanotubes to Molecular Charge Transfer. *J. Phys. Chem. C* **2008**, *112*, 13053–13056.
- (151) Xu, J. L.; Dai, R. X.; Xin, Y.; Sun, Y. L.; Li, X.; Yu, Y. X.; Xiang, L.; Xie, D.; Wang, S. D.; Ren, T. L., Efficient and Reversible Electron Doping of Semiconductor-Enriched Single-Walled Carbon Nanotubes by Using Decamethylcobaltocene. *Sci. Rep.* **2017**, *7*, 6751.
- (152) Blackburn, J. L.; Svedruzic, D.; McDonald, T. J.; Kim, Y.-H.; King, P. W.; Heben, M. J., Raman Spectroscopy of Charge Transfer Interactions Between Single Wall Carbon Nanotubes and [FeFe] Hydrogenase. *Dalton Trans.* **2008**, 5454–5461.

- (153) Bayley, P.; Martin, S.; Jones, G., The Conformation of Calmodulin: A Substantial Environmentally Sensitive Helical Transition in Ca⁴-Calmodulin with Potential Mechanistic Function. *FEBS lett.* **1988**, *238*, 61–66.
- (154) Settimo, L.; Donnini, S.; Juffer, A. H.; Woody, R. W.; Marin, O., Conformational Changes Upon Calcium Binding and Phosphorylation in a Synthetic Fragment of Calmodulin. *Biopolymers* **2007**, *88*, 373–385.
- (155) Nakai, J.; Ohkura, M.; Imoto, K., A High Signal-to-Noise Ca²⁺ Probe Composed of a Single Green Fluorescent Protein. *Nat. Biotechnol.* **2001**, *19*, 137–141.
- (156) Wang, Q.; Shui, B.; Kotlikoff, M. I.; Sondermann, H., Structural Basis for Calcium Sensing by GCaMP2. *Structure* **2008**, *16*, 1817–1827.
- (157) Herman, R. A.; Scherer, P. N.; Shan, G., Evaluation of Logistic and Polynomial Models for Fitting Sandwich-Elisa Calibration Curves. *J. Immunol. Methods* **2008**, *339*, 245–258.
- (158) Grabarek, Z., Insights into Modulation of Calcium Signaling by Magnesium in Calmodulin, Troponin C and Related Ef-Hand Proteins. *Biochim. Biophys. Acta* **2011**, *1813*, 913–921.
- (159) Fogh-Andersen, N., Albumin/Calcium Association at Different pH, as Determined by Potentiometry. *Clin. Chem.* **1977**, *23*, 2122–2126.
- (160) Chen, R. J.; Choi, H. C.; Bangsaruntip, S.; Yenilmez, E.; Tang, X.; Wang, Q.; Chang, Y.-L.; Dai, H., An Investigation of the Mechanisms of Electronic Sensing of Protein Adsorption on Carbon Nanotube Devices. *J. Am. Chem. Soc.* **2004**, *126*, 1563–1568.
- (161) Ding, M.; Tang, Y.; Star, A., Understanding Interfaces in Metal-Graphitic Hybrid Nanostructures. *J. Phys. Chem. Lett.* **2013**, *4*, 147–160.
- (162) Andre, I.; Kesvatera, T.; Jonsson, B.; Akerfeldt, K. S.; Linse, S., The Role of Electrostatic Interactions in Calmodulin-Peptide Complex Formation. *Biophys. J.* **2004**, *87*, 1929–1938.
- (163) Heller, I.; Janssens, A. M.; Mannik, J.; Minot, E. D.; Lemay, S. G.; Dekker, C., Identifying the Mechanism of Biosensing with Carbon Nanotube Transistors. *Nano Lett.* **2008**, *8*, 591–595.
- (164) Tey, J. N.; Ho, X.; Wei, J., Effect of Doping on Single-Walled Carbon Nanotubes Network of Different Metallicity. *Nanoscale Res. Lett.* **2012**, *7*, 548–554.
- (165) Ogawa, Y.; Tanokura, M., Calcium Binding to Calmodulin: Effects of Ionic Strength, Mg²⁺, pH and Temperature. *J. Biochem.* **1984**, *95*, 19–28.
- (166) Alizadeh, T.; Shamkhali, A. N.; Hanifehpour, Y.; Joo, S. W., A Ca²⁺ Selective Membrane Electrode Based on Calcium-Imprinted Polymeric Nanoparticles. *New. J. Chem.* **2016**, *40*, 8479–8487.

- (167) Ocana, C.; Abramova, N.; Bratov, A.; Lindfors, T.; Bobacka, J., Calcium-Selective Electrodes Based on Photo-Cured Polyurethane-Acrylate Membranes Covalently Attached to Methacrylate Functionalized Poly(3,4-Ethylenedioxythiophene) as Solid-Contact. *Talanta* **2018**, *186*, 279–285.
- (168) Wu, M.; Meng, S.; Wang, Q.; Si, W.; Huang, W.; Dong, X., Nickel-Cobalt Oxide Decorated Three-Dimensional Graphene as an Enzyme Mimic for Glucose and Calcium Detection. *ACS Appl. Mater. Interfaces* **2015**, *7*, 21089–21094.
- (169) Ankireddy, S. R.; Kim, J., Highly Selective and Sensitive Detection Of Calcium (II) Ions in Human Serum using Novel Fluorescent Carbon Dots. *Sens. Actuators B Chem.* **2018**, *255*, 3425–3433.
- (170) Li, Z.; Ding, J.; Lefebvre, J.; Malenfant, P. R. L., Surface Effects on Network Formation of Conjugated Polymer Wrapped Semiconducting Single Walled Carbon Nanotubes and Thin Film Transistor Performance. *Org. Electron.* **2015**, *26*, 15–19.
- (171) Schlosser, R. J.; Bolger, W. E., Nasal Cerebrospinal Fluid Leaks: Critical Review and Surgical Considerations. *Laryngoscope* **2004**, *114*, 255–265.
- (172) Banks, C. A.; Palmer, J. N.; Chiu, A. G.; O'Malley, B. W., Jr.; Woodworth, B. A.; Kennedy, D. W., Endoscopic Closure of CSF Rhinorrhea: 193 Cases Over 21 Years. *Otolaryngol. Head Neck Surg.* **2009**, *140*, 826–833.
- (173) Mantur, M.; Lukaszewicz-Zajac, M.; Mroczko, B.; Kulakowska, A.; Ganslandt, O.; Kemon, H.; Szmitkowski, M.; Drozdowski, W.; Zimmermann, R.; Kornhuber, J.; Lewczuk, P., Cerebrospinal Fluid Leakage-Reliable Diagnostic Methods. *Clin. Chim. Acta* **2011**, *412*, 837–840.
- (174) Oakley, G. M.; Alt, J. A.; Schlosser, R. J.; Harvey, R. J.; Orlandi, R. R., Diagnosis of Cerebrospinal Fluid Rhinorrhea: An Evidence-Based Review with Recommendations. *Int. Forum Allergy Rhinol.* **2016**, *6*, 8–16.
- (175) Macedo, M. F.; de Sousa, M., Transferrin and the Transferrin Receptor: Of Magic Bullets and Other Concerns. *Inflamm. Allergy Drug Targets* **2008**, *7*, 41–52.
- (176) Arrer, E.; Oberascher, G.; Gibitz, H.-J., Protein Distribution in the Human Perilymph: A Comparative Study between Perilymph (Post Mortem), CSF and Blood Serum. *Acta Otolaryngol.* **1988**, *106*, 117–123.
- (177) Schnabel, C.; Martino, E. D.; Gilsbach, J. M.; Riediger, D.; Gressner, A. M.; Kunz, D., Comparison of β 2-Transferrin and β -Trace Protein for Detection of Cerebrospinal Fluid in Nasal and Ear Fluids. *Clin. Chem.* **2004**, *50*, 661–663.
- (178) Brown, K. J.; Vanderver, A.; Hoffman, E. P.; Schiffmann, R.; Hathout, Y., Characterization of Transferrin Glycopeptide Structures in Human Cerebrospinal Fluid. *Int. J. Mass Spectrom.* **2012**, *312*, 97–106.

- (179) Normansell, D. E.; Stacy, E. K.; Booker, C. F.; Butler, T. Z., Detection of Beta-2 Transferrin in Otorrhea and Rhinorrhea in a Routine Clinical Laboratory Setting. *Clin. Diagn. Lab. Immunol.* **1994**, *1*, 68–70.
- (180) Anani, W. Q.; Ojerholm, E.; Shurin, M. R., Resolving Transferrin Isoforms via Agarose Gel Electrophoresis. *Lab. Med.* **2015**, *46*, 26–33.
- (181) Kumar, S.; Tripathy, S.; Jyoti, A.; Singh, S. G., Recent Advances in Biosensors for Diagnosis and Detection of Sepsis: A Comprehensive Review. *Biosens. Bioelectron.* **2019**, *124–125*, 205–215.
- (182) Florea, A.; Melinte, G.; Simon, I.; Cristea, C., Electrochemical Biosensors as Potential Diagnostic Devices for Autoimmune Diseases. *Biosensors (Basel)* **2019**, *9*, 38.
- (183) Gupta, S.; Kaushal, A.; Kumar, A.; Kumar, D., Recent Advances in Biosensors for Diagnosis of Celiac Disease: A Review. *Biotechnol. Bioeng.* **2019**, *116*, 444–451.
- (184) Shandilya, R.; Bhargava, A.; Bunkar, N.; Tiwari, R.; Goryacheva, I. Y.; Mishra, P. K., Nanobiosensors: Point-of-Care Approaches for Cancer Diagnostics. *Biosens. Bioelectron.* **2019**, *130*, 147–165.
- (185) Farzin, L.; Shamsipur, M.; Samandari, L.; Sheibani, S., HIV Biosensors for Early Diagnosis of Infection: The Intertwine of Nanotechnology with Sensing Strategies. *Talanta* **2020**, *206*, 120201.
- (186) Carneiro, P.; Morais, S.; do Carmo Pereira, M., Biosensors on the Road to Early Diagnostic and Surveillance of Alzheimer's Disease. *Talanta* **2020**, *211*, 120700.
- (187) Shao, W.; Shurin, M. R.; Wheeler, S. E.; He, X.; Star, A., Rapid Detection of SARS-CoV-2 Antigens Using High-Purity Semiconducting Single-Walled Carbon Nanotube-Based Field-Effect Transistors. *ACS Appl. Mater. Interfaces* **2021**, *13*, 10321–10327.
- (188) Lee, C.-S.; Kim, J. S.; Kim, T. H., A Chemodosimeter-Modified Carbon Nanotube-Field Effect Transistor: Toward a Highly Selective and Sensitive Electrical Sensing Platform. *RSC Adv.* **2019**, *9*, 28414–28420.
- (189) De Volder, M. F. L.; Tawfick, S. H.; Baughman, R. H.; Hart, A. J., Carbon Nanotubes: Present and Future Commercial Applications. *Science* **2013**, *339*.
- (190) Zhou, C.; Zhao, J.; Ye, J.; Tange, M.; Zhang, X.; Xu, W.; Zhang, K.; Okazaki, T.; Cui, Z., Printed Thin-Film Transistors And NO₂ Gas Sensors Based on Sorted Semiconducting Carbon Nanotubes by Isoindigo-Based Copolymer. *Carbon* **2016**, *108*, 372–380.
- (191) Liu, Y.; Wei, N.; Zhao, Q.; Zhang, D.; Wang, S.; Peng, L. M., Room Temperature Infrared Imaging Sensors Based on Highly Purified Semiconducting Carbon Nanotubes. *Nanoscale* **2015**, *7*, 6805–6812.

- (192) Ochoa, E. L. M.; Bangham, A. D., N-Acetylneuraminic Acid Molecules as Possible Serotonin Binding Sites. *J. Neurochem.* **1976**, *26*, 1193–1198.
- (193) Yodoshi, M.; Ikuta, T.; Mouri, Y.; Suzuki, S., Specific Extraction of Sialic-Acid-Containing Glycans and Glycopeptides using Serotonin-bonded Silica. *Anal. Sci.* **2010**, *26*, 75–81.
- (194) Meininger, M.; Stepath, M.; Hennig, R.; Cajic, S.; Rapp, E.; Roterig, H.; Wolff, M. W.; Reichl, U., Sialic Acid-Specific Affinity Chromatography for the Separation of Erythropoietin Glycoforms using Serotonin as a Ligand. *J. Chromatogr. B* **2016**, *1012–1013*, 193–203.
- (195) Grange, P. a.; Mouricout, M. a., Transferrin Associated with the Porcine Intestinal Mucosa Is a Receptor Specific for K88ab Fimbriae of *Escherichia coli*. *Infect. Immun.* **1996**, *64*, 606–610.
- (196) Mulla, M. Y.; Tuccori, E.; Magliulo, M.; Lattanzi, G.; Palazzo, G.; Persaud, K.; Torsi, L., Capacitance-Modulated Transistor Detects Odorant Binding Protein Chiral Interactions. *Nat. Commun.* **2015**, *6*, 6010.
- (197) Macchia, E.; Manoli, K.; Holzer, B.; Di Franco, C.; Ghittorelli, M.; Torricelli, F.; Alberga, D.; Mangiatordi, G. F.; Palazzo, G.; Scamarcio, G.; Torsi, L., Single-Molecule Detection with a Millimetre-Sized Transistor. *Nat. Commun.* **2018**, *9*, 3223.
- (198) Nguyen, T. T. K.; Tran, H. V.; Vu, T. T.; Reisberg, S.; Noel, V.; Mattana, G.; Pham, M. C.; Piro, B., Peptide-Modified Electrolyte-Gated Organic Field Effect Transistor. Application to Cu²⁺ Detection. *Biosens. Bioelectron.* **2019**, *127*, 118–125.
- (199) Kazemi, S. H.; Shanehsaz, M.; Ghaemmaghami, M., Non-Faradaic Electrochemical Impedance Spectroscopy as a Reliable and Facile Method: Determination of the Potassium Ion Concentration Using a Guanine Rich Aptasensor. *Mater. Sci. Eng. C* **2015**, *52*, 151–154.
- (200) Tanak, A. S.; Jagannath, B.; Tamrakar, Y.; Muthukumar, S.; Prasad, S., Non-Faradaic Electrochemical Impedimetric Profiling of Procalcitonin and C-Reactive Protein as a Dual Marker Biosensor for Early Sepsis Detection. *Anal. Chim. Acta X* **2019**, *3*, 100029.
- (201) Stevenson, H.; Radha Shanmugam, N.; Paneer Selvam, A.; Prasad, S., The Anatomy of a Nonfaradaic Electrochemical Biosensor. *SLAS Technol.* **2018**, *23*, 5–15.
- (202) Diacci, C.; Berto, M.; Di Lauro, M.; Bianchini, E.; Pinti, M.; Simon, D. T.; Biscarini, F.; Bortolotti, C. A., Label-Free Detection of Interleukin-6 Using Electrolyte Gated Organic Field Effect Transistors. *Biointerphases* **2017**, *12*, 05F401.
- (203) Zhu, D. M.; Dustin, M. L.; Cairo, C. W.; Golan, D. E., Analysis of Two-Dimensional Dissociation Constant of Laterally Mobile Cell Adhesion Molecules. *Biophys. J.* **2007**, *92*, 1022–1034.

- (204) Kronbichler, A.; Kresse, D.; Yoon, S.; Lee, K. H.; Effenberger, M.; Shin, J. I., Asymptomatic Patients as a Source of COVID-19 Infections: A Systematic Review and Meta-Analysis. *Int. J. Infect. Dis.* **2020**, *98*, 180–186.
- (205) Ravi, N.; Cortade, D. L.; Ng, E.; Wang, S. X., Diagnostics for SARS-CoV-2 Detection: A Comprehensive Review of the FDA-EUA COVID-19 Testing Landscape. *Biosens. Bioelectron.* **2020**, *165*, 112454.
- (206) Grant, B. D.; Anderson, C. E.; Williford, J. R.; Alonzo, L. F.; Glukhova, V. A.; Boyle, D. S.; Weigl, B. H.; Nichols, K. P., SARS-CoV-2 Coronavirus Nucleocapsid Antigen-Detecting Half-Strip Lateral Flow Assay Toward the Development of Point of Care Tests Using Commercially Available Reagents. *Anal. Chem.* **2020**, *92*, 11305–11309.
- (207) Porte, L.; Legarraga, P.; Vollrath, V.; Aguilera, X.; Munita, J. M.; Araos, R.; Pizarro, G.; Vial, P.; Iruretagoyena, M.; Dittrich, S.; Weitzel, T., Evaluation of a Novel Antigen-Based Rapid Detection Test for the Diagnosis of SARS-CoV-2 in Respiratory Samples. *Int. J. Infect. Dis.* **2020**, *99*, 328–333.
- (208) Yamayoshi, S.; Sakai-Tagawa, Y.; Koga, M.; Akasaka, O.; Nakachi, I.; Koh, H.; Maeda, K.; Adachi, E.; Saito, M.; Nagai, H.; Ikeuchi, K.; Ogura, T.; Baba, R.; Fujita, K.; Fukui, T.; Ito, F.; Hattori, S. I.; Yamamoto, K.; Nakamoto, T.; Furusawa, Y.; Yasuhara, A.; Ujie, M.; Yamada, S.; Ito, M.; Mitsuya, H.; Omagari, N.; Yotsuyanagi, H.; Iwatsuki-Horimoto, K.; Imai, M.; Kawaoka, Y., Comparison of Rapid Antigen Tests for COVID-19. *Viruses* **2020**, *12*, 1420.
- (209) Yakoh, A.; Pimpitak, U.; Rengpipat, S.; Hirankarn, N.; Chailapakul, O.; Chaiyo, S., Paper-based Electrochemical Biosensor for Diagnosing COVID-19: Detection of SARS-CoV-2 Antibodies and Antigen. *Biosens. Bioelectron.* **2021**, *176*, 112912.
- (210) Chen, Y.; Ren, R.; Pu, H.; Guo, X.; Chang, J.; Zhou, G.; Mao, S.; Kron, M.; Chen, J., Field-Effect Transistor Biosensor for Rapid Detection of Ebola Antigen. *Sci. Rep.* **2017**, *7*, 10974.
- (211) Afsahi, S.; Lerner, M. B.; Goldstein, J. M.; Lee, J.; Tang, X.; Bagarozzi, D. A., Jr.; Pan, D.; Locascio, L.; Walker, A.; Barron, F.; Goldsmith, B. R., Novel Graphene-Based Biosensor for Early Detection of Zika Virus Infection. *Biosens. Bioelectron.* **2018**, *100*, 85–88.
- (212) Uhm, M.; Lee, J. M.; Lee, J.; Lee, J. H.; Choi, S.; Park, B. G.; Kim, D. M.; Choi, S. J.; Mo, H. S.; Jeong, Y. J.; Kim, D. H., Ultrasensitive Electrical Detection of Hemagglutinin for Point-of-Care Detection of Influenza Virus Based on a CMP-NANA Probe and Top-Down Processed Silicon Nanowire Field-Effect Transistors. *Sensors (Basel)* **2019**, *19*, 4502.
- (213) Zhang, X.; Qi, Q.; Jing, Q.; Ao, S.; Zhang, Z.; Ding, M.; Wu, M.; Liu, K.; Wang, W.; Ling, Y.; Zhang, Z.; Fu, W. Electrical Probing of COVID-19 Spike Protein Receptor Binding Domain via a Graphene Field-Effect Transistor *arXiv e-prints* [Online], 2020, p. arXiv:2003.12529. <https://ui.adsabs.harvard.edu/abs/2020arXiv200312529Z> (accessed May 25, 2020).

- (214) Seo, G.; Lee, G.; Kim, M. J.; Baek, S. H.; Choi, M.; Ku, K. B.; Lee, C. S.; Jun, S.; Park, D.; Kim, H. G.; Kim, S. J.; Lee, J. O.; Kim, B. T.; Park, E. C.; Kim, S. I., Rapid Detection of COVID-19 Causative Virus (SARS-CoV-2) in Human Nasopharyngeal Swab Specimens Using Field-Effect Transistor-Based Biosensor. *ACS Nano* **2020**, *14*, 5135–5142.
- (215) Zheng, H. Y.; Alsager, O. A.; Zhu, B.; Travas-Sejdic, J.; Hodgkiss, J. M.; Plank, N. O., Electrostatic Gating in Carbon Nanotube Aptasensors. *Nanoscale* **2016**, *8*, 1365–1368.
- (216) Gebhardt, B.; Syrgiannis, Z.; Backes, C.; Graupner, R.; Hauke, F.; Hirsch, A., Carbon Nanotube Sidewall Functionalization with Carbonyl Compounds-Modified Birch Conditions vs the Organometallic Reduction Approach. *J. Am. Chem. Soc.* **2011**, *133*, 7985–7995.
- (217) Scheller, C.; Krebs, F.; Minkner, R.; Astner, I.; Gil-Moles, M.; Watzig, H., Physicochemical Properties of SARS-CoV-2 for Drug Targeting, Virus Inactivation and Attenuation, Vaccine Formulation and Quality Control. *Electrophoresis* **2020**, *41*, 1137–1151.
- (218) Lerner, M. B.; D’Souza, J.; Pazina, T.; Dailey, J.; Goldsmith, B. R.; Robinson, M. K.; Johnson, A. T. C., Hybrids of a Genetically Engineered Antibody and a Carbon Nanotube Transistor for Detection of Prostate Cancer Biomarkers. *ACS Nano* **2012**, *6*, 5143–5149.
- (219) Hirotsu, Y.; Maejima, M.; Shibusawa, M.; Nagakubo, Y.; Hosaka, K.; Amemiya, K.; Sueki, H.; Hayakawa, M.; Mochizuki, H.; Tsutsui, T.; Kakizaki, Y.; Miyashita, Y.; Yagi, S.; Kojima, S.; Omata, M., Comparison of Automated SARS-CoV-2 Antigen Test for COVID-19 Infection with Quantitative RT-PCR Using 313 Nasopharyngeal Swabs, Including From Seven Serially Followed Patients. *Int. J. Infect. Dis.* **2020**, *99*, 397–402.
- (220) Surjit, M.; Lal, S. K., The SARS-CoV Nucleocapsid Protein: A Protein with Multifarious Activities. *Infect. Genet. Evol.* **2008**, *8*, 397–405.
- (221) Zeng, W.; Liu, G.; Ma, H.; Zhao, D.; Yang, Y.; Liu, M.; Mohammed, A.; Zhao, C.; Yang, Y.; Xie, J.; Ding, C.; Ma, X.; Weng, J.; Gao, Y.; He, H.; Jin, T., Biochemical Characterization of SARS-CoV-2 Nucleocapsid Protein. *Biochem. Biophys. Res. Commun.* **2020**, *527*, 618–623.
- (222) Du, L.; He, Y.; Zhou, Y.; Liu, S.; Zheng, B. J.; Jiang, S., The Spike Protein of SARS-CoV– A Target for Vaccine and Therapeutic Development. *Nat. Rev. Microbiol.* **2009**, *7*, 226–236.